

**INTERPOLATED ESPI USING CONTINUOUS MEASUREMENTS FOR MOVING
SURFACES AND LARGE DEFORMATIONS**

by

Harsh Pokharna

B.Tech., Manipal Institute of Technology, 2016

A THESIS SUBMITTED IN PARTIAL FULFILLMENT OF
THE REQUIREMENTS FOR THE DEGREE OF

MASTER OF APPLIED SCIENCES

in

THE FACULTY OF GRADUATE AND POSTDOCTORAL STUDIES

(Mechanical Engineering)

THE UNIVERSITY OF BRITISH COLUMBIA

(Vancouver)

September 2018

© Harsh Pokharna, 2018

The following individuals certify that they have read, and recommend to the Faculty of Graduate and Postdoctoral Studies for acceptance, a thesis/dissertation entitled:

Interpolated ESPI using continuous measurements for moving surfaces and large deformations

submitted by Harsh Pokharna in partial fulfillment of the requirements for

the degree of Master of Applied Science

in Mechanical Engineering

Examining Committee:

Dr. Gary Schajer

Supervisor

Dr. Srikantha Phani

Supervisory Committee Member

Dr. Mattia Bacca

Supervisory Committee Member

Abstract

Deformation measurement is a common experimental need when testing the behaviour of mechanical devices. Such measurements are the basis for the evaluation of mechanical and thermal stresses, also for health monitoring of biological samples, study of vibrating parts of a mechanical component, and for quality testing of MEMS products. Optical methods like Electronic Speckle Pattern Interferometry (ESPI) are particularly attractive for practical applications because they are non-contact, sensitive and because they provide full-field displacement map over an extended area of the specimen. Conventional phase-stepping ESPI requires that the test object remains in the state of rest during the image acquisition, both before and after the deformation. This limits the use of ESPI to static or quasi-static measurements. Another limitation of conventional static ESPI is the measurable displacement range. Over large displacements ranging more than the size of a pixel, the speckles decorrelate and correct displacement information is lost. This project aims at developing a robust measurement technique to calculate surface displacement map for moving objects and to extend the range of measurable displacement. A newly developed algorithm that includes a technique involving camera exposure-synced phase stepper and mathematical interpolation is described. This method enables the extraction of instantaneous phase information using single interferograms. The test object is no longer required to be quasi-static during image acquisition. Every pixel in this method behaves like an independent displacement sensor. In addition, this method is computationally inexpensive. Some of the post-processing techniques are also discussed. A set of experimental results are discussed to validate the proposed technique.

Lay Summary

Small displacement measurements, in the scale ranging from nanometers to micrometers, are required in various engineering applications. The applications include machine design, measuring mechanical stresses, vibrations and residual stresses, material characterizations, biological health monitoring etc. Electronic Speckle Pattern Interferometry (ESPI) is a non-contact, full-field and non-destructive optical technique that uses a laser light to measure such deformations. The conventional ESPI methods are all suitable for static measurements. The object is required to be at rest before and after deformation. In real world applications, the test objects are always in motion or subjected to mechanical vibrations. The aim of this project is to develop an ESPI technique that can measure moving objects with good accuracy and precision. An Interpolated-ESPI method is proposed where a camera triggers a piezo-mounted mirror. The method is explained and is validated using several experimental data. Some of the applications are also demonstrated.

Preface

This work was first proposed by Dr. Gary Schajer and was conducted at the Renewable Resources Laboratory, Department of Mechanical Engineering at the University of British Columbia, Vancouver. I worked and developed the concept further. I developed the algorithms, electronics, test samples and detailed experimentation plans. I was also responsible for data collection and analysis and the manuscript composition.

The experiments described in Chapter 4 are all done in the lab. The test samples and other components were fabricated in the student machine shop in the Mechanical Department. Glenn Jolly, Technician and Electronics Shop supervisor, aided me with the design and debugging of the circuits used. The Phantom V611 high speed camera for some of the initial experimental work was made available to me with the help of Dr. Sheldon Green and Dr. Srikantha Phani.

The testing on organic wheat seed samples in Chapter 4 was done in collaboration with Darren, a former lab student.

Table of Contents

Abstract	iii
Lay Summary	iv
Preface	v
Table of Contents	vi
List of Tables	viii
List of Figures	ix
List of Symbols	xiii
List of Abbreviations	xiv
Acknowledgements	xv
Dedication	xvi
1. Introduction	1
1.1. Motivation	1
1.2. Introduction to Speckle Interferometry	3
1.3. ESPI for Dynamic Measurements	6
1.4. Objectives	7
1.5. Overview	8
2. Electronic Speckle Pattern Interferometry	9
2.1. Concept.....	9
2.2. ESPI Technique	11
2.3. In-Plane ESPI Setup	13
2.4. ESPI for Measuring Displacements.....	15
2.5. Phase-stepping	17
3. Continuous Measurements using Interpolated ESPI	26
3.1. Concept.....	26
3.2. Image acquisition.....	28
3.3. Calibration	30
3.4. Interpolation.....	31
3.5. Frame Acquisition Rate	36
3.5.1. Linear deformation.....	37

3.5.2.	Vibration	38
3.5.3.	Effect of change in vibration amplitude and frequency on intensity plots and on frame rate.....	39
3.6.	Real-Time Tracking of Average Intensity A and Modulation B	41
4.	Measurements and Validation.....	45
4.1.	Camera Frame Rate	45
4.2.	Linear Deformation	55
4.3.	Accuracy and Precision	57
4.4.	Vibration Measurement	59
4.5.	Test Sample Excitation using Custom Waveform.....	64
4.6.	Measurement of a Discontinuous Sample	65
4.7.	Post Processing.....	69
4.7.1.	Correction for low modulation.....	69
4.7.2.	Correction for saturated pixels.....	71
4.8.	Large Displacement Measurements.....	74
4.9.	Errors	79
4.10.	Application: Wheat Seed Health Monitoring	80
5.	Conclusions and Future Work	82
5.1.	Dynamic Measurement Technique and Its Features.....	82
5.2.	Applications.....	83
5.3.	Challenges	84
5.4.	Future Work.....	85
	References	87

List of Tables

Table 4-1: Experimental parameters for showing the effect of frame rate	46
Table 4-2: Experimental parameters for the experiment to measure linear fixed velocity displacement measurement	55
Table 4-3: Experimental parameters for the set of experiments to validate the accuracy of the proposed technique	58
Table 4-4: Accuracy and precision using total of 20 measurements divided into 4 cases of displacements	59
Table 4-5: Experimental parameters for testing vibrating samples (Increasing amplitude)	59
Table 4-6: Experimental parameters for testing vibrating samples (Increasing frequency)	62

List of Figures

Figure 1-1: (Top) The two waves interfere in phase and results in constructive interference...	4
Figure 1-2: (left) Beams shining on optically rough surface and (right) New wavefronts interfering.....	5
Figure 1-3: (left) A test sample, (centre) shone with a laser beam, and (right) speckles seen in the camera.....	5
Figure 2-1: In-plane sensitivity.....	13
Figure 2-2: Schematic of the in-plane set-up.....	14
Figure 2-3: In-plane interferometry set-up.....	14
Figure 2-4: Physical significance of fringes.....	16
Figure 2-5: (a) Four $\pi/2$ phase stepped images and (b) the intensity values of the highlighted pixel shown on its modulated intensity plot.....	18
Figure 2-6: Flowchart of the phase stepping process.....	20
Figure 2-7: Effect of noise during unwrapping. (a) noise with maximum amplitude less than π . (b) 2π phase discontinuity correctly located and (c) the data is unwrapped. (d) high amplitude noise added to the data (e) False detection of phase jumps (f) Error in phase unwrapping. Reproduced from [31].....	21
Figure 2-8: Intensity trend labelled with A and B, I_{\max} and I_{\min}	22
Figure 2-9: a) Fringe map with good visibility and b) Fringe map with poor visibility.....	24
Figure 2-10: (Top) A pixel with good modulation and (Bottom) A pixel with bad modulation.....	24
Figure 3-1: Change in intensity with time for a particular surface motion.....	27
Figure 3-2: Four intensity series of a pixel. Each intensity series is phase-stepped by 90° . The four asterisks show four 90° phase shifted intensities at time $t=0.28$ sec.....	27
Figure 3-3: Exposure signal (inverse) synced with PZT.....	29
Figure 3-4: Image acquisition using synchronized PZT mirror.....	29
Figure 3-5: Achieving desired calibration by changing the resistor values.....	30
Figure 3-6: Intensity series at a particular position of PZT mirror showing the acquired and missing images.....	31
Figure 3-7: Graphical representation of images acquired in the four intensity-series at every time instant. Images represented by asterisk are the acquired images. Circles represent the missing images. The green line represent a particular time instant.....	32

Figure 3-8: (Top) Intensity values acquired by the camera. Every consecutive intensity value is from the next phase stepped series. (Bottom) Using interpolation, missing data is generated, and all the four series are completed. The hollow markers represent the mathematically generated intensity values and the solid markers represent the acquired intensity values. 35

Figure 3-9: Sample waveform and the points needed to recreate it..... 36

Figure 3-10: The four figures show increasing excitation amplitude of the test sample depicted by orange colour and the theoretical intensity plots depicted in blue colour..... 39

Figure 3-11: The four figures show the theoretical response of intensity plots shown in blue colour on changing the excitation frequency of the test sample 39

Figure 3-12: Random arrangement of speckles in a group of pixels. Some of the pixels have speckle boundaries at the centre and some of them have bright speckle centres 42

Figure 3-13: Intensity plot of a pixel when the sample is displaced in a linear fashion with a constant velocity. The range of displacement is 22 micrometers. The instantaneous phase frequency remains constant and the camera frame rate depends on the velocity of motion ... 43

Figure 3-14: The intensity plot of a pixel when the sample is excited at a certain frequency. (Left) Vibration with a small amplitude and frequency 4Hz. Data is for 2 seconds 43

Figure 4-1: Test sample for demonstrating the effect of frame rate 46

Figure 4-2: (Top) Zoomed into 1 sec of interpolated intensities for all the four phase-stepped sequences, (Centre) Incremental phase change from one frame to the next with respect to time and, (Bottom) Calibration steps. This is the case when frame rate is 200fps and we have 8.2 frames/cycle/frame..... 48

Figure 4-3: (Top) Zoomed into 1 sec of interpolated intensities for all the four phase-stepped sequences, (Centre) Incremental phase change from one frame to the next with respect to time and, (Bottom) Calibration steps. This is the case when frame rate is 120fps and we have 5 frames/cycle/frame..... 49

Figure 4-4: (Top) Zoomed into 1 sec of interpolated intensities for all the four phase-stepped sequences, (Centre) Incremental phase change from one frame to the next with respect to time and, (Bottom) Calibration steps. This is the case when frame rate is 100fps and we have 4 frames/cycle/frame..... 50

Figure 4-5: (Top) Zoomed into 1 sec of interpolated intensities for all the four phase-stepped sequences, (Centre) Incremental phase change from one frame to the next with respect to time and, (Bottom) Calibration steps. This is the case when frame rate is 80fps and we have 3.3 frames/cycle/frame. This one is just beginning to have aliasing. Anything below this frame rate will not be useful..... 51

Figure 4-6: (Top) Zoomed into 1 sec of interpolated intensities for all the four phase-stepped sequences, (Centre) Incremental phase change from one frame to the next with respect to time

and, (Bottom) Calibration steps. This is the case when frame rate is 60fps and we have 2.5 frames/cycle/frame. Aliasing is evident in this case	52
Figure 4-7: (Top) Zoomed into 1 sec of interpolated intensities for all the four phase-stepped sequences, (Centre) Incremental phase change from one frame to the next with respect to time and, (Bottom) Calibration steps. This is the case when frame rate is 40fps and we have 1.6 frames/cycle/frame. Aliasing is extremely evident in this case	53
Figure 4-8: (Top) Zoomed into 1 sec of interpolated intensities for all the four phase-stepped sequences, (Centre) Incremental phase change from one frame to the next with respect to time and, (Bottom) Calibration steps. This is the case when frame rate is 25 fps and we have 1 frame/cycle/frame. This is to show the worst case when all the data is lost because only 1 frame is available every cycle.	54
Figure 4-9: Test sample for linear fixed rate motion measurement.....	55
Figure 4-10: (Top): Incremental phase change with respect to time. (Bottom): Measured phase plotted by adding the incremental phase values.	56
Figure 4-11 (Left): Zoomed in view of the sequences showing 8-9 points/cycle/sequence....	57
Figure 4-12: Comparison between the measured and actual linear displacement by plotting the displacements vs time	58
Figure 4-13: Vibration measurement sample excited using an electromagnetic coiled exciter	60
Figure 4-14: Study 1 with amplitude around 10 radians.....	60
Figure 4-15: Study 2 with amplitude around 11.3 radians.....	61
Figure 4-16: Study 3 with amplitude around 18.3 radians.....	61
Figure 4-17: Case 1 with the input as a triangular wave of frequency 2 Hz.....	63
Figure 4-18: Case 2 with the input as a triangular wave of frequency 4 Hz.....	63
Figure 4-19: Input wave to the electromagnetic actuator	64
Figure 4-20: Measured phase plot when the sample was excited using a modulated sine wave as the input to the electromagnetic actuator	64
Figure 4-21: Test sample used to demonstrate measurement of discontinuous samples.....	66
Figure 4-22: Wrapped phase maps. a) $t=0$ sec, beginning of the excitation, b) $t=0.16$ sec	66
Figure 4-23: Added phase maps. a) $t=0$ sec, beginning of the excitation, b) $t=0.16$ sec	67
Figure 4-24: Conventional unwrapped phase maps.....	68
Figure 4-25: Example of post-processing showing correction of low modulation pixel. a). Shows the interpolated intensities. A zoomed view of one of the low modulation area is shown.....	70
Figure 4-26: Example of post-processing where saturated pixel is corrected for.....	72

Figure 4-27: Case with extreme saturation of a pixel and its correction a). Shows the interpolated intensities. Saturated intensity region can be seen. b). Shows the modulation map of the pixel. c). Shows the incremental phase map before correction. d). Shows the incremental phase plot after post processing.73

Figure 4-28: Application of the technique measuring large deformation. The deformation measure is around 1300 radians that corresponds to 200 microns.....75

Figure 4-29: The unwrapped phase map for the same example of 200 microns displacement is shown.76

Figure 4-30: Second large displacement measurement example. The displacement here is 1000 microns. a). The interpolated intensities. Saturated intensity region can be seen.77

Figure 4-31: Displacement plot of the second example of 1000 microns. The measured value is 974 microns. This shows successful measurement of 1000 microns with around 2.5% error.78

Figure 4-32: Phase evolution of the seed with time. The data is yet to be studied further for interpretation81

Figure 4-33: (Left) Wrapped phase map of a healthy seed (Right) Wrapped phase map of copper treated inhibited seed sample81

Figure 5-1: Proposed 3D dynamic ESPI setup for future work85

List of Symbols

I – Intensity

I_i – Phase-stepped intensity before deformation

J_i – Phase-stepped intensity after deformation

Φ – Phase of light wave

$\Delta\Phi$ – Phase change due to surface motion

u – Complex electric field

U – Electric field amplitude

t – Time

r – Position vector

λ – Wavelength

f – Frequency of light wave

ω – Angular frequency

K – Sensitivity vector

A – Average intensity

B – Intensity modulation

Θ – Angle of incidence

S_A – Speckle size

$F\#$ – F number of the camera lens

μ – Visibility

V – Velocity of motion of test sample

F – Frequency of vibration of test sample

List of Abbreviations

3-D – Three Dimensional

CW – Continuous Wave

DIC – Digital Image Correlation

ESPI – Electronic Speckle Pattern Interferometry

FM – Frequency Modulated

FR – Frame Rate

LDV – Laser Doppler Vibrometry

MEMS – Microelectromechanical Systems

NDT – Non-Destructive Testing

PZT – Lead Zirconate Titanate

ROI – Region of Interest

SLM – Single Longitudinal Mode

Acknowledgements

I would like to thank my supervisor, Dr. Gary Schajer, for offering me this wonderful project. He has been an amazing guide, teacher and support throughout my degree providing with all the guidance and facilities. Thank you again Dr. Schajer for being the best supervisor one can ever wish for!

I would also like to offer my gratitude to the UBC Mechanical Engineering faculty and staff. I would like to thank Markus and Eric for the smartest ideas in the machine shop, Glenn for being a genius and helping me out with the electronics, and also Sean and Faheem from the Instrumentation shop. I also want to thank a former lab student, Darren for helping me out with some of the mex codes and innovative experimental ideas.

I want to express my sincere gratitude to the examination committee, Dr. Srikantha Phani and Dr. Mattia Bacca for their patience and time.

Furthermore, I would like to thank my lab colleagues Filipe Zanini Broetto, Juuso Heikinnen, Patrick Pan, Alan Walsh and Noushi Roushi for all the support and ideas.

I cannot forget to mention my friends here who made me feel at home in Vancouver: Claire Marie Grégoire (CMG :P), Miguel Villalba, Adriana Cabrera, Faisal Al-qurooni, Mike El-Koussefi, Sarah Crosby, Ratul Das, Somesh Bhatia, Prashant Mongia, Takshak Shetty, Chaitrali Salvi, Ankita Rathi, Fagun Jain and Saurav Sahu. Ketaki Sohani (Kitkat) and Nirmalendu Kuanr: You two deserve special thanks for bearing all my shenanigans and standing by my side. You guys are the reason I survived through all the difficult times away from home.

Last but not the least, I want to thank my parents and my family. They are the reason I am what I am today. This would not be possible without them. Hope I made you proud.

Dedicated to
Mummy and Papa for giving me the wings to fly!!!

“You have to dream before your dreams can come true.”

-A.P.J. Abdul Kalam

1. Introduction

1.1. Motivation

Displacement measurement is a common experimental requirement for designing and testing any mechanical components. The surface deformations considered in these deformations range from a few nanometers to several micrometers. These measurements are essential in industries like automobile [1], aerospace, microelectromechanical systems (MEMS) [2] and biological [3]. Typical applications include assessment of mechanical and thermal stresses, health monitoring of biological samples [4], study of vibrating parts of a mechanical component [5], and for quality testing of MEMS products. Recent developments in software technologies allow efficient modeling and simulation of mechanical deformations and transient phenomena like vibrations, heat transfer, impact and other dynamic events. These developments lead to an increasing need of accurate and precise physical measurement techniques that can verify the software models. Optical measurement techniques have many advantages [6] for such applications because they are non-destructive and non-contact methods [7][8][9]. In addition, they are capable of fast full-field measurements. Holographic interferometry, Electronic Speckle Pattern Interferometry (ESPI), Digital Image Correlation (DIC) are some of the frequently used optical techniques for full-field surface deformation measurements [10].

All the above-mentioned optical methods have very interesting and unique features. DIC measures displacements by correlating the stochastic pattern on a test specimen's surface captured before and after deformation. It is a very robust method and works perfectly well in the presence of random noise and vibration and therefore very good for operating environment [11]. ESPI is much more sensitive compared to DIC. The typical strain resolution of ESPI is around 10-20

micrometer/m as compared to 1000um/m for DIC [12]. On the other hand, when the displacements are bigger than the speckle diameter, there is a decorrelation problem between the reference and the deformed states, which sets the upper limit of measurement for ESPI [13].

The focus of this work is on ESPI because of its sensitivity and ease of computation. It can detect displacements up to fractions of wavelength of the laser used. Speckle interferometry dates back to 1970s as demonstrated in the work of Leendertz [14], followed by noticeable work by Burch et al. recording in-plane surface displacements [15]. Electronic Speckle Pattern Interferometry (ESPI) will be discussed extensively in Chapter 2. There are several different optical arrangements available that enable a wide range of full-field measurements to be made. Typical possible measurements include in-plane displacements, out-of-plane displacements and surface rotation.

Despite its versatility, conventional ESPI also has some limitations, notably that it is best suited to static or quasi-static measurements. This occurs because the typical ESPI measurement method involves acquiring at least three, most commonly, four phase-stepped images both before and after deformation. Phase stepping would be discussed in more details in the following chapter. There must be very little specimen motion during the acquisition of these phase-stepped images, thus limiting the surface velocities that can be accommodated to close to zero. In addition, the typical measurement range is only up to about 5-10 micrometers (typical speckle diameter size) [13]. It would certainly be a great advance to be able to take advantage of the sensitivity and versatility of the ESPI method while overcoming the speed and range limitations. The present work seeks to address these issues and proposes a practical procedure that enables high-speed measurements to be made over a greatly extended measurement range.

1.2. Introduction to Speckle Interferometry

1.2.1. Interference

Interference is an important observable property of light owing to its wave nature. Light can be thought of as a transverse electromagnetic wave propagating with specific amplitude, frequency and phase. When two light waves of intensities I_1 and I_2 combine, the resultant intensity I can be mathematically described as in equation 1-1

$$I = I_1 + I_2 + 2\sqrt{I_1 I_2} \cos \Delta\phi \quad (1-1)$$

where

I = Intensity

$\Delta\phi$ = Phase difference of the two waves

If the two waves combine in-phase, the resultant interference is constructive, and the outcome is a wave with higher amplitude and therefore, higher intensity. When the waves interfere out-of-phase, the interference is destructive and result in a lower intensity wave. For intermediate phase differences, the resultant intensity can be anything between the maximum and minimum intensities corresponding to partially constructive or destructive interference. Figure 1-1 shows the same concept in a graphical manner.

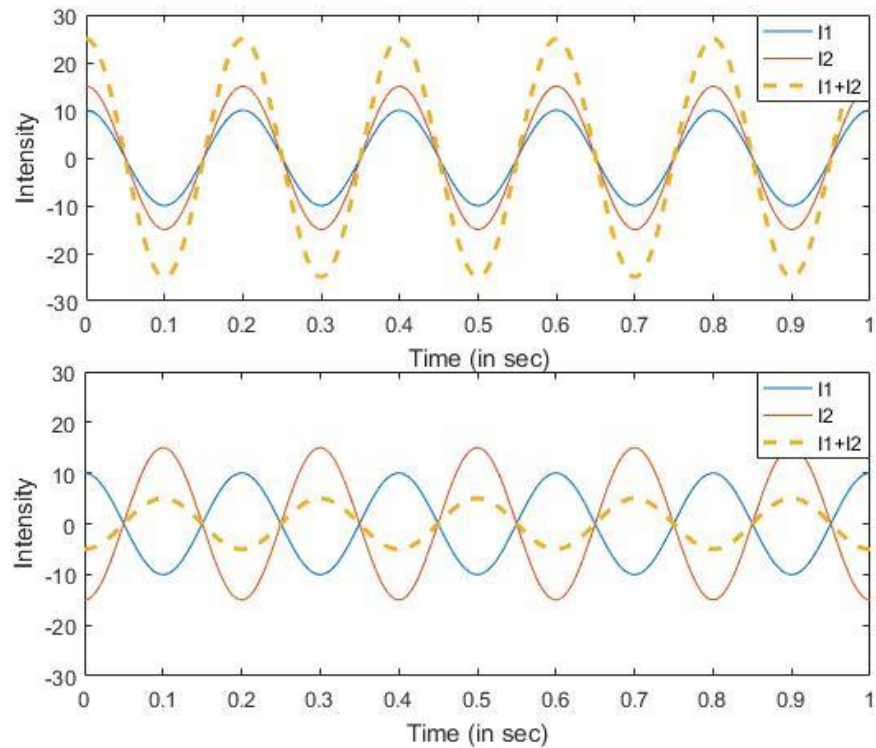


**Figure 1-1: (Top) The two waves interfere in phase and results in constructive interference
(Bottom) Out-of-phase interference resulting in destructive interference**

1.2.2. Speckles

When a coherent light source like a laser beam shines on a rough surface, the microscopic roughness of the surface acts as new point sources. These sources result in multiple wavefronts emitting from the surface in random directions (Figure 1-2). These wavefronts interfere with each other and give rise to random bright and dark spots. These random spots distribution looks like a grainy pattern. This pattern is called a speckle pattern and is as shown in Figure 1-3

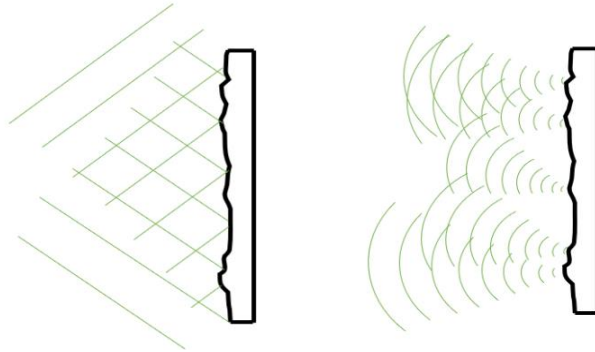


Figure 1-2: (left) Beams shining on optically rough surface and (right) New wavefronts interfering

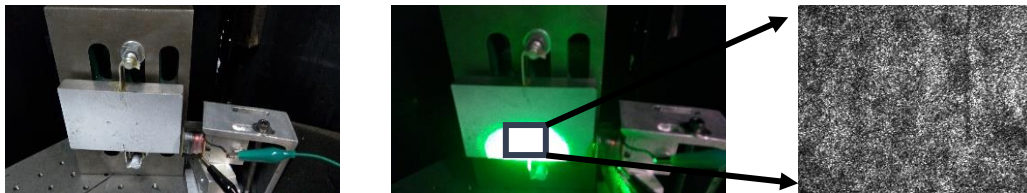


Figure 1-3: (left) A test sample, (centre) shone with a laser beam, and (right) speckles seen in the camera

1.2.3. Speckle interferometry

The speckle pattern as discussed in the above section has random spatial distribution, meaning that every speckle has the phase independent of other neighbouring speckles [16]. Every speckle carries important surface information at that point encoded as phase [17]. The surface motion results in relative path length difference of two interfering waves at that point. This path length difference manifests itself into phase difference and that phase difference manifests itself into intensity difference which looks like change in speckle pattern that is recorded by a camera. In fact, motion of any component in the optical set-up would result in path length difference and hence change in speckle pattern. Therefore, the set-up needs to be isolated and free of environmental noise and vibrations.

1.3. ESPI for Dynamic Measurements

Conventional ESPI techniques require the test object to be stationary both before and after deformation. This limits the use of the methods to quasi-static measurements. Some approaches proposed are based on multiple wavelengths [18], frequency scanning [19], or using a multicamera system [20]. These methods require expensive equipment and usually have very complex arrangements. Li et al. [21] implemented a Fourier Transform technique to calculate temporal deformation fields by introducing a carrier pattern into the interference field in ESPI measurement [22]. Transient deformation measurements are also demonstrated using stroboscopic [23] and pulsed-laser [24] illumination. Moore A.J. et al. demonstrated the use of short exposure and high frame acquisition rate of camera for measuring vibration and transient deformation using a continuous-wave (cw) laser [25].

There are a few methods that can measure transient deformations using single fringe image, but they still need multiple reference images to start with. A correlation calculation is carried on a small patch of pixels within two images and a regression coefficient is found which is used to determine the phase maps and eventually the deformation [26]. This method and some of the variations are described by Georgas and Schajer [27]. An, Carlsson [28] have presented a least-square algorithm to calculate phase change using only one image at a time. Lopez et al. also demonstrated vibration measurement using ultra high speed camera and correlation technique such that the deformation between two frames do not exceed a certain limit [29]. On the other hand, the competing technique for vibration measurement is Laser Doppler Vibrometry (LDV). The comparison is that ESPI is a full-field measurement technique using camera as the sensor while LDV is a point-based method using photo diode as the sensor. ESPI has superior spatial resolution whereas, LDV has much higher temporal resolution. In LDV, a scanning device is usually used to

perform 2D measurements which assumes that the measurement conditions remain invariant while sequential measurements are performed and therefore, it is only suitable to measure steady-state or well-characterized vibrations [30].

We propose a method using single camera and single continuous wave (CW) laser to measure transient events and to extend ESPI's typical upper limit of measurable deformation. The crux of the method is a technique where the camera exposure is in-sync with the phase stepper. Mathematical interpolation is used to extract instantaneous phase information using single images. This method has the luxury of measuring surface deformations even if the test object is moving. The robust ESPI measurement method is described with its advantages, limitations and applications.

1.4. Objectives

To summarize; The objectives achieved with this research are:

- To get full-field phase information (and hence the displacement) acquiring one frame at a time
- To achieve the deformation data free of directional ambiguity
- To extend the upper limit of measurable deformation using ESPI
- To successfully demonstrate the proposed technique and show the applications of the method

The main questions answered in this research are:

- Can ESPI be used to obtain both the amplitude and direction of motion of moving surfaces?

- Can ESPI be used for measuring displacements larger than speckle size?
- Can ESPI be used on a test object where the motion at one part of the object is completely independent of the other part on the sample? Or in other words, can we measure non-continuous deformations?

1.5. Overview

In **chapter 2**, there is an extensive discussion on ESPI. There is an explanation on the concepts of visibility and sensitivity direction. It also describes the phase-stepping algorithms necessary for ESPI measurements. Details of the experimental setup is also incorporated.

Chapter 3 follows with detailed description of our proposed method. Characteristic features of the method and necessary modifications to the standard ESPI setup to measure transient events are discussed.

Chapter 4 presents experimental results that shows the validity of the proposed method to measure in-plane surface deformations at high speed and increased measurement range. It also touches on the post-processing aspects of the algorithm where outliers are detected and corrected.

Chapter 5 concludes with a brief discussion of the research work presented in the thesis with mention of future work.

2. Electronic Speckle Pattern Interferometry

2.1. Concept

2.1.1. Interference Phenomenon

Light is a transverse electromagnetic wave, with specific amplitude, wavelength and phase. The direction of oscillation is determined by the polarization, which can be linear, circular, elliptical or non-polarized. The behavior of light is described by the Maxwell equations and one of the solutions to the wave equation is a sinusoidal function. The electric field u can be used to describe the light wave. In the case of a plane monochromatic wave, the field can be represented in the complex form as shown in equation 2-1.

$$u = U \cdot e^{i\varphi} \quad (2-1)$$

where U is the field amplitude, φ is the wave's phase component which depends on time t , position r , wavelength λ and frequency ω .

When similarly polarized light waves with electric fields u_1 and u_2 combine, the resultant electric field is the sum of the individual electric fields, as described in equation 2-2. When these two light waves are superimposed, the resultant amplitude either adds or subtracts depending on whether they meet in-phase or out-of-phase respectively. This is the common phenomenon called interference.

$$\begin{aligned} u_T &= u_1 + u_2 \\ u_T &= U_1 e^{i\varphi_1} + U_2 e^{i\varphi_2} \end{aligned} \quad (2-2)$$

The intensity is defined as the square of the field u . Therefore, the total intensity, measured over a period of time much larger than the period of the interfering waves, can be described by equation 2-3.

$$I_T = (u_T)^2$$

$$I_T = (u_T)(u_T^*) \quad (2-3)$$

$$I_T = (u_1 + u_2)(u_1^* + u_2^*)$$

$$I_T = u_1 u_1^* + u_2 u_2^* + u_1 u_2^* + u_2 u_1^* = I_1 + I_2 + 2\sqrt{I_1 I_2} \cos \Delta\varphi \quad (2-4)$$

Equation 2-4 corresponds to equation 1-1. $\Delta\varphi$ in equation 2-4 is the phase difference between the two interfering waves. The phase φ is described in equation 2-5.

$$\varphi_{(r,t)} = K \cdot r - \omega \cdot t + \phi_i \quad (2-5)$$

where K relates the phase to the spatial variation and ω relates the phase to the temporal variation. The term ϕ_i is the initial phase. Recalling the interference equation 2-4, it can be simplified in the form of equation 2-6.

$$I = A + B \cos(\varphi_0 + \varphi_s) \quad (2-6)$$

Phase changes cause the intensity of every speckle to follow the sinusoidal pattern indicated by equation 2-6, where A is the average intensity, B is the intensity modulation term and φ is the phase.

2.1.2. Speckle Phenomenon

When coherent light¹ illuminates an optically rough surface, the microscopic surface roughness gives rise to multiple new wave fronts which are re-emitted from the surface. The interference of all these waves produce a random intensity pattern, called Speckle. If the light source is not coherent, for instance white light, then speckles would not be observed because the presence of multiple wavelengths or broad wavelength spectrum would average out the intensity patterns.

The Electronic Speckle Pattern Interferometry (ESPI) technique is based on the speckle phenomenon and uses the random pattern characteristic and its properties to obtain information regarding the surface.

2.2. ESPI Technique

The ESPI technique uses phase information obtained from a speckle pattern to calculate small surface motions. The surface is illuminated by two coherent light beams, which are originated from the same source, to form an interference pattern described point by point by equation 2-4. The relative phase difference at any point in the surface depends on the optical arrangement and the surface state. If the surface moves, a path length difference between wave 1 and wave 2 results in phase modulation. The phase difference $\Delta\phi_s$ due to surface motion obeys equation 2-7.

$$\Delta\phi_s = \phi_2 - \phi_1 = (K_2 - K_1) \cdot \Delta r = K \cdot \Delta r \quad (2-7)$$

¹ Coherence is a measure of purity of the light. Coherence can be understood as the degree of correlation of a wave's phase with its phase at different instants of time, for temporal coherence, and at different points in space, for spatial coherence. For example, if the light's spectrum is very narrow, its initial phase will remain constant through longer periods of time and will correlate with itself for longer distances, resulting in a longer coherence length.

where $K = (K_2 - K_1)$ is a vector called sensitivity vector and Δr is the displacement vector. Notice that the scalar product in equation 2-7 implies that there will only be a phase difference due to the parallel component of Δr with K . Equation 2-6 can also be written as equation

$$I = A + B \cos(\varphi_0 + K \cdot \Delta r) \quad (2-8)$$

An important term describing the functionality of an interferometer is its sensitivity vector. The sensitivity vector describes the direction along which surface displacements are translated into phase changes. Therefore, the displacements measured by an ESPI interferometer are in the direction of its sensitivity vector K . This vector is dependent on the optical arrangement of the interferometer and is defined by the incidence angles of the two interfering beams.

Figure 2-1 shows an example of in-plane arrangement. The two beams have the same illumination angle θ . The wave vectors of the two interfering beams are given by K_1 and K_2 .

$$K_1 = \frac{2\pi}{\lambda} (\sin \theta \hat{x} - \cos \theta \hat{z}) \quad (2-9)$$

$$K_2 = \frac{2\pi}{\lambda} (-\sin \theta \hat{x} - \cos \theta \hat{z}) \quad (2-10)$$

$$\vec{K} = K_2 - K_1 = \frac{4\pi}{\lambda} \sin \theta \hat{x} \quad (2-11)$$

The phase change due to surface motion is then given by Equation 2-7. In the above-mentioned arrangement, the displacement required for a complete 2π phase change is $\Delta r = \frac{\lambda}{2\sin\theta} \hat{x}$. Since the set-up is in-plane, Δr would be referred to as Δx henceforth.

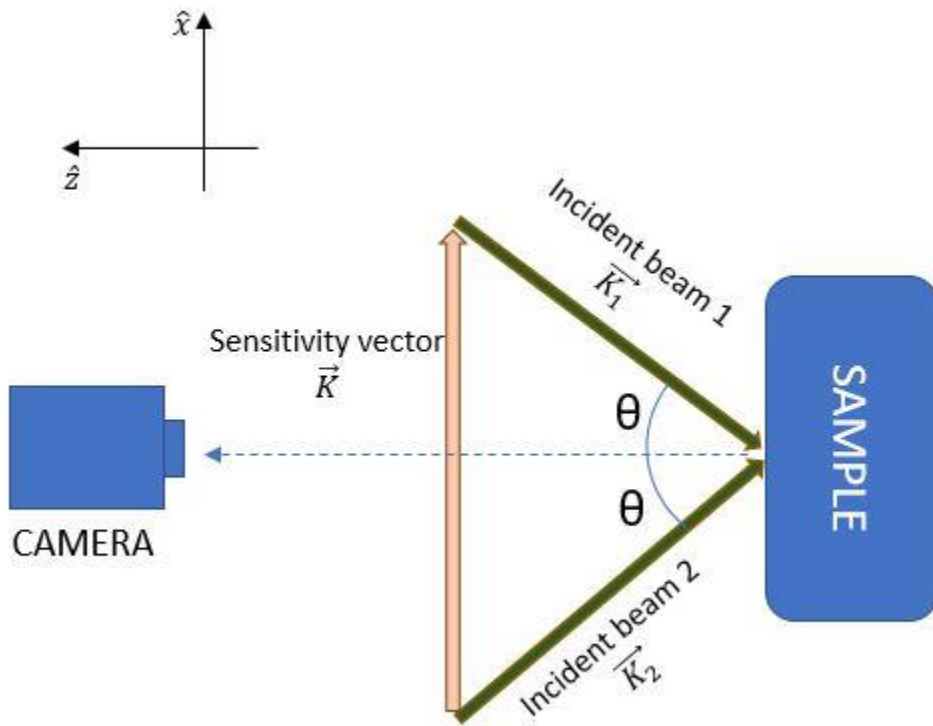


Figure 2-1: In-plane sensitivity

2.3. In-Plane ESPI Setup

The basic elements [31] of an interferometer are as follows:

- Light source
- Beam splitting element to split the light into two paths
- Different optical path lengths to create a phase difference
- Element where superposition of different waves take place
- Recording element or a detector

Figure 2-2 and Figure 2-3 illustrate the modified Mach-Zehnder interferometer typically used for in-plane ESPI. The light source used here is a JDS Uniphase single longitudinal mode (SLM) 532nm wavelength green laser. The beam splitter divides the laser beam into two coherent light beams. One beam goes to the test sample after being reflected by a fixed mirror while the second

goes through a piezo-operated mirror and then to the test sample. Both the beams arrive at the test surface at a 16.5° angle.

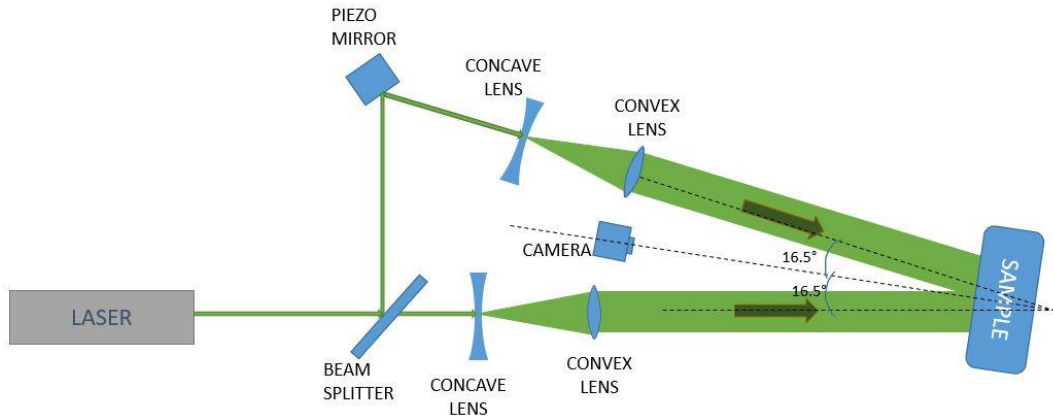


Figure 2-2: Schematic of the in-plane set-up

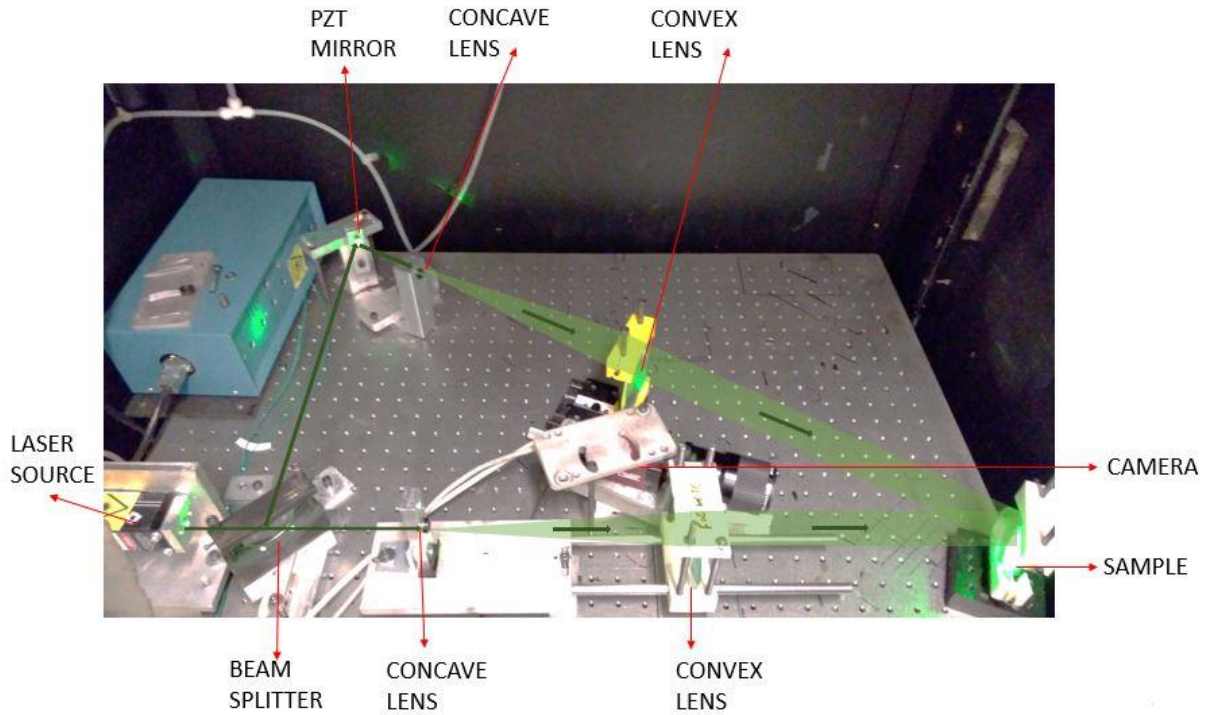


Figure 2-3: In-plane interferometry set-up

The configurations shown in Figure 2-3 has in-plane sensitivity. The incidence angles are same for both the beams.

2.4. ESPI for Measuring Displacements

Equations 2-7 and 2-11 describe the relationship between the displacement and the phase. Any change in the surface position along the direction of the sensitivity vector results in a relative phase change. This phase modulates the speckle pattern intensity, as described in equation 2-4. The camera detects this intensity modulation, which is later used to indicate the displacement of the measured surface.

Figure 2-2 and Figure 2-3 illustrate the illumination angle used in the in-plane setup. Both the beams arrive at 45° with the surface's normal direction. Thus, using equation 2-11,

$$|\vec{K}| = \frac{4\pi}{\lambda} \sin 16.5^\circ = 6.7 \text{ rad/micron} \quad (2-12)$$

Equation 2-12 indicates that a displacement of 1 micrometer along the sensitivity direction produces a phase change of 6.7 radians. Figure 2-4 shows an example. One fringe (white to white), corresponding to a phase change of 2π rad, is equivalent to a relative displacement of 0.936 micrometers.

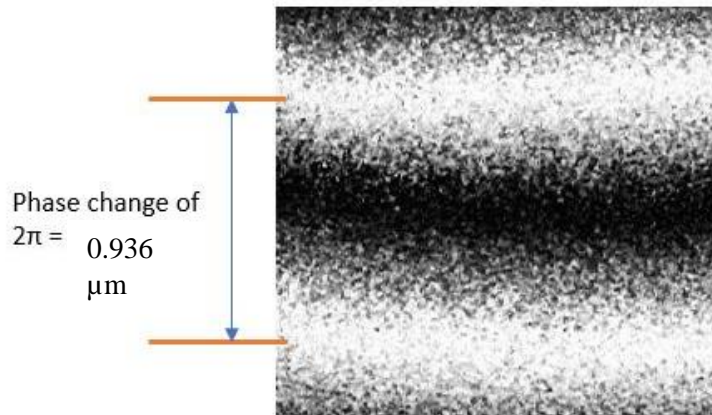


Figure 2-4: Physical significance of fringes

Equation 2-6 is used to solve for the phase difference. There are three independent variables, namely average intensity, modulation and phase. Thus, to solve for the phase, three images are required. A method called phase stepping, which introduces a known phase into the speckle pattern from one image to the next, makes it possible to determine the phase. For mathematical reasons, it is more convenient to take four images before deformation with 90° of phase difference, then repeat the same after deformation. The calculation of the phase difference between the reference and deformed states yields the relative displacements at the specimen's surface. The next section presents the phase stepping method in more details.

2.5. Phase-stepping

The most commonly employed phase-stepping method uses four images phase-shifted by $\frac{\pi}{2}rad$. The phase stepping is performed using a mirror equipped with a piezoelectric² transducer, henceforth referred to as PZT (Lead Zirconate Titanate). When a voltage is applied to the PZT terminals, it expands and translates the mirror in the process. The typical translation required for a phase-shift of $\frac{\pi}{2}rad$ is in the order of a fraction of a wavelength. To maintain the specified phase difference, there should not be any object motion during the acquisition of the phase-stepped images. This is the first challenge for dynamic measurements because the measured surface is in motion. In a typical static displacement measurement application, the phase stepping procedure is executed before and after deformation. Then, the phase of the reference state is subtracted from the phase of the deformed state. The difference of phase between the two states is proportional to the deformation in the sensitivity direction.

The four phase stepped images before deformation, namely, I_1, I_2, I_3 and I_4 are described by the following equations

$$I_1 = A + B\cos(\theta_i) \quad (2-13)$$

$$I_2 = A + B\cos\left(\theta_i + \frac{\pi}{2}\right) = A - B\sin(\theta_i) \quad (2-14)$$

$$I_3 = A + B\cos(\theta_i + \pi) = A - B\cos(\theta_i) \quad (2-15)$$

$$I_4 = A + B\cos\left(\theta_i + \frac{3\pi}{2}\right) = A + B\sin(\theta_i) \quad (2-16)$$

² A piezoelectric transducer is an element that suffers expansion when a positive voltage is applied on its terminals. It is used in applications where nanometric and micrometric positioning is required, due to its high precision.

Similarly, the images after deformation, J_1, J_2, J_3 and J_4 are acquired. Figure 2-7 shows the intensity modulation introduced by the phase stepping process. The highlighted pixel, in red, changes intensity as the phase shift is introduced, which can also be seen in the right side of the picture.

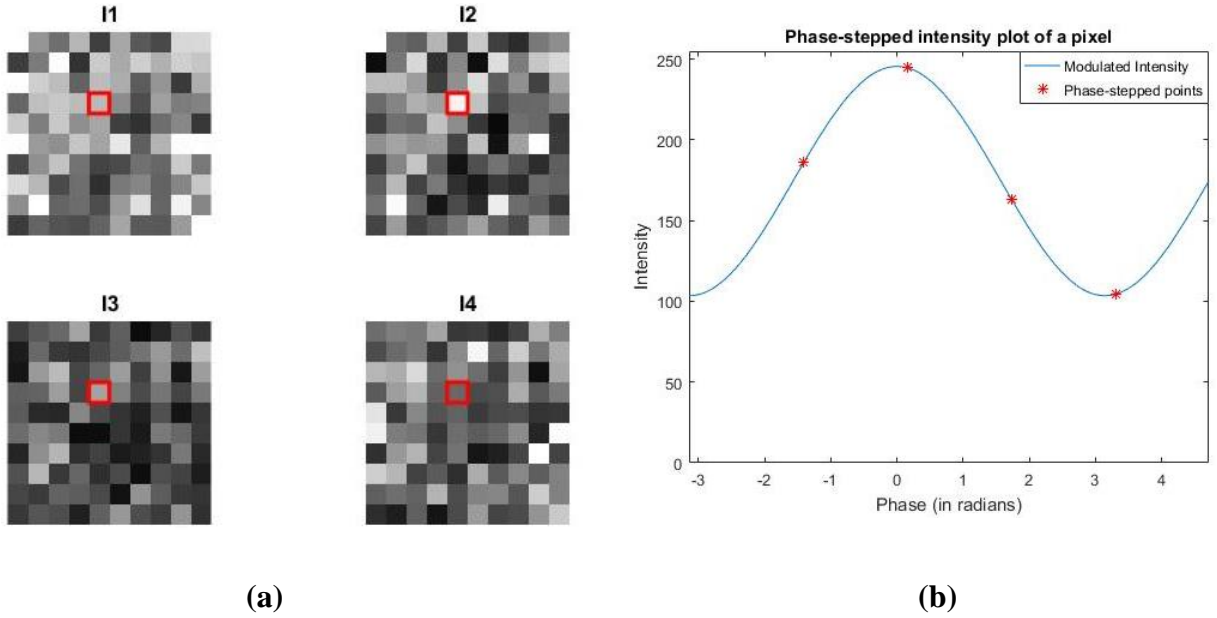


Figure 2-5: (a) Four $\pi/2$ phase stepped images and (b) the intensity values of the highlighted pixel shown on its modulated intensity plot

The phase difference can be obtained directly using the eight pictures at once. Equations 2-22 and 2-23 are used to obtain the direct phase difference. By defining

$$I_n = I_4 - I_2 \quad (2-17)$$

$$I_d = I_1 - I_3 \quad (2-18)$$

$$J_n = J_4 - J_2 \quad (2-19)$$

$$J_d = J_1 - J_3 \quad (2-20)$$

and using the trigonometrical identity,

$$\tan(\theta_j - \theta_i) = \frac{\tan(\theta_j) - \tan(\theta_i)}{1 + \tan\theta_j \tan\theta_i} \quad (2-21)$$

$$\tan(\theta_j - \theta_i) = \tan(\Delta\theta) = \frac{\frac{J_n}{J_d} - \frac{I_n}{I_d}}{1 + \frac{J_n}{J_d} \frac{I_n}{I_d}} = \frac{J_n I_d - I_n J_d}{J_d I_d + J_n I_n} \quad (2-22)$$

$$\Delta\theta = \tan^{-1} \frac{J_n I_d - I_n J_d}{J_d I_d + J_n I_n} \quad (2-23)$$

The computed phase change determined using equation 2-23 remains in the range $-\pi$ to π because of the cyclic nature of the inverse tangent function. Thus, the phase map obtained, is called a wrapped phase map. This wrapped phase map has discontinuities where the phase jumps from $-\pi$ to π or vice-versa as the phase changes increases or decreases, respectively. Consequently, the standard phase-stepping ESPI measurement is generally used to find relative displacements. Absolute displacements are possible in two cases: (1) if there is at least one fixed point (point with zero displacement in the sensitivity direction) in the region of interest and then all the other points will show displacements relative to that zero-displacement point; (2) if the displacement is less than one cycle or one wavelength of the laser used. The phase map obtained with this phase-stepping method is saw-tooth in characteristic because of the arctangent function. It is made continuous using well-defined spatial phase unwrapping algorithms [32]. Figure 2-6 summarizes the phase-stepping ESPI method in the form of a flowchart.

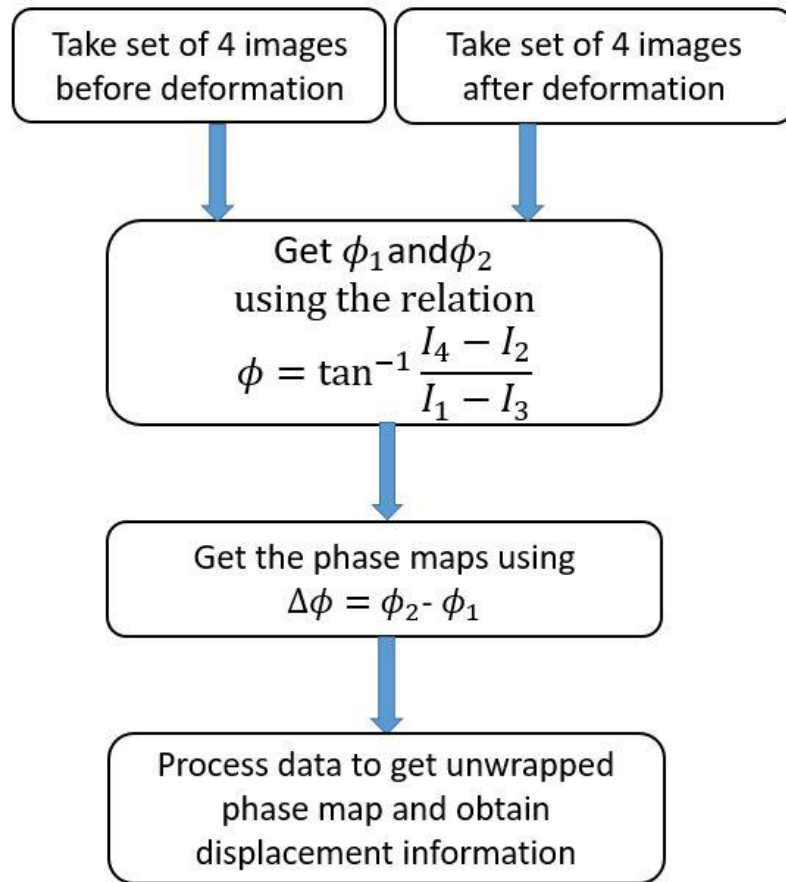


Figure 2-6: Flowchart of the phase stepping process

The ESPI technique is extremely sensitive to environmental noise and outside disturbances, so the unwrapping process needs to operate on noisy wrapped phase maps. Iterative smoothing of intensities is typically required when the signal-to-noise ratio or intensity modulation is low [33][34]. Unwrapping under these circumstances introduces errors in the form of phase jumps. Figure 2-7 shows unwrapping of both ideal and noisy data. The proposed method described in the next chapter does not require phase unwrapping. Thus, avoiding phase unwrapping errors, is another advantage of the method.

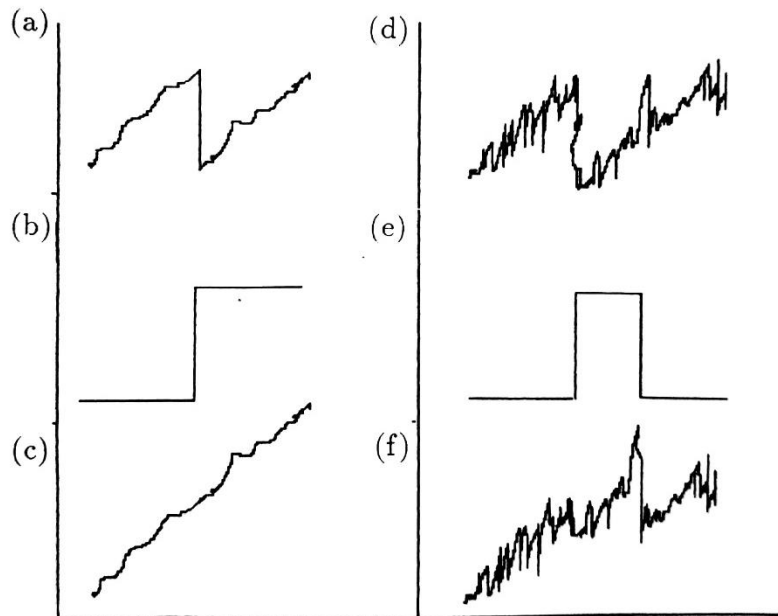


Figure 2-7: Effect of noise during unwrapping. (a) noise with maximum amplitude less than π . (b) 2π phase discontinuity correctly located and (c) the data is unwrapped. (d) high amplitude noise added to the data (e) False detection of phase jumps (f) Error in phase unwrapping. Reproduced from [31].

There are many factors that influence ESPI measurement. Among the most important are visibility, which is a consequence of coherence and relates to the measurement quality, and decorrelation, which influences the measurement range and limits the magnitude of displacements that can be measured.

2.5.1. Visibility

Visibility is a direct consequence of coherence [35]. The intensity value in a pixel correlates directly with the instantaneous phase of the corresponding speckle. Figure 2-8 graphically shows this relationship. If the temporal coherence or spatial coherence is limited, the phase correlation of

the wave with itself is reduced and the interference modulation term B averages to nearly zero. In this case, the modulation is reduced drastically.

To evaluate visibility, the intensity modulation is analyzed as a function of phase change. The higher the difference between the maximum and minimum intensities achieved, the higher the visibility. Figure 2-8 illustrates the concept.

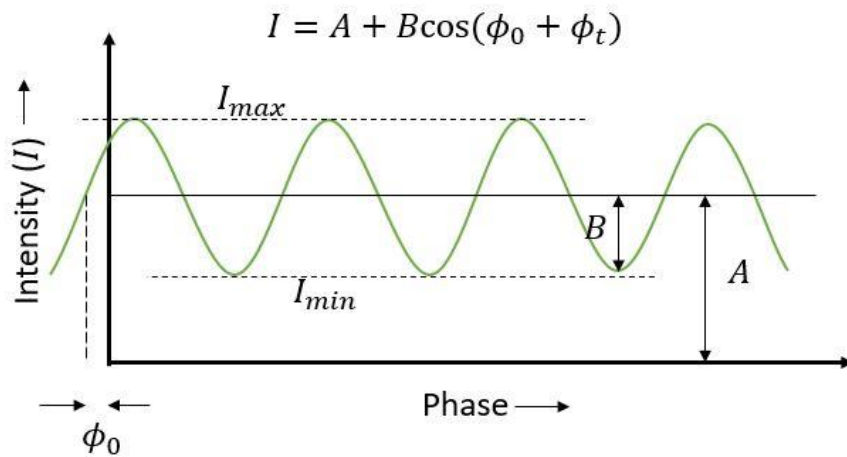


Figure 2-8: Intensity trend labelled with A and B, I_{max} and I_{min}

The maximum intensity I_{max} occurs when the two beams interfere in-phase, i.e., $\phi=2n\pi$

$$I_{\max} = I_1 + I_2 + 2\sqrt{I_1 I_2} \quad (2-24)$$

Similarly, the minimum intensity I_{min} occurs when the two beams interfere out-of-phase, i.e.,

$$\phi=(2n+1)\pi$$

$$I_{\min} = I_1 + I_2 - 2\sqrt{I_1 I_2} \quad (2-25)$$

where n = 0,1,2,3,.....

The visibility can then be defined as

$$\mu = \frac{I_{\max} - I_{\min}}{I_{\max} + I_{\min}} = \frac{B}{A} = \frac{2\sqrt{I_1 I_2}}{I_1 + I_2} \quad (2-26)$$

The visibility values for speckles can be calculated using equation 2-26 and can range between 0 and 1. Typically, $\mu < 0.2$ gives noisy or poor fringes. The Figure 2-9 shows two fringe maps, one with good visibility and the other with poor visibility. It can be seen that the one with poor visibility has more noise, resulting in a grainy fringe map. Visibility can be controlled by adjusting the speckle size, which in turn, is driven by the numerical aperture of the lens and the wavelength of the light. Average speckle size on the screen is given by the equation 2-27 [13]. If the speckle size is too small, many speckles can occupy a pixel and average to a middle value, resulting in low modulation. On the other hand, if the speckle size is too big, each speckle covers many pixels and so reduces the spatial resolution of the result. Ideally, the desirable speckle size approximately equals the pixel size.

$$S_A = 1.2 * \lambda * F\# \quad (2-27)$$

Where S_A : Average speckle size

$F\#$: F number on the camera lens that is a measurement of aperture size

Figure 2-10 exemplifies that good visibility produces substantial variation of intensity with phase change. The benefit proportionated by high visibility is that it makes it easier to determine phase differences, proportional to displacements, based on the intensity measurements.

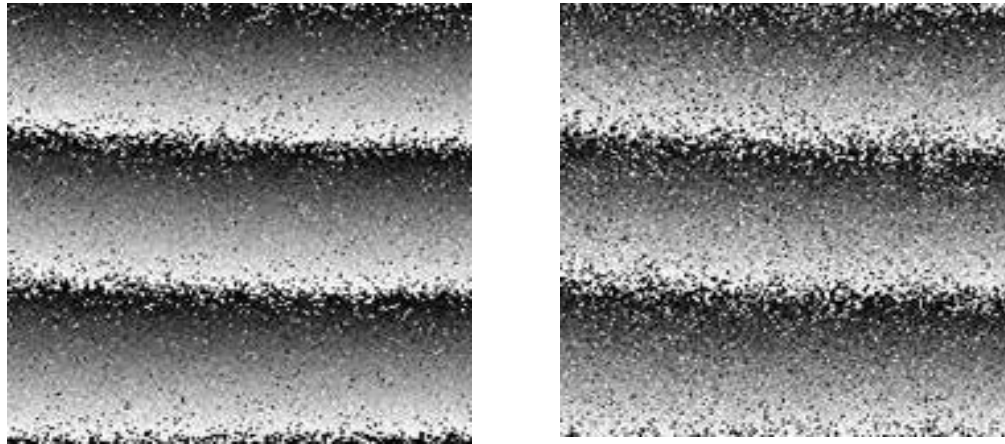


Figure 2-9: (Left) Fringe map with good visibility and, (Right) Fringe map with poor visibility

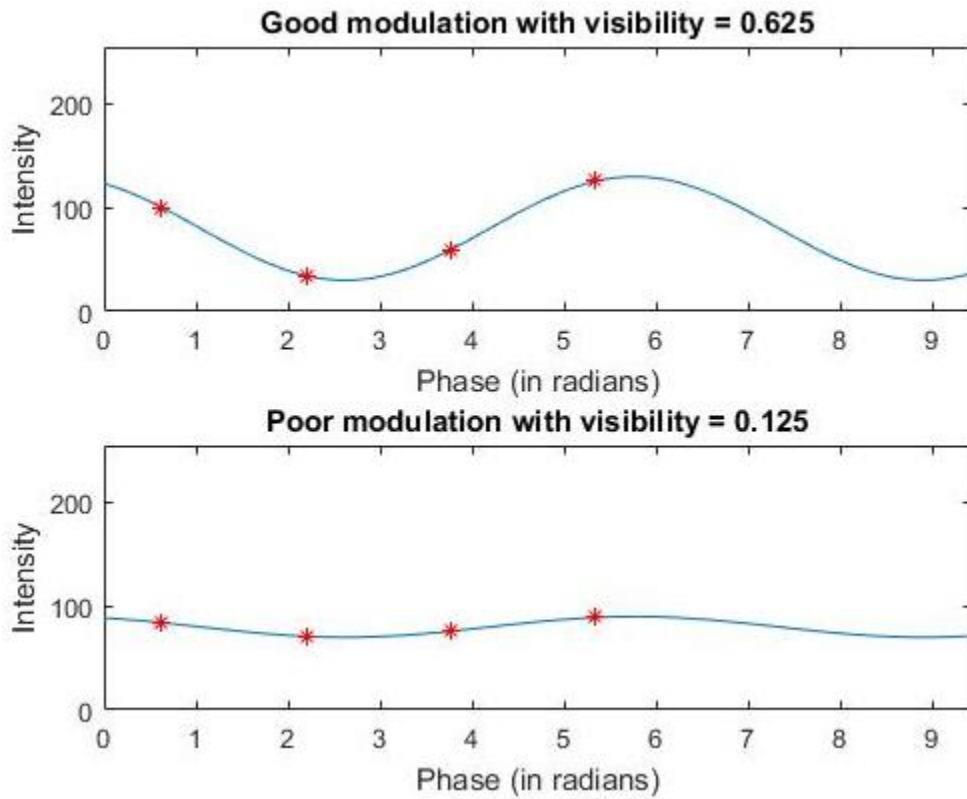


Figure 2-10: (Top) A pixel with good modulation and, (Bottom) A pixel with bad modulation

2.5.2. Decorrelation

Speckle images are composed of overlapping speckles. Surface displacement causes the speckles to move laterally as well as to change in phase. If the surface displacement is such that a speckle completely shifts its position from one pixel to another, the initial phase of the new speckle in the pixel is completely different and independent of the initial phase of the original speckle in the same pixel. The new phase after displacement then cannot be related to the initial phase before displacement. This condition is called decorrelation and poses a significant challenge when using ESPI. It sets a limit to the displacement that can be measured. As discussed in section 2.5.1, the ideal speckle size is around the size of a pixel. For a typical camera, this sets the upper limit of displacement to around 10 microns. There are some indirect methods used to measure big displacements. For example, the measurement can be divided into smaller steps and the displacement results can be added at the end to give the total displacement; Digital Image Correlation (DIC) can be used to mathematically re-correlate the images [36] and then apply ESPI technique.

The following chapter introduces a novel technique for addressing these challenges. It involves modifying the way that the phase stepping is done so as to enable measurements to be made even when the test object is in motion.

3. Continuous Measurements using Interpolated ESPI

3.1. Concept

During dynamic ESPI measurements, surface movement causes continuous changes in the measured phase. These phase changes in turn cause local intensity changes and form a time sequence of intensity at each pixel. Figure 3-1 shows a schematic example of measured light intensity changing in a sinusoidal manner following equation 2-6. To extract the associated phase information, at least three 120° phase-stepped images are needed at every point of time. However, it is more common to use four 90° phase-stepped images to provide greater measurement robustness. Figure 3-2 shows the four required intensity series of a pixel from time $t=0s$ to $t=1s$. The asterisks on the figure represent the four phase-stepped intensities of the pixel desired at a random time instant. This is not available in conventional method because only one phase image can be captured at a time.

By using a single monochrome camera and single a laser system, it is possible to capture only one time-sequence of intensity for every pixel. The main idea of the proposed method is to make use of a phase-stepper synchronised to the camera. The phase-stepper, in this case, is a PZT mirror synchronized with the camera. In the proposed method, every successive image is from the next phase-stepped intensity sequence. At the end of the acquisition, there are four periodically sampled phase-stepped intensity sequences. Although periodically sampled, there is enough information to complete mathematically all the four required time-sequences of intensity for every pixel. Polynomial interpolation is used to find the missing intensities. Once complete series of intensities are obtained, the standard phase-stepping algorithm is used to calculate instantaneous phase.

The synchronized acquisition process permits continuous ESPI measurements using only one camera and a single cw laser source while the test object is in motion. The details of the method describing image acquisition and mathematical interpolation, along with the advantages, and also the limitations on the surface velocities are discussed in detail in the following sections of the chapter.

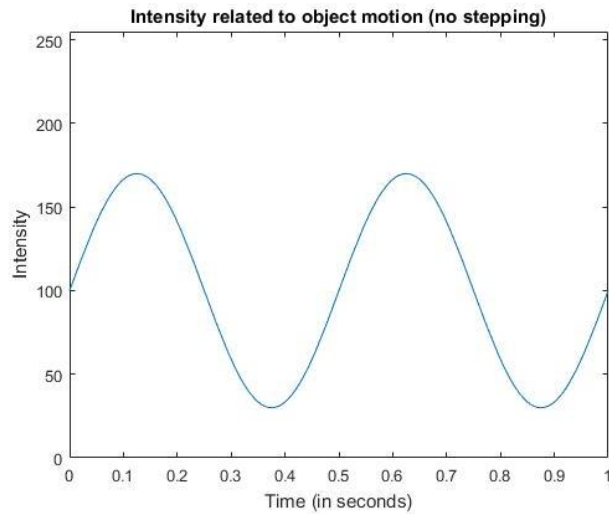


Figure 3-1: Change in intensity with time for a particular surface motion

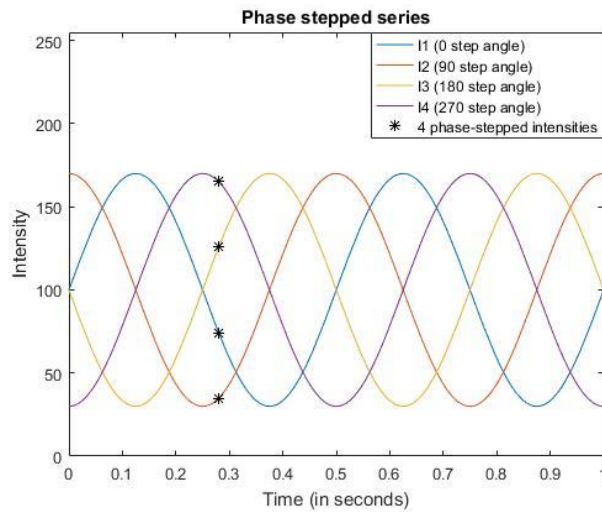


Figure 3-2: Four intensity series of a pixel. Each intensity series is phase-stepped by 90°.

The four asterisks show four desired 90° phase shifted intensities at time t=0.28 sec

3.2. Image acquisition

In addition to the acquired images, machine vision cameras also provide timing information and strobe outputs with microsecond accuracy. The trigger signals correspond to the frame acquisition rate of the camera. Every trigger cycle is composed of exposure and readout cycles. The exposure pulse indicates when the camera sensor integrates the light and captures an image and the readout indicates when the image data is readout from the sensor. Every time the camera exposes, it sends out a logic pulse called strobe. The exposure signal triggers the PZT mirror. After every image, the PZT is stepped up by 90° . Figure 3-3 shows the trigger timing signal synced with the PZT. The yellow signal in the figure is the strobe output signal from the camera. The blue signal corresponds to the voltage input to the piezo. The PZT input voltage is change at the start of the readout pulse. By the time the exposure pulse starts, PZT input voltage is stable. In other words, as soon as the camera finishes integrating light for one image, the signal activates the PZT mirror to only then trigger the next integrating cycle.

After acquiring the first image, PZT steps up by 90° and the second image is acquired. PZT mirror steps up again by another 90° and the third image is acquired, followed by the same procedure to capture the fourth frame. After the fourth frame, PZT mirror comes back to the original position and the fifth image is acquired. Every 4th image lies on the same time-sequence of intensity. The process continues till desired number of images are recorded. The four time-series of intensity are represented by I_1 , I_2 , I_3 and I_4 . Figure 3-4: Image acquisition using synchronized PZT mirror shows the time sequences. It is possible to see that the first frame lies on the I_1 series (blue), the second image lies on I_2 (red), the third on I_3 (yellow), The fourth image lies on I_4 (purple). The fifth image lies on I_1 and so on. The image data acquired for the recorded duration

is processed to mathematically generate the missing frames and complete the four phase-stepped images at every time instant.

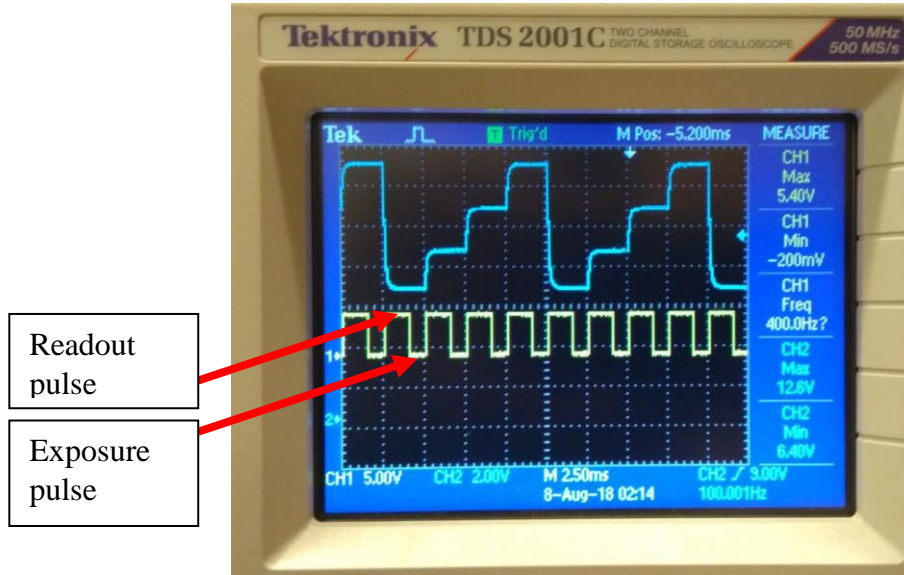


Figure 3-3: Exposure signal (inverse) synced with PZT

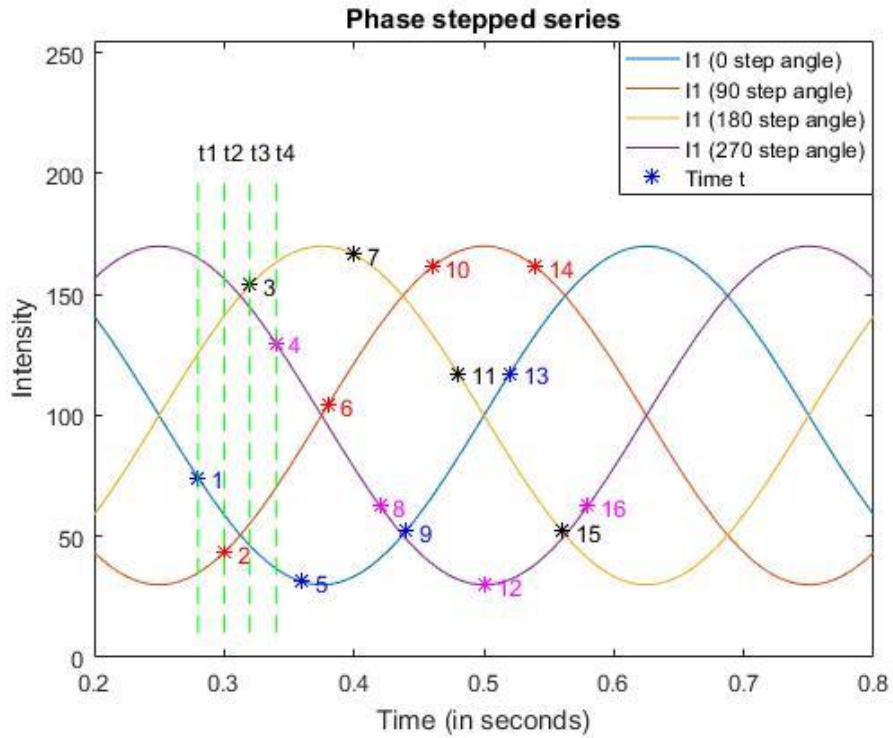


Figure 3-4: Image acquisition using synchronized PZT mirror

3.3. Calibration

When the PZT mirror assembly is energized by applying a voltage across its terminals, it expands or contracts by an amount approximately proportional to the applied voltage. Consider a sequence of four applied voltages V_1 , V_2 , V_3 and V_4 . At these voltages, the PZT mirror moves by incremental distances corresponding to the four phase-steps. The circuit that connects the camera with the phase-stepper comprises a digital counter that sequentially cycles a logical signal among four outputs. Each of the outputs are connected to resistors that alter the gain of a voltage amplifier circuit so that a repeating sequence of four voltage steps is output. The resistors can be adjusted so that the voltage output looks like a step ladder as shown in the Figure 3-3.

For calibration purpose, a set of images is captured and processed in MATLAB. According to the result, the variable resistors are adjusted, and the process is repeated until the step angles between consecutive images are 90° . This is done using the correlation method described in [27]. Figure 3-5 shows how the step angles change during the calibration process.

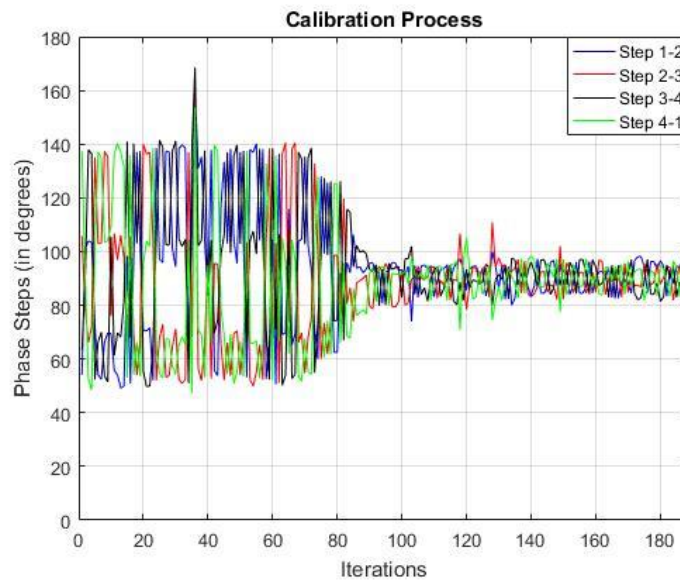


Figure 3-5: Achieving desired calibration by changing the resistor values

3.4. Interpolation

Once the acquisition process is complete, the four periodically sampled phase-stepped intensity sequences must be processed to interpolate the intermediate points. Figure 3-6 shows one of the series I_1 for a pixel. Every fourth image is captured in the I_1 intensity series. Similarly, the series I_2 , I_3 and I_4 are also partially complete. The images marked by asterisk are the ones which the camera acquires. The ones marked with circles are the missing images. At this point, the idea of mathematical interpolation is used to artificially generate the missing images and complete all the intensity series.

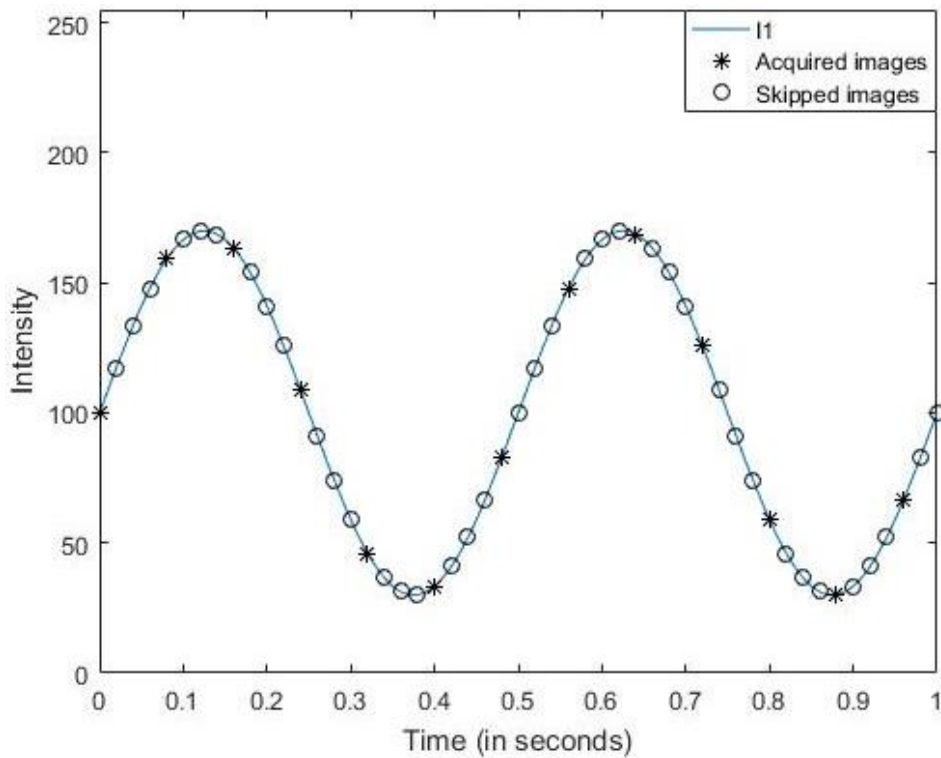


Figure 3-6: Intensity series at a particular position of PZT mirror showing the acquired and missing images

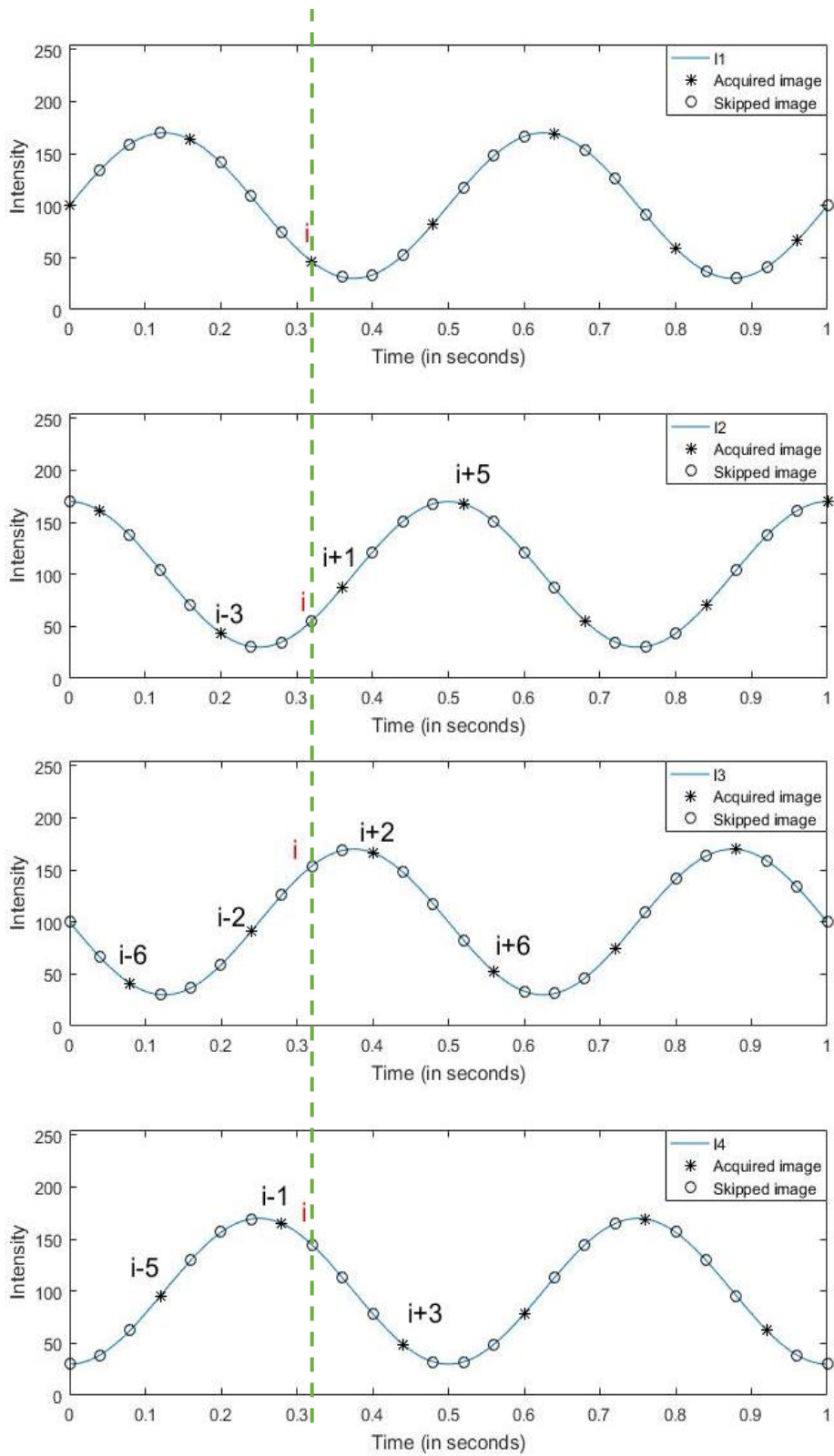


Figure 3-7: Graphical representation of images acquired in the four intensity-series at every time instant. Images represented by asterisk are the acquired images. Circles represent the missing images. The green line represent a particular time instant

Consider a time instant represented by the green line shown in the Figure 3-7: Graphical representation of images acquired in the four intensity-series at every time instant. Images represented by asterisk are the acquired images. Circles represent the missing images. The green line represent a particular time instant. Every intensity sequence for a small time-interval is considered to be a 2nd degree curve represented by the equation 3-1.

$$I = a + b(x) + c(x)^2 \quad (3-1)$$

For the intensity series I_1 , the first image is J_k and is acquired by the camera. Therefore, interpolation is not needed for that time instant for I_1 .

$$I_1(t_k) = J_k \quad (3-2)$$

For the series I_2 , the image is mathematically generated using the nearest images acquired in that series.

$$I_2(t_k) = \frac{5J_{k-3} + 30J_{k+1} - 3J_{k+5}}{32} \quad (3-3)$$

Similarly, I_3 and I_4 are given by

$$I_3(t_k) = \frac{-J_{k-6} + 9J_{k-2} + 9J_{k+2} - 3J_{k+6}}{16} \quad (3-4)$$

$$I_4(t_k) = \frac{-3J_{k-5} + 30J_{k-1} + 5J_{k+3}}{32} \quad (3-5)$$

After interpolation, four phase stepped intensities are available for every time instant k (shown in the Figure 3-8), which implies that the instantaneous phase at t_k is known. Incremental phase is then calculated as discussed in section 2.5 using equation 2-23.

Figure 3-8 (Top) shows the acquired intensities and; (Bottom) shows the complete intensities for all the four phase sequences using mathematical interpolation. The four colours correspond to the four phase-stepped images. The solid black markers in the figure on top match with the solid colour markers in the figure at the bottom. The solid markers represent acquired image intensity values. The hollow markers on the bottom are the mathematically obtained intensity values to complete the four phase-stepped intensity series. Every fourth acquired image lies on the same phase-stepped sequence shown in the figure at the bottom. On any dotted vertical line, there are four markers (Figure 3-8: bottom). One is solid that represents the acquired value and the other three are hollow representing mathematically generated values. This is the central idea of the proposed Interpolated-ESPI method.

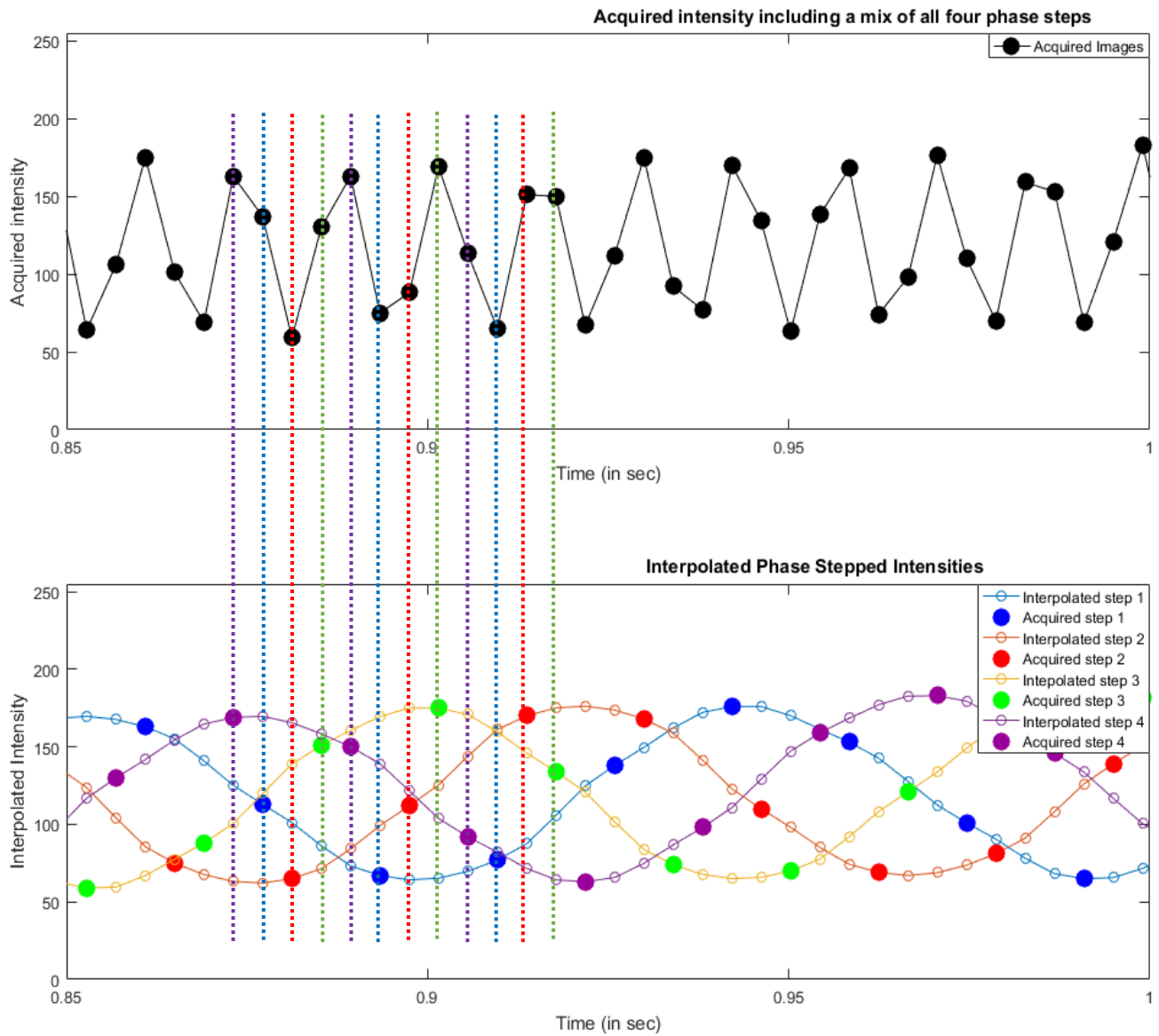


Figure 3-8: (Top) Intensity values acquired by the camera. Every consecutive intensity value is from the next phase stepped series. (Bottom) Using interpolation, missing data is generated, and all the four series are completed. The hollow markers represent the mathematically generated intensity values and the solid markers represent the acquired intensity values.

3.5. Frame Acquisition Rate

For dynamic ESPI, frame rate is a key camera property. To recreate a sinusoidal waveform as shown in Figure 3-9, it was found experimentally that at least 4 points per cycle at each phase step are needed to achieve stable results. Fewer points than that results in aliasing in the data set. This detail is explored experimentally in the following chapter. Recalling that a total of four waveforms need to be recreated corresponding to the four phase-stepping angles, the final criterion then becomes at least 16 measurements 16 frames/cycle. This equals approximately 0.4 radians (23°) per frame. The recommendation is to have 20 frames/cycles.

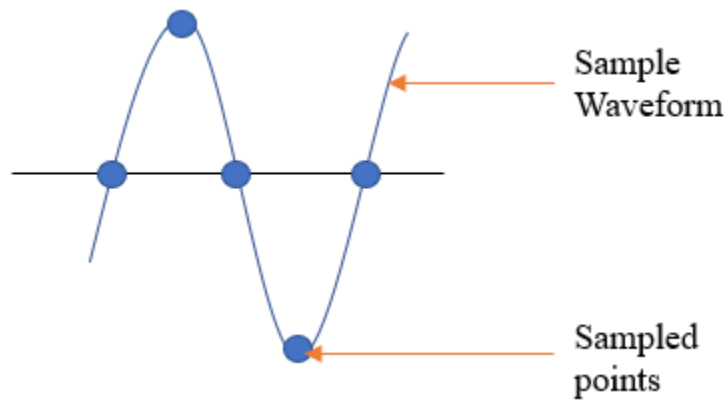


Figure 3-9: Sample waveform and the points needed to recreate it

Mathematically the instantaneous phase frequency is the slope of the phase and phase is nothing but the motion of the test sample. The instantaneous phase frequency F is therefore given by,

$$F = \left| \frac{d\phi}{dt} \right| \text{ (rad/sec)} \quad (3-6)$$

Differentiating equation 2-7,

$$\frac{d\phi}{dt} = K \cdot \frac{dx}{dt} \quad (3-7)$$

3.5.1. Linear deformation

For linear deformation, Δx in equation 2-8 varies with time as

$$\Delta x = V * t \quad (3-8)$$

where V is velocity is in microns per second and t is time. Substituting Δx , the intensity equation becomes,

$$I = A + B \cos(\varphi_0 + K.V.t) \quad (3-9)$$

$$F = K \cdot \frac{dx}{dt} = K.V \text{ (rad/sec)} \quad (3-10)$$

As seen from equation 3-10, the instantaneous phase frequency F for every pixel in this loading case is directly proportional to the velocity of motion and sensitivity of the setup. Therefore, frame rate of the camera is directly proportional to K (Sensitivity) and rate of displacement.

The minimum recommended Frame Rate (FR) in this case can then be estimated as shown below.

$$FR > \left| K.V \cdot \frac{20}{2\pi} \right| \text{ (frames/sec)} \quad (3-11)$$

Considering the sensitivity of the set-up and the arrangement,

$$FR > |21.32 * V| \text{ (frames/sec)} \quad (3-12)$$

The absolute minimum frame rate would be

$$FR_{min} \approx \left| K.V \cdot \frac{16}{2\pi} \right| \approx |17 * V| \text{ (frames/sec)} \quad (3-13)$$

For instance, if the test sample is moving at 12 micrometers/sec, then the recommended frame rate should be greater than 255 fps and the absolute minimum frame rate would be 204 fps.

3.5.2. Vibration

In this loading case, Δx in the equation 2-8 varies with time as

$$\Delta x = C \cdot \sin(2\pi ft) \quad (3-14)$$

Where C is the amplitude of vibration (in micrometers) of the sample, f is the frequency of the sample's vibration and t is the time. Substituting Δx , the intensity equation becomes

$$I = A + B \cos(\varphi_0 + C \cdot \sin(2\pi ft)) \quad (3-15)$$

The instantaneous phase frequency in this case is given by,

$$F = K \cdot \frac{dx}{dt} = K \cdot 2\pi f C \cos(2\pi ft) \text{ (rad/sec)} \quad (3-16)$$

As seen in equation 3-16, the phase frequency is a function of sensitivity K , vibration amplitude C and vibration frequency f . The maximum instantaneous phase frequency is $2\pi f K C$.

$$FR > \frac{20}{2\pi} \cdot 2\pi f K C \quad (3-17)$$

$$FR > 134fC \quad (3-18)$$

$$FR_{min} \approx 107fC \quad (3-19)$$

For instance, if the test sample is vibrating with amplitude 2 micrometers and frequency 2 Hz, the recommended frames rate is 536 fps approximately to detect the points with maximum velocity on the wavefronts. The absolute minimum frame rate would be around 428 fps below which it will not be possible to measure the particular vibrating sample.

If the frame rate is less than the set criteria, under sampling will happen and there will be loss of phase information. The experiments validating the above-mentioned criteria are conducted and are discussed in the next chapter. The next sub-section shows how the intensity plots change when the excitation amplitude and the excitation frequency of the test sample are changed.

3.5.3. Effect of change in vibration amplitude and frequency on intensity plots and on frame rate

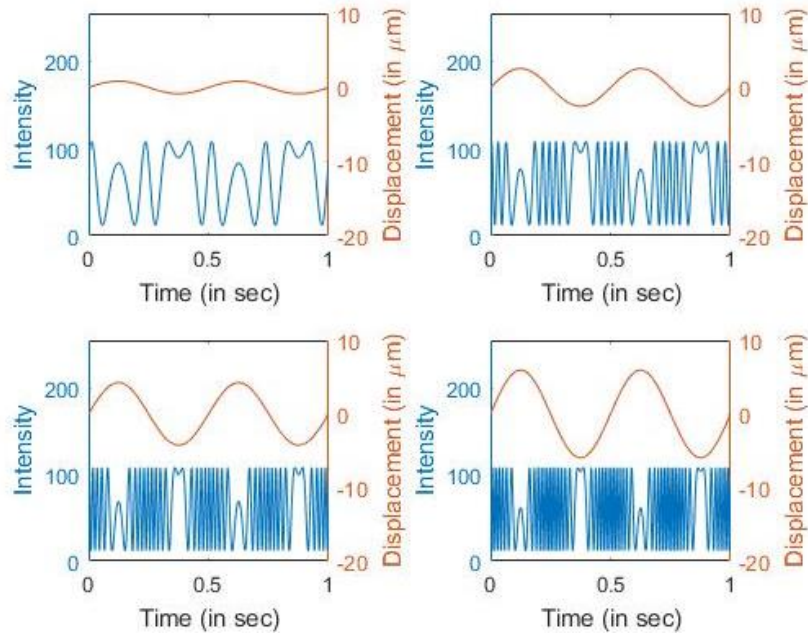


Figure 3-10: The four figures show increasing excitation amplitude of the test sample depicted by orange colour and the theoretical intensity plots depicted in blue colour

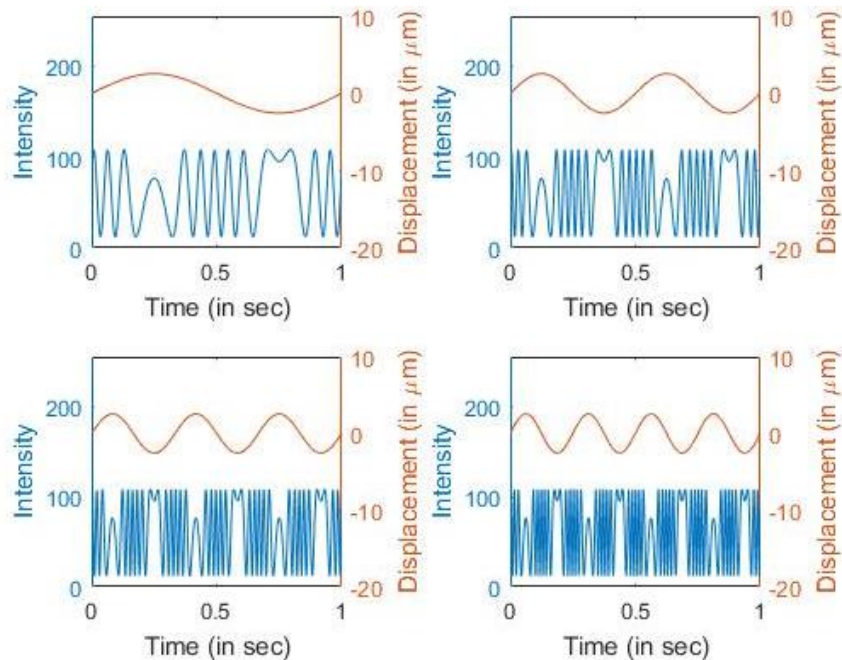


Figure 3-11: The four figures show the theoretical response of intensity plots shown in blue colour on changing the excitation frequency of the test sample

Understanding how the intensity changes with change in the excitation parameters of the sample is important for dynamic ESPI. Figure 3-11 shows the same concept. The orange plots show the displacement of the sample that correlates directly to the motion of the sample and the blue plots show the intensity. The top set of images in the figure depicts change in intensity with the change in excitation amplitude of the test sample while keeping the excitation frequency constant at 2Hz. In this case, the number of repeating cycles of intensity modulation within the time frame of 1 sec remains the same i.e. 2. The pattern of intensity modulation becomes denser on increasing the amplitude, with more number of peaks and valleys within each cycle. This corresponds directly to the increase in number of fringes within each cycle. The second case demonstrates effect of increasing the excitation frequency while keeping the amplitude of vibration the same. It is seen that the number of peaks within each cycle remains the same but the number of repeating cycles of intensity modulation within the time frame of 1 sec increases. It can be seen that the intensity waves behave like Frequency Modulated (FM) waves in case of vibrating sample. The instantaneous intensity modulation rate is the slope of the displacement plot. It is shown that in both the cases, the maximum instantaneous rate of intensity modulation increases with increasing frequency or increasing amplitude of vibration. Therefore, the camera's frame rate has to be adjusted to accommodate the fastest varying displacements of the test sample. The effect of aliasing is demonstrated by experimental validation in the next chapter.

The next section highlights one of the most attractive features of this technique that allows for dynamic measurement and big displacements.

3.6. Real-Time Tracking of Average Intensity A and Modulation B

Recollecting the intensity equation 2-6, it has three unknowns. The unknowns are average intensity A , modulation quantity B and the phase that relates to the displacement information. To find the phase, we need to determine A and B . By observing the theoretical intensity plots discussed so far, it seems that the values of A and B remain constant over time for a pixel. If that be the case, A and B can be obtained by finding the maximum and minimum intensity values of a pixel's intensity time series. The experimental data suggests that the values of A and B vary with the object motion and are never constant if we follow in time. Some pixels might contain either several speckles, one speckle or part of a speckle. In all the cases, when the surface of the test sample moves, the speckles associated with the microscopic surface roughness also move [37]. The speckles start shifting to the neighbouring pixels and the original values of A and B for that pixel will not remain the same.

For instance, Figure 3-12 shows a group of speckles that is centered at a pixel on the bottom left. The average intensity A at that pixel is well-defined while the modulation B in that pixel depends strongly on the number of speckles contained within the pixel. On the other hand, the two pixels on the top right and bottom right have their centers corresponding to the boundary or interface between speckles. The modulation B in those pixels would be close to zero.

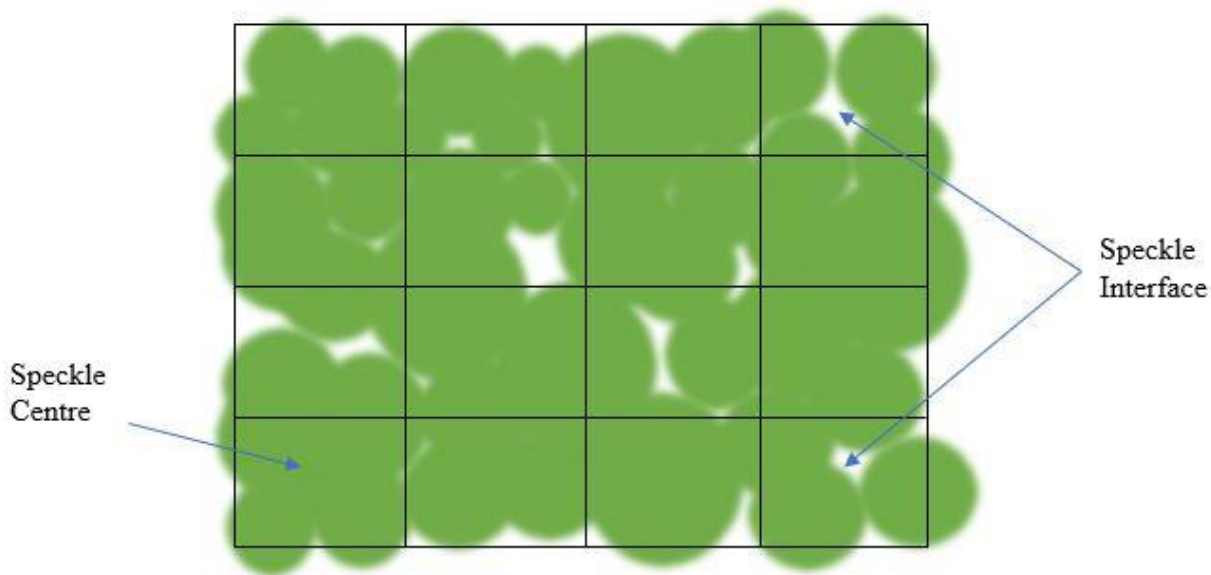


Figure 3-12: Random arrangement of speckles in a group of pixels. Some of the pixels have speckle boundaries at the centre and some of them have bright speckle centres

Figure 3-13 and Figure 3-14 show experimental plots of intensity of a pixel. The variation in the average intensity and modulation values is clear. This feature of the speckle motion that effects the modulation quantity restricts typical ESPI to smaller displacement ranges. When B reduces and becomes zero and then increase again, the new speckle entering the pixel lose correlation with the speckle occupying the pixel before. The decorrelation issue caused by a speckle shifting to another pixel can be avoided by measuring the displacements in smaller steps. One of the advantages of this novel interpolation technique discussed in the thesis is that the changes in A and B are tracked throughout the series of measured intensities. In other words, the proposed method does not rely on the assumption that the values of A and B remain constant over time, and therefore allows the measurement of large deformations using ESPI.

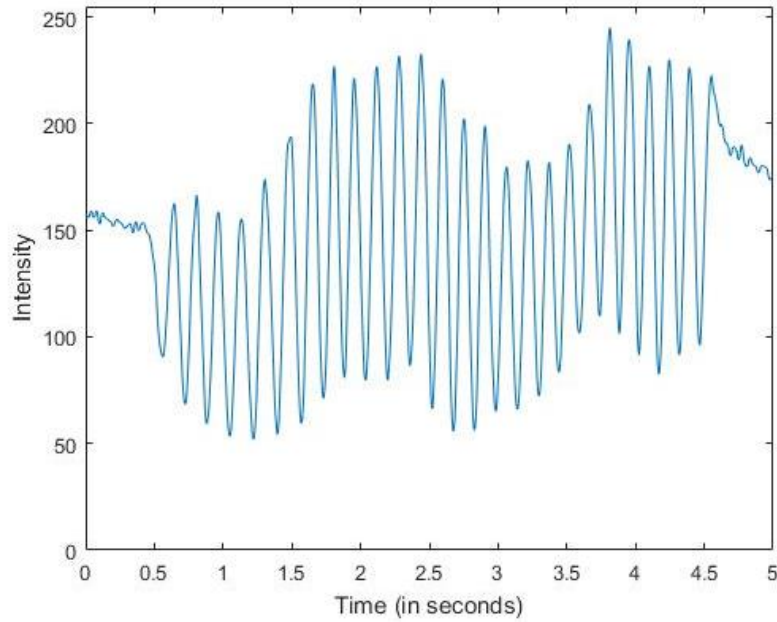


Figure 3-13: Intensity plot of a pixel when the sample is displaced in a linear fashion with a constant velocity. The range of displacement is 22 micrometers. The instantaneous phase frequency remains constant and the camera frame rate depends on the velocity of motion

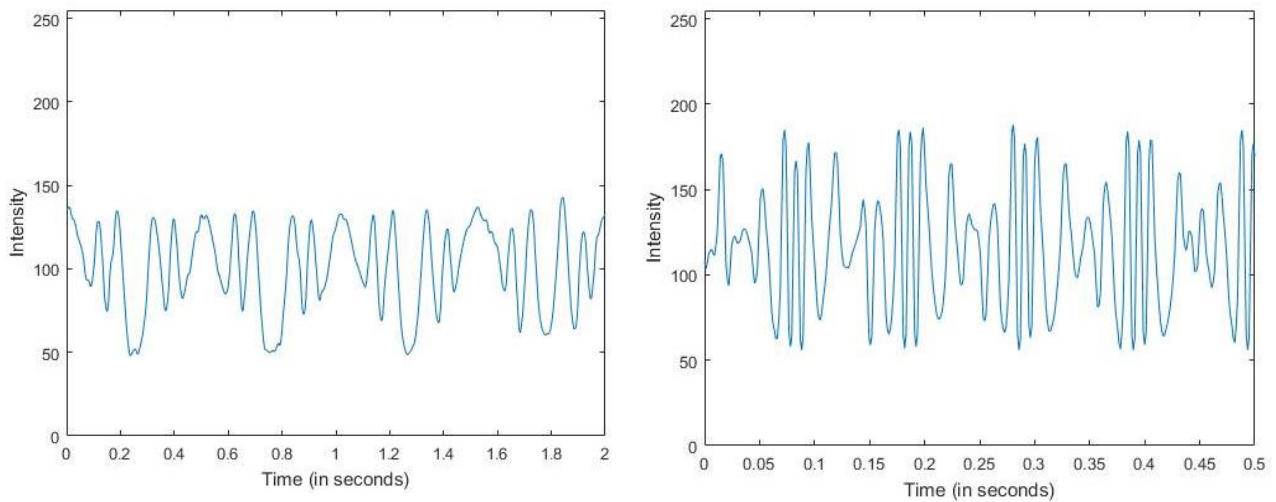


Figure 3-14: The intensity plot of a pixel when the sample is excited at a certain frequency. (Left) Vibration with a small amplitude and frequency 4Hz. Data is for 2 seconds (Right) Vibration with a higher amplitude and frequency of 10Hz. Data is for half a second

These figures exemplify two characteristics discussed in the sections 3.5 and 3.6. In the case where the test surface moves with constant velocity, the instantaneous modulation frequency remains constant and the camera frame rate can be set based on the velocity of motion. In the case of vibrating samples, the instantaneous modulation frequency is like that of an FM wave and therefore the camera frame rate has to be set according to the maximum modulation frequency. That frequency value is dependent both on the amplitude and frequency of vibration. In addition, Figure 3-14 (top and bottom) shows that mean intensity A and the modulation intensity B vary as the surface moves.

Experimental data and validation of the new interpolation method for dynamic ESPI are discussed in the next chapter. The applications and features of the proposed method are validated.

4. Measurements and Validation

A series of experiments was conducted to validate the proposed technique. Some were quantitative measurements to highlight the accuracy and precision of the method, while qualitative experiments were to focus on the applications of the method. Experiments were also conducted to demonstrate the effect of camera frame acquisition rate on the measured data and to show how low frame rate results in aliasing. Some post-processing techniques were developed to address artifacts so as to extend the use of the measurements.

4.1. Camera Frame Rate

The theoretical considerations discussed in Section 3.5 indicate that at least four measurements are required per phase change cycle (phase change = 2π) for each of the four phase sequences that are recorded. This required at least 16 measurements per phase change cycle to accommodate all the four phase sequences. The first tests were designed to investigate this criterion by exploring how frame rate affects interpolated intensity results. Figure 4-1 shows the test sample used in the setup. It comprises a long steel rod that is displaced linearly at the top using a single-axis Newport ESP 100 motion controller. ESPI measurements were made at the bottom of the rod. This arrangement was used so that sub-micron displacements could be observed when using a motion controller with multi-micron resolution. Seven cases were studied where the velocity of the motion was kept fixed while the frame rate was reduced from 200 fps to 25 fps. In this way, the onset of insufficient frame rate could be observed.

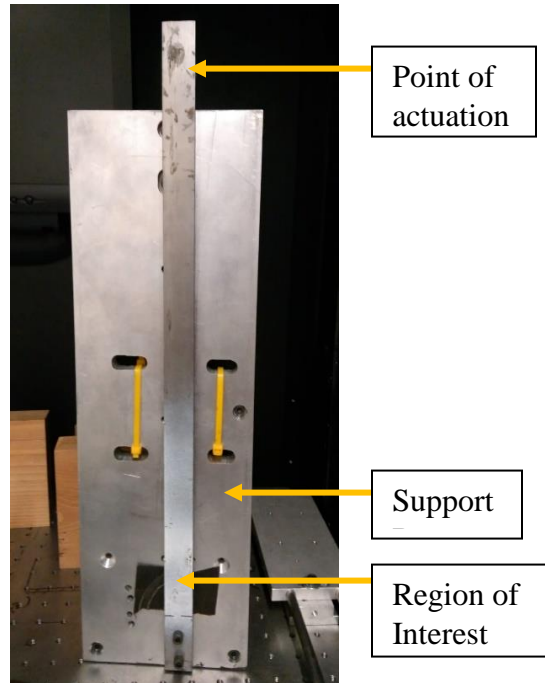


Figure 4-1: Test sample for demonstrating the effect of frame rate

The experimental parameters for the set in this section are given in the Table 4-1.

Table 4-1: Experimental parameters for showing the effect of frame rate

Velocity of test surface	5.7 microns/sec
Minimum required frame rate	~ 97 fps (Using equation 3-13)
Frame rates used in the tests	200, 120, 100, 80, 60, 40 and 25

Case 1 in Figure 4-2 shows light intensity measurements at an example pixel made at 8.2 frames/cycle/sequence, which is approximately double the theoretical minimum frame rate. The interpolation then gives realistic results with no concern for aliasing. As expected for a linear motion, the phase change per frame is approximately constant. The estimated phase change between piezo steps is stable around 90° .

Case 2 in Figure 4-3 shows a similar measurement made at 5 frames/cycle/sequence. This is somewhat greater than the minimum theoretical rate of 4 frames/cycle/sequence. It can be seen that although the results are somewhat noisier than those of Case 1, they still are realistic and not subject to aliasing.

Case 3 in Figure 4-4 shows a further measurement made at 4.1 frames/cycle/sequence. This barely exceeds the minimum theoretical frame rate. Incipient aliasing is apparent in the interpolated light intensity curves, with consequent increases in noise in the phase change per frame and phase step results. While marginally acceptable, this minimal frame rate condition is likely an unconservative choice for general-purpose use.

Cases 4-7 in Figure 4-5 to Figure 4-8 illustrate the increasingly damaging effects of aliasing as the frame rate is reduced below the 4 frames/cycle/sequence theoretical threshold. Noise in the phase change per frame and phase step results continue to increase until eventually the computations entirely fail.

CASE 1: Frame Rate = 200 fps

- $0.19 \text{ rad/frame} = 33 \text{ frames/cycle (including 4 sequences)} = 8.2 \text{ frames/cycle/sequence}$

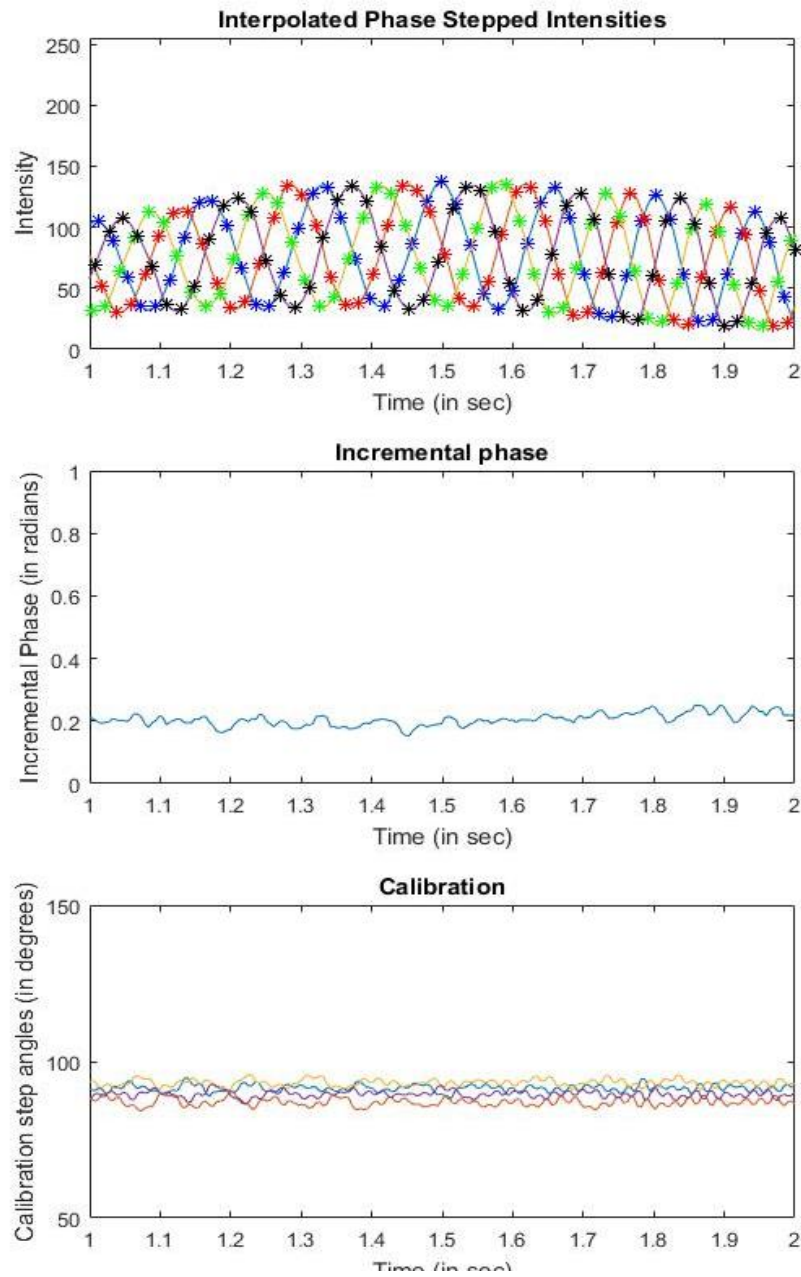


Figure 4-2: (Top) Zoomed into 1 sec of interpolated intensities for all the four phase-stepped sequences, (Centre) Incremental phase change from one frame to the next with respect to time and, (Bottom) Calibration steps. This is the case when frame rate is 200fps and we have 8.2 frames/cycle/frame

CASE 2: Frame Rate = 120 fps

- $0.32 \text{ rad/frame} = 20 \text{ frames/cycle (including 4 sequences)} = 5 \text{ frames/cycle/sequence}$

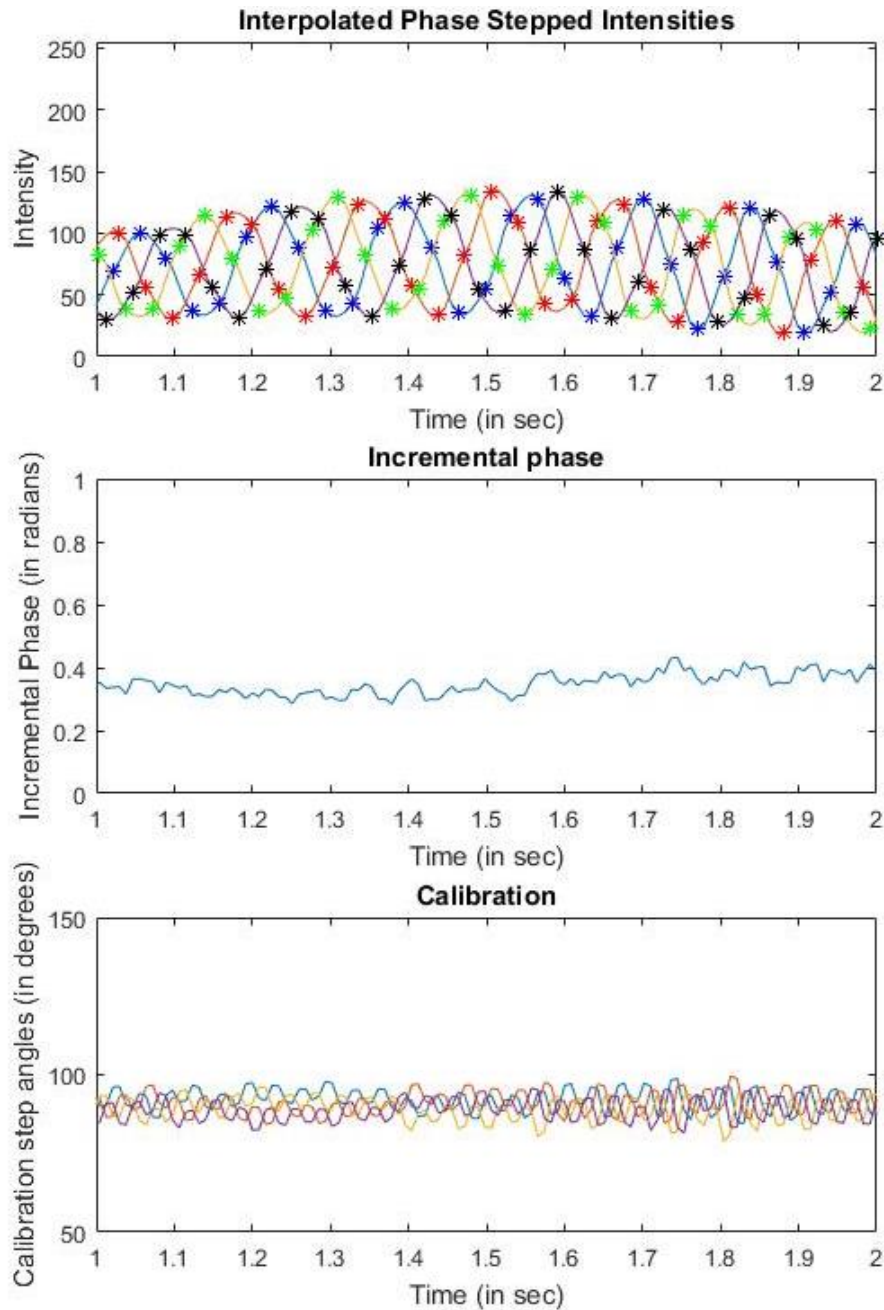


Figure 4-3: (Top) Zoomed into 1 sec of interpolated intensities for all the four phase-stepped sequences, (Centre) Incremental phase change from one frame to the next with respect to time and, (Bottom) Calibration steps. This is the case when frame rate is 120fps and we have 5 frames/cycle/frame

CASE 3: Frame Rate = 100 fps

- $0.38 \text{ rad/frame} = 16.5 \text{ frames/cycle (including 4 sequences)} = 4 \text{ frames/cycle/sequence}$

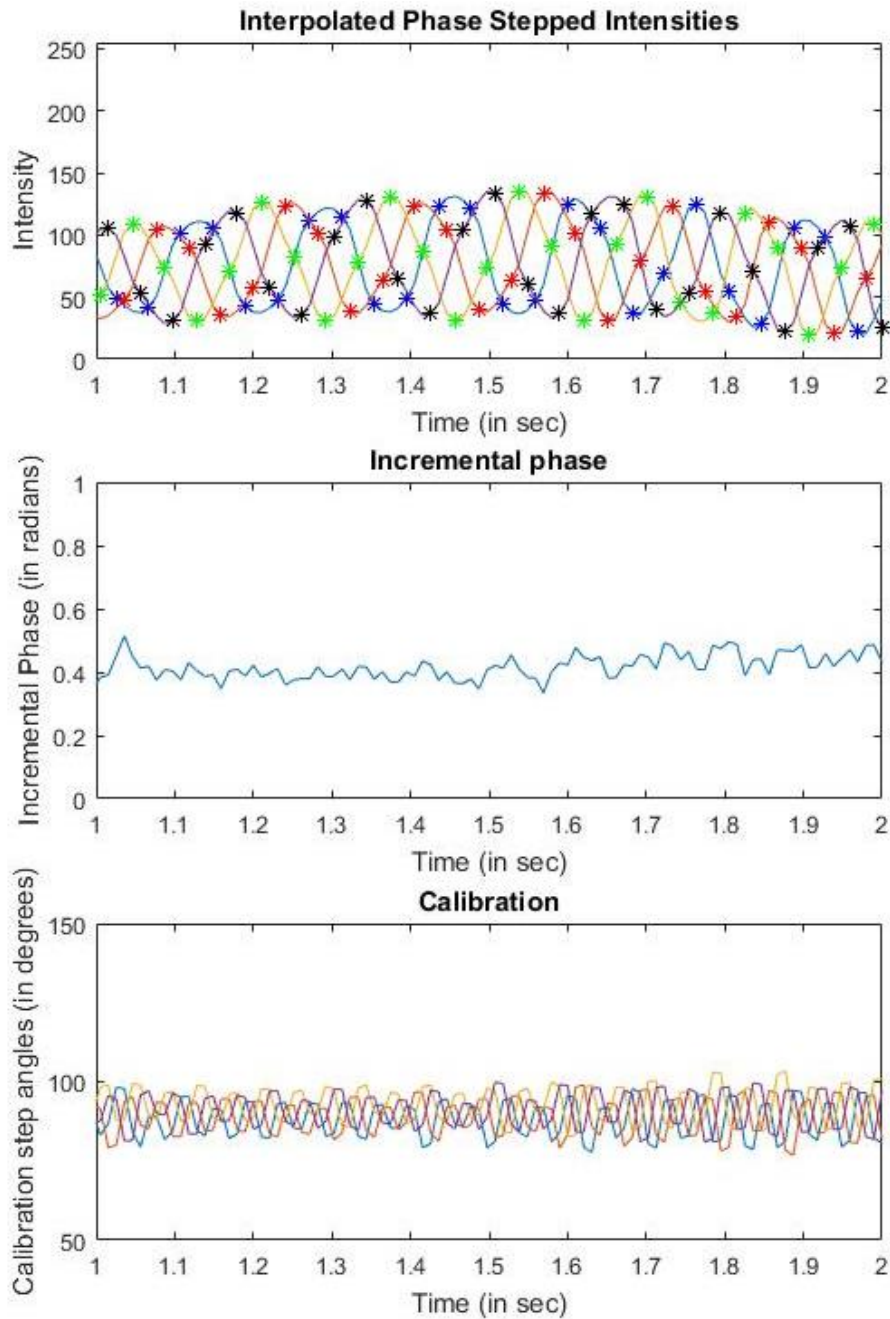


Figure 4-4: (Top) Zoomed into 1 sec of interpolated intensities for all the four phase-stepped sequences, (Centre) Incremental phase change from one frame to the next with respect to time and, (Bottom) Calibration steps. This is the case when frame rate is 100fps and we have 4 frames/cycle/frame

CASE 4: Frame Rate = 80 fps

- $0.47 \text{ rad/frame} = 13.2 \text{ frames/cycle}$ (including 4 sequences) = $3.3 \text{ frames/cycle/sequence}$

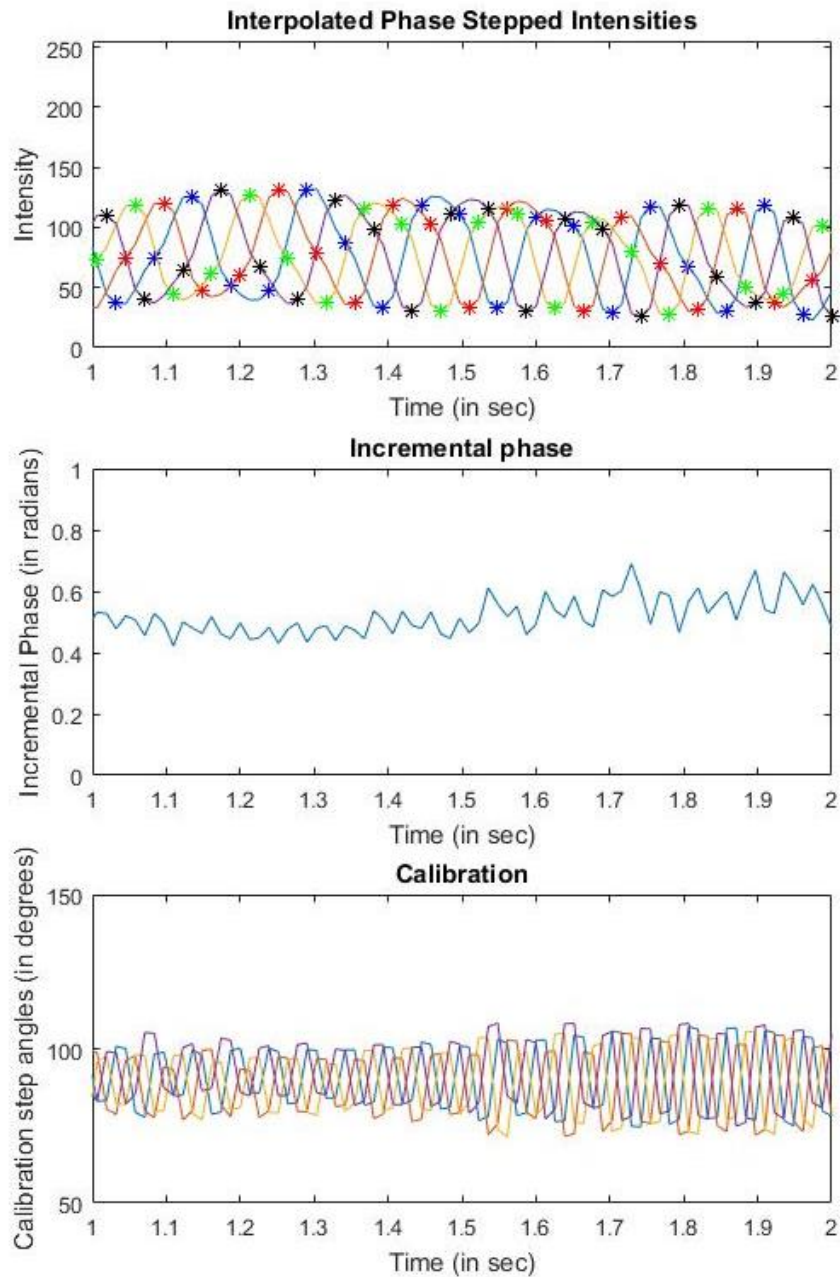


Figure 4-5: (Top) Zoomed into 1 sec of interpolated intensities for all the four phase-stepped sequences, (Centre) Incremental phase change from one frame to the next with respect to time and, (Bottom) Calibration steps. This is the case when frame rate is 80fps and we have 3.3 frames/cycle/frame. This one is just beginning to have aliasing. Anything below this frame rate will not be useful

CASE 5: Frame Rate = 60 fps

- $0.63 \text{ rad/frame} = 10 \text{ frames/cycle (including 4 sequences)} = 2.5 \text{ frames/cycle/sequence}$

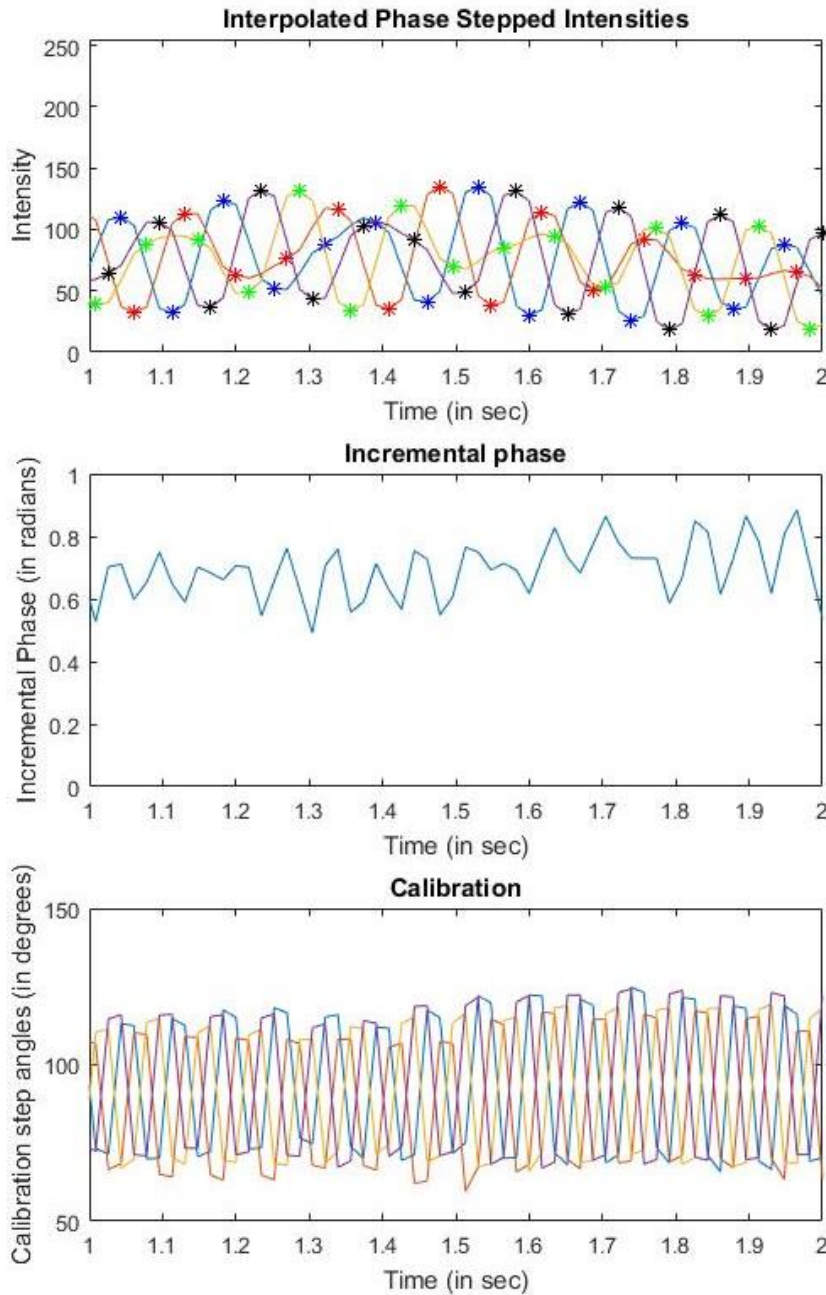


Figure 4-6: (Top) Zoomed into 1 sec of interpolated intensities for all the four phase-stepped sequences, (Centre) Incremental phase change from one frame to the next with respect to time and, (Bottom) Calibration steps. This is the case when frame rate is 60fps and we have 2.5 frames/cycle/frame. Aliasing is evident in this case

CASE 6: Frame Rate = 40 fps

- $0.95 \text{ rad/frame} = 6.6 \text{ frames/cycle (including 4 sequences)} = 1.6 \text{ frames/cycle/sequence}$

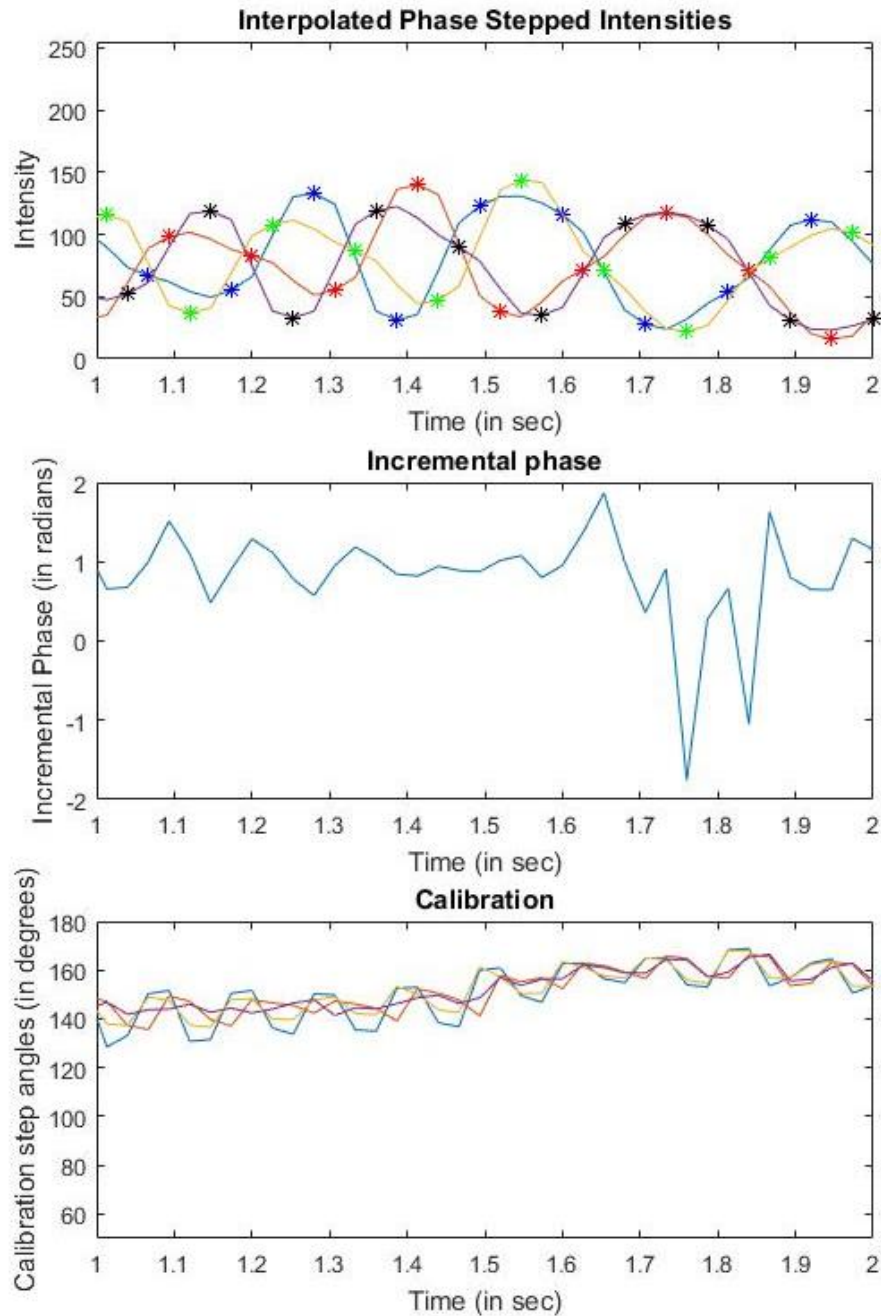


Figure 4-7: (Top) Zoomed into 1 sec of interpolated intensities for all the four phase-stepped sequences, (Centre) Incremental phase change from one frame to the next with respect to time and, (Bottom) Calibration steps. This is the case when frame rate is 40fps and we have 1.6 frames/cycle/frame. Aliasing is extremely evident in this case

CASE 7: Frame Rate = 25 fps

- $1.52 \text{ rad/frame} = 4.2 \text{ frames/cycle (including 4 sequences)} = 1.05 \text{ frames/cycle/sequence}$

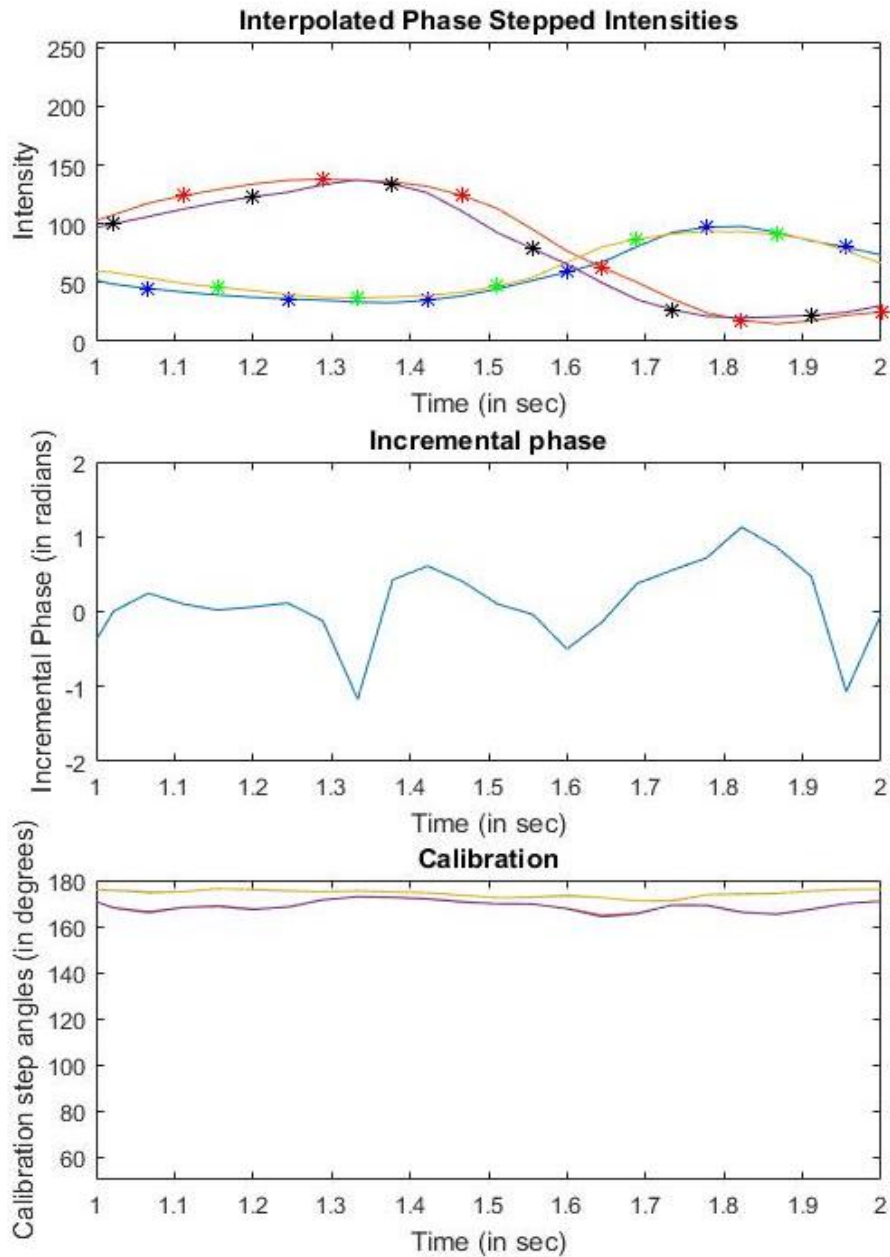


Figure 4-8: (Top) Zoomed into 1 sec of interpolated intensities for all the four phase-stepped sequences, (Centre) Incremental phase change from one frame to the next with respect to time and, (Bottom) Calibration steps. This is the case when frame rate is 25 fps and we have 1 frame/cycle/frame. This is to show the worst case when all the data is lost because only 1 frame is available every cycle.

4.2. Linear Deformation

The test setup shown in the Figure 4-9 was used to demonstrate the capability to make measurements of a continuously moving sample. The sample was mounted on a support that moves on a fixed rail. The support was actuated using a Newport ESP100 single-axis motion controller. Table 4-2 summarizes the test parameters.

Table 4-2: Experimental parameters for the experiment to measure linear fixed velocity displacement measurement

<i>Frame Rate</i>	300 fps
<i>Exposure</i>	400 μ s
<i>F#</i>	11
<i>Velocity of motion</i>	10 microns/sec
<i>Displacement</i>	30 microns
<i>Minimum required frame rate</i>	170 fps

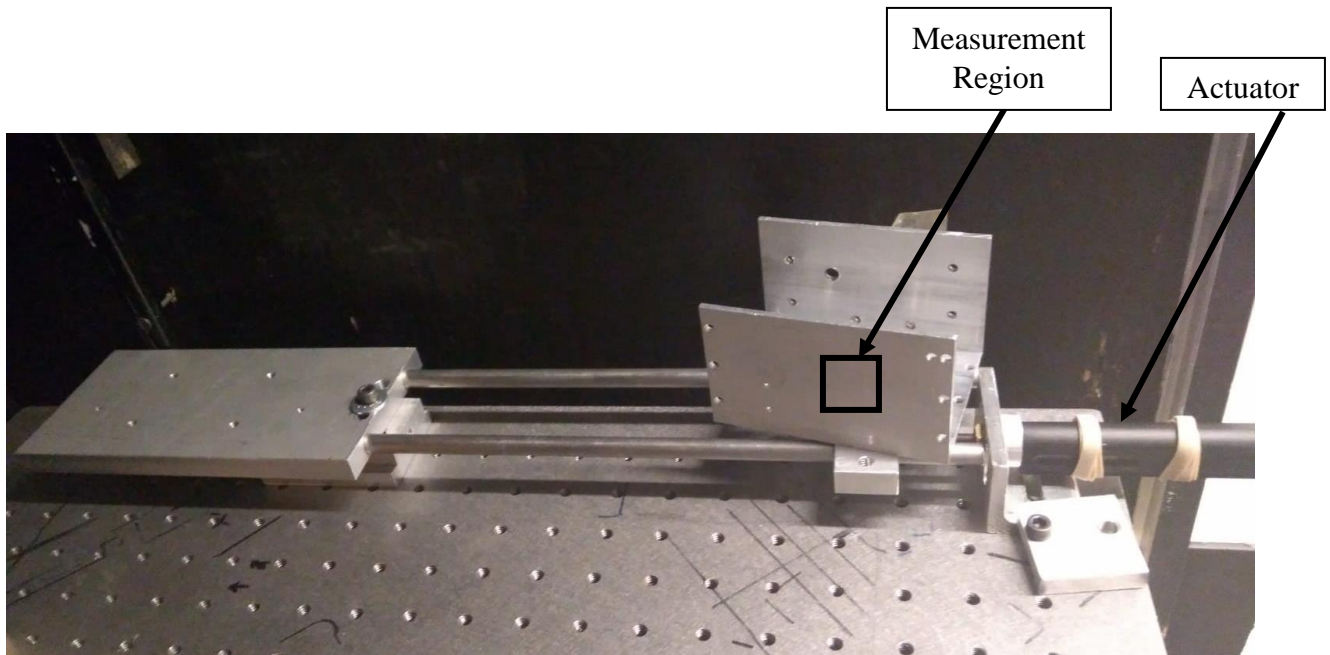
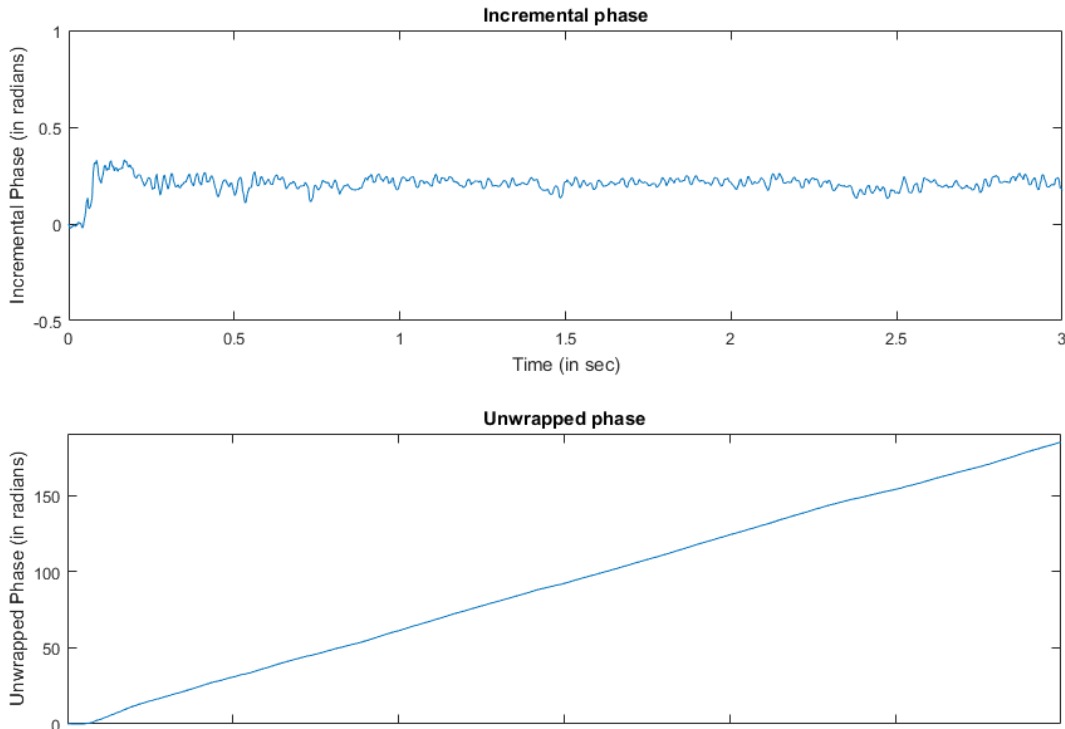


Figure 4-9: Test sample for linear fixed rate motion measurement

Figure 4-10 shows the incremental and summed-up phase values in the result. The 300fps frame rate was sufficient to provide 8-9 points/cycle/sequence. Figure 4-11 (Left) shows a zoomed-in view of the interpolated intensity series. The spacings between all the four phase sequences are consistent, indicating good stability of the calibrated steps. The incremental phase is constant because this is a fixed velocity motion. Adding the incremental phase values, total phase change is obtained with respect to time. Figure 4-11 (Right) shows that the measured displacement matches with the actual displacement. The displacement is obtained directly from the phase measurements using the geometrically determined sensitivity of the setup. The slope of the measured displacement also shows consistent agreement of the measurement technique. The accuracy and precision of the method is discussed in the next section.



**Figure 4-10: (Top): Incremental phase change with respect to time.
(Bottom): Measured phase plotted by adding the incremental phase values.**

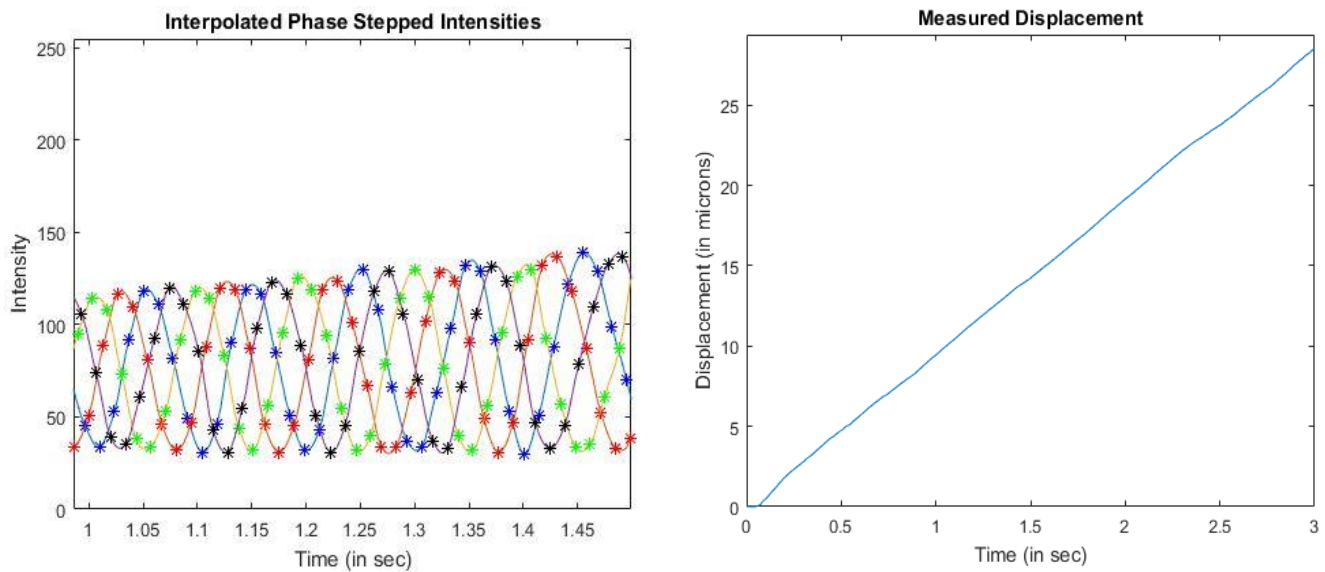


Figure 4-11 (Left): Zoomed in view of the sequences showing 8-9 points/cycle/sequence (Right): Measured displacement of the sample directly calculated from the measured phase values

4.3. Accuracy and Precision

A series of linear displacement experiments was conducted to quantify the accuracy of the proposed technique. The test sample used was the same as shown in Figure 4-9. The sample was fixed on a linear rail that was displaced using a Newport ESP100 single-axis motion controller. The displacements in the measurement region ranged from 20 microns to 100 microns. For each displacement set, 5 measurements were recorded. The test parameters are listed in Table 4-3 below.

Table 4-3: Experimental parameters for the set of experiments to validate the accuracy of the proposed technique

<i>Frame Rate</i>	600 fps
<i>Exposure</i>	800 μ s
<i>Image dimension</i>	100 x 100
<i>F#</i>	8
<i>Average speckle size (on screen)</i>	23 microns
<i>Pixel size (on screen)</i>	22 microns
<i>Velocity of motion</i>	10 microns/sec

Figure 4-12 shows a typical plot comparing the measured displacement (as determined from measured phase change) and the applied displacement (as determined from the elapsed time at known displacement speed). Table 4-4 summarizes the measured displacement results from Figure 4-12 and the other similar measurements in the series.

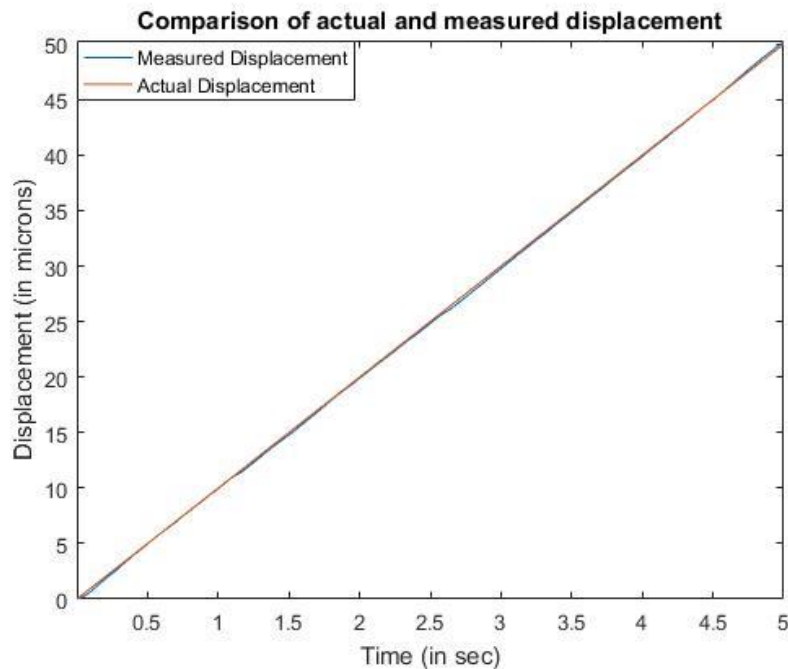


Figure 4-12: Comparison between the measured and actual linear displacement by plotting the displacements vs time

Table 4-4: Accuracy and precision using total of 20 measurements divided into 4 cases of displacements

Case Number	Actual Displacement (in microns)	Measured Displacement (in microns)	Error (%)
1	20	20.08 +/- 0.016	0.4%
2	30	30.21 +/- 0.022	0.7%
3	50	50.22 +/- 0.002	0.4%
4	100	98.50 +/- 0.015	1.5%

4.4. Vibration Measurement

CASE 1: Effect of Increasing Amplitude with Sinusoidal Excitation Wave

This set of experiments is to demonstrate a further application of the method to the measurement of vibrating samples. The test sample was a steel block fixed by flexible supports so that it was able to rotate. The sample was subjected to external excitation force from a coiled electromagnetic actuator. Figure 4-13 shows the arrangement.

Table 4-5: Experimental parameters for testing vibrating samples (Increasing amplitude)

<i>Frame rate</i>	350 fps
<i>Frequency of excitation</i>	1 Hz
<i>Amplitude</i>	1.5 microns to 2.7 microns
<i>Minimum frame rate required</i>	160 fps for 1.2 microns and 290 fps for 2.7 microns
<i>Recording time</i>	2 seconds

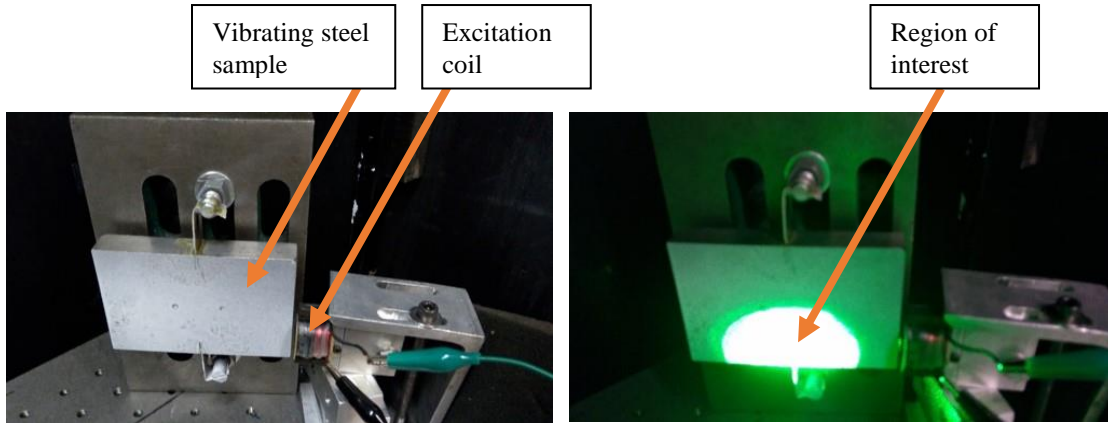


Figure 4-13: Vibration measurement sample excited using an electromagnetic coiled exciter

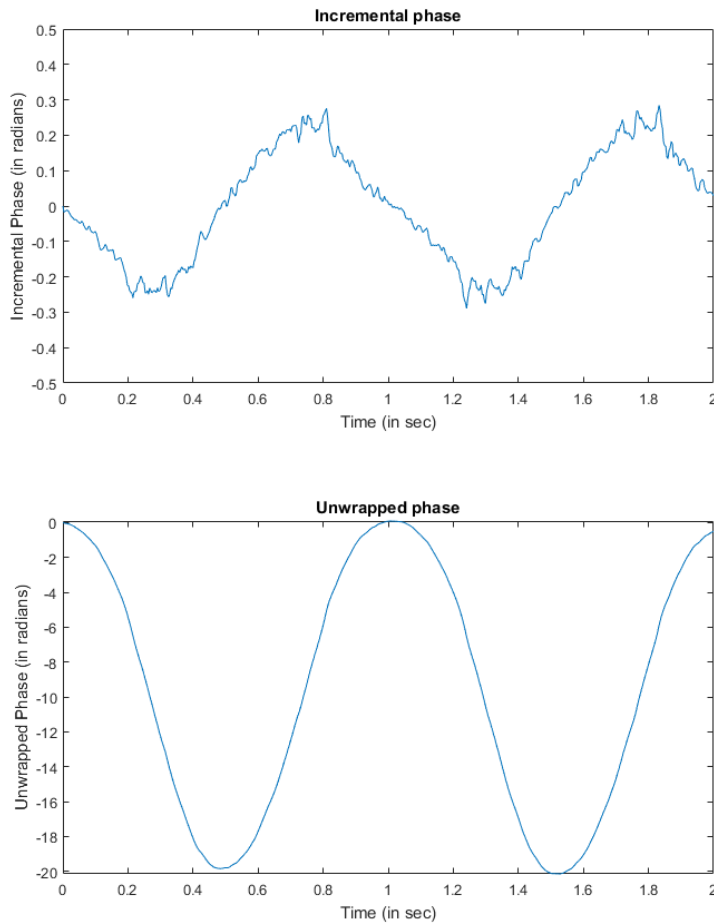


Figure 4-14: Study 1 with amplitude around 10 radians

(Top): incremental phase change with respect to time

(Bottom): Measured phase plotted by adding the incremental phase values

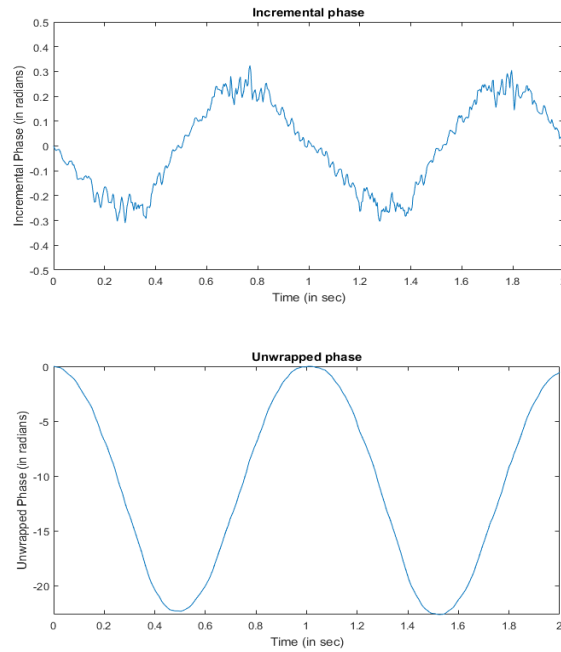


Figure 4-15: Study 2 with amplitude around 11.3 radians

(Top): incremental phase change with respect to time

(Bottom): Measured phase plotted by adding the incremental phase values

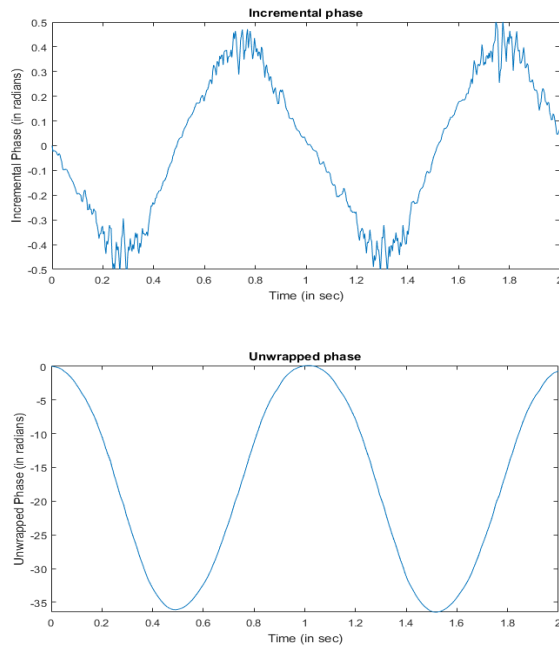


Figure 4-16: Study 3 with amplitude around 18.3 radians

(Top): incremental phase change with respect to time

(Bottom): Measured phase plotted by adding the incremental phase values

Figure 4-14 to Figure 4-16 show the effect of increasing the excitation amplitude. Unlike the previous linear fixed velocity deformations, the incremental phase change in this case continuously varies. The measurements show that irregularities in the incremental phase occurs at the times within the vibration cycle where the surface velocity and hence the incremental phase are the greatest. The size and extent of the noise increases with vibration amplitude. This observation is in keeping with the prior observation from Figure 4-2 to Figure 4-8 that good results are achieved when there are at least 4 frames/cycle/sequence. This corresponds to a maximum incremental phase of 0.39 rad/frame. Figure 4-14 to Figure 4-16 show that increasing noise occurs when this threshold is approached or is exceeded.

CASE 2: Effect of Increasing Frequency with the Input as a Triangular Wave

In this further set of experiments to measure vibrations, the input waveform was changed from a sinusoid to a triangular ramp wave. Measurements were made with frequency 2 and 4 Hz.

Table 4-6: Experimental parameters for testing vibrating samples (Increasing frequency)

<i>Frame rate</i>	600 fps
<i>Exposure</i>	300 μ s

The measured phase values qualitatively agree with the input to the test sample. Since the signal is a ramp wave, the slope and hence the velocity remain approximately constant when ramping up and when ramping down. The corresponding incremental phases are therefore constant in magnitudes. The slopes are not exactly constant due to inertial effects of the vibrating mass. Figure 4-17 and Figure 4-18 show the same.

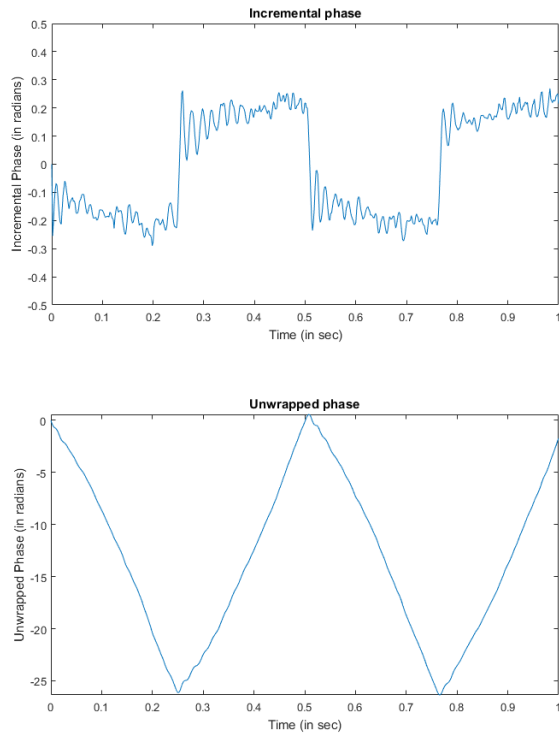


Figure 4-17: Case 1 with the input as a triangular wave of frequency 2 Hz

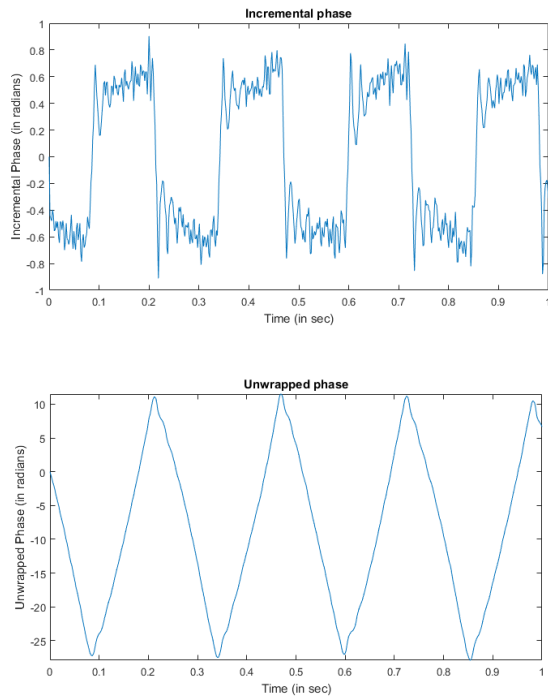


Figure 4-18: Case 2 with the input as a triangular wave of frequency 4 Hz

4.5. Test Sample Excitation using Custom Waveform

To demonstrate that the technique would work on any kind of excitation, a further series of measurements using a modulated sine wave was made. Figure 4-19 shows the input waveform to the electromagnetic actuator.

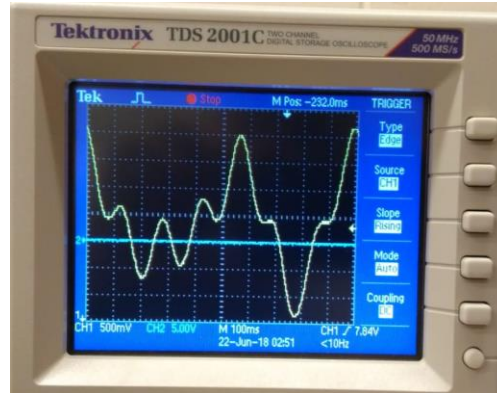


Figure 4-19: Input wave to the electromagnetic actuator

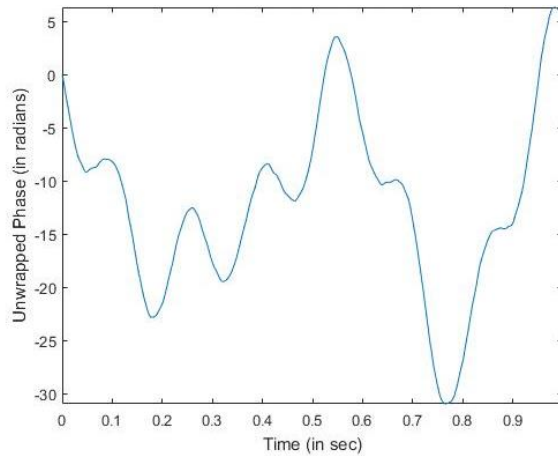


Figure 4-20: Measured phase plot when the sample was excited using a modulated sine wave as the input to the electromagnetic actuator

Figure 4-20 shows the measured phase plot. It looks very closely similar to the input waveform. This suggests that the method can successfully measure surface displacements with arbitrary motion.

4.6. Measurement of a Discontinuous Sample

This experiment is designed to demonstrate the applicability of the interpolation method on a discontinuous sample. This feature also highlights an important advantage of the method that it does not require phase unwrapping and therefore the final phase map calculation for discontinuous samples becomes possible without use of complex and computationally expensive phase unwrapping algorithms. Since every pixel measurement is independent of its neighbouring pixels, any discontinuity in the sample does not affect the measurement. Figure 4-21 shows the sample. A plastic eraser with a hole drilled at its centre was used as the specimen. It was glued to a rigid support on the left side and to steel extension on the right side. The steel extension was then actuated using a coiled electromagnetic exciter. The measured Region of Interest (ROI) spanned both the plastic eraser and the steel extension. The large ratio of the elastic modulus of the two components caused a sharp discontinuity in the observed deformation pattern along their attachment line. In addition, the external excitation force was deliberately applied at an offset from the overall central axis so as to create a significant and readily observable rotation.

Figure 4-22 shows the evolution of the wrapped phases with the increasing force. Figure 4-23 shows the evolution through unwrapped phase maps for the same experiment (Unwrapped phase is coloured because it is easier to visualize compared to monochrome). It should be noted that adding up the incremental phase values measured gives a direct measurement of the total phase values at any time instant; There is no difficulty or challenge in handling the discontinuous phase along the boundary line between materials. A concentration of fringes around the hole can also be seen that shows the region of stress concentration. Figure 4-24 shows conventionally unwrapped phase maps. The irregularities in the phase values obtained using the conventional method highlight the benefit of Interpolated-ESPI.

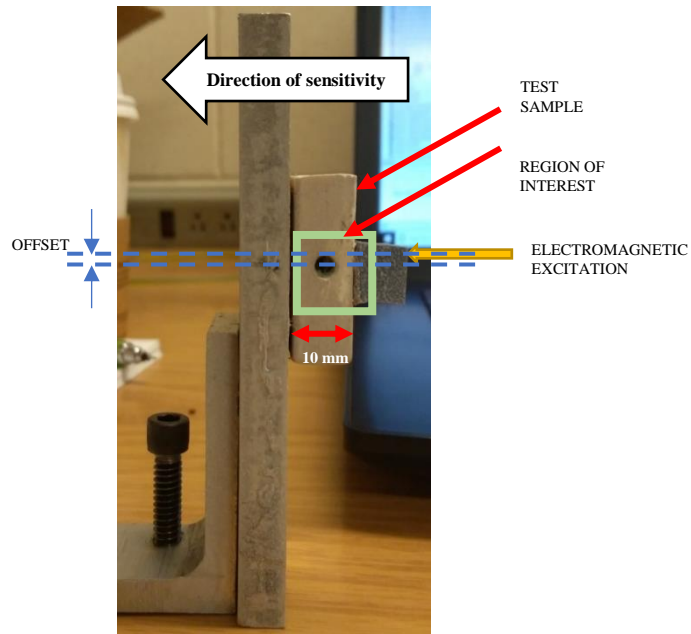
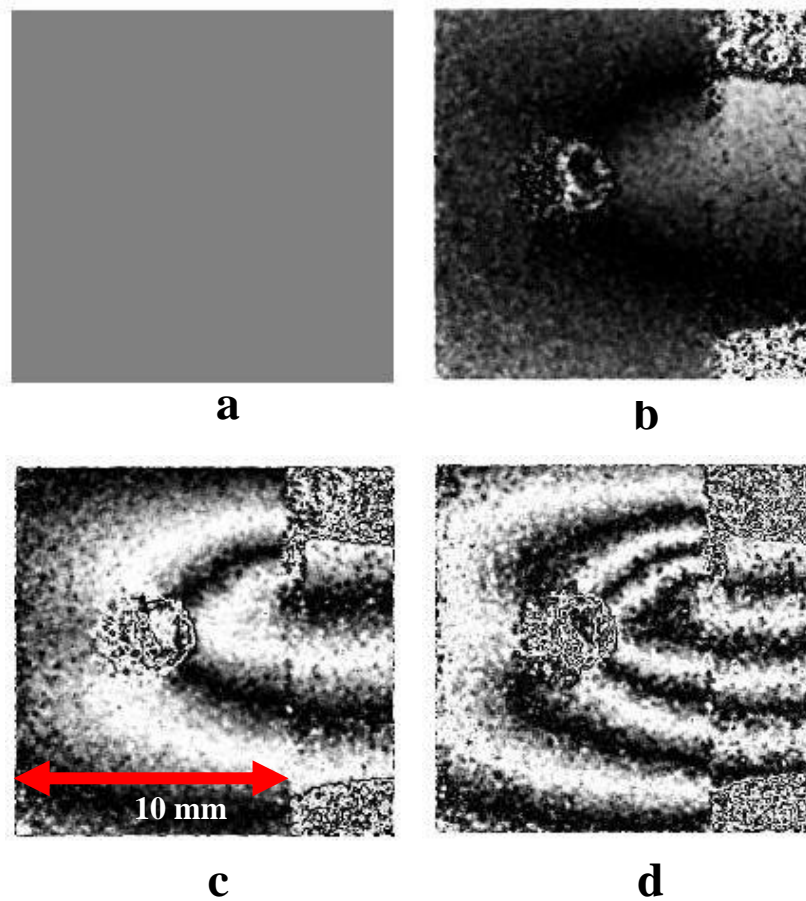


Figure 4-21: Test sample used to demonstrate measurement of discontinuous samples



**Figure 4-22: Wrapped phase maps. a) $t=0$ sec, beginning of the excitation, b) $t=0.16$ sec
c) $t=0.32$ sec and, d) $t=0.5$ sec**

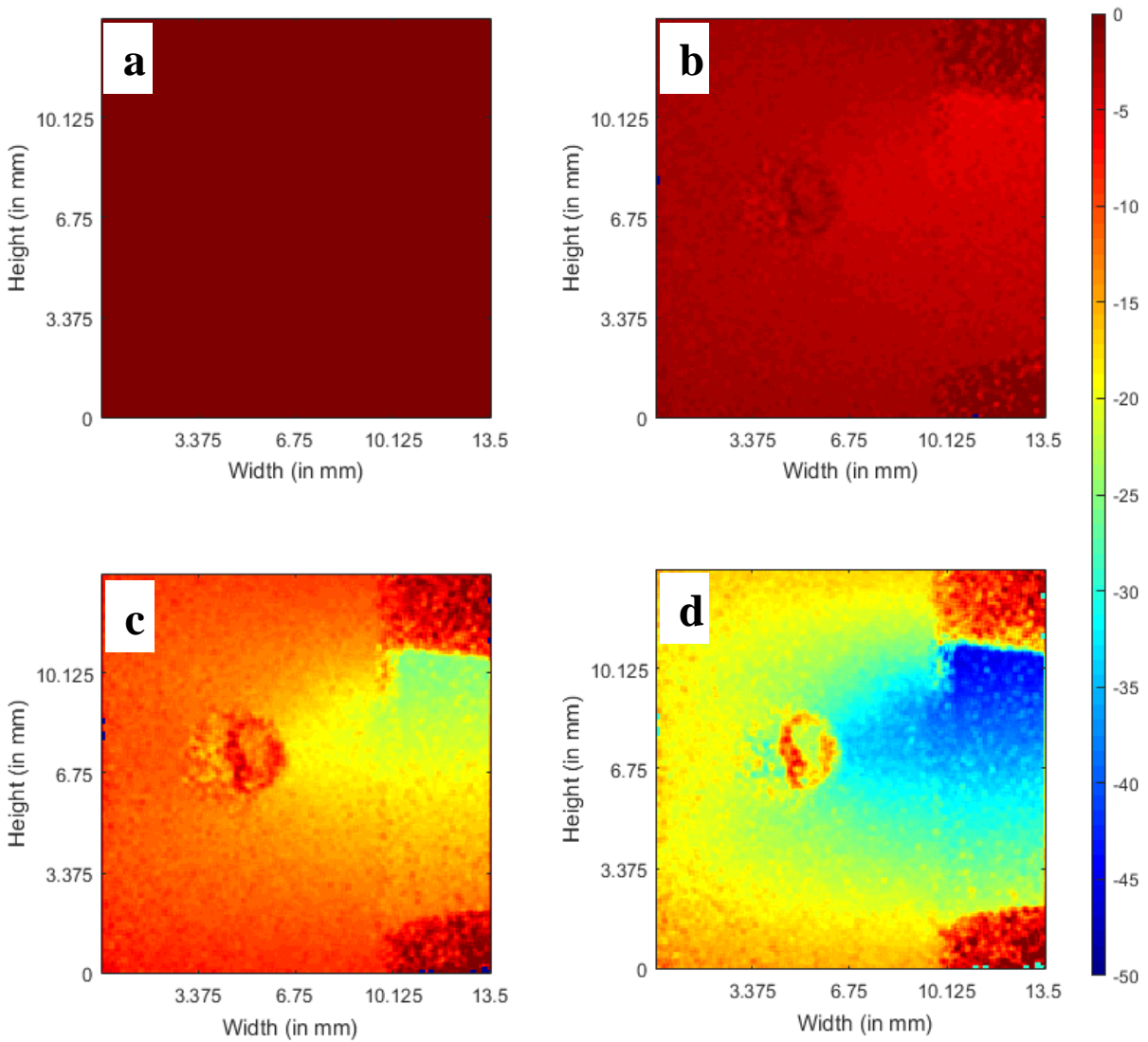


Figure 4-23: Added phase maps. a) $t=0$ sec, beginning of the excitation, b) $t=0.16$ sec c) $t=0.32$ sec and, d) $t=0.5$ sec. The scale on the right is in radians.

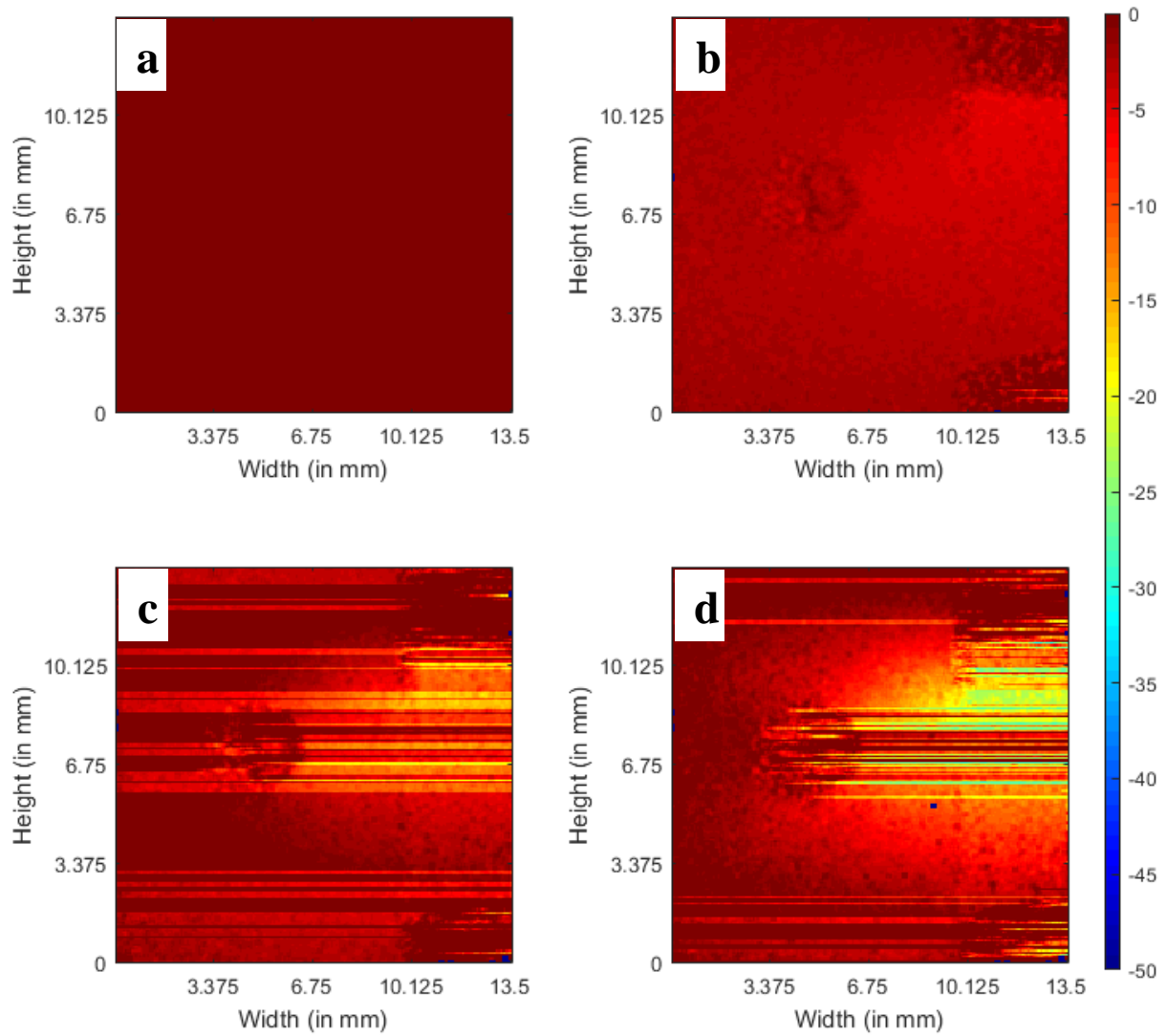


Figure 4-24: Conventional unwrapped phase maps.

a) $t=0$ sec, beginning of the excitation, b) $t=0.16$ sec

c) $t=0.32$ sec and, d) $t=0.5$ sec. The scale on the right is in radians.

4.7. Post Processing

4.7.1. Correction for low modulation

One of the most important characteristics of the Interpolated-ESPI technique is its ability to measure large deformations. Such measurements are not possible using the conventional technique because of the bulk motion of the speckles away from their original pixels and consequent phase decorrelation. As discussed in Section 3.6, the shift in speckle from one pixel to the next can be detected by tracking the pixel modulation. When a shift happens, the phase changes discontinuously by a random amount. If not corrected, that phase change carries forward throughout the measurement and introduces random noise into the measurement. Movement from one speckle to another at a given pixel can be detected by monitoring the local modulation B , and observing the modulation drops below a threshold value. All such pixels are flagged at every time instant. The correction procedure is based on the observation that at any instant, only a few pixels are subject to discontinuous phase changes due to the transition between adjacent speckles, the neighbouring pixels continue to function normally. Thus, the neighbouring pixels can be used to restore the phase continuity of the defective pixel. For each such pixel, a local neighborhood called kernel is selected, and that kernel is moved across the image. Every flagged pixel is replaced by the average of the adjacent unflagged pixels using a kernel of size a 3 x 3. This is the smallest kernel size and so produces the lowest spatial averaging in the results.

Figure 4-25 shows an example pixel that has passed through a region of low modulation corresponding to movement between speckles. The incremental phase map at $t=1\text{sec}$ shows the resulting discontinuous phase values. The corrected incremental phases shown in the last plot in the figure shows consistency in the values.

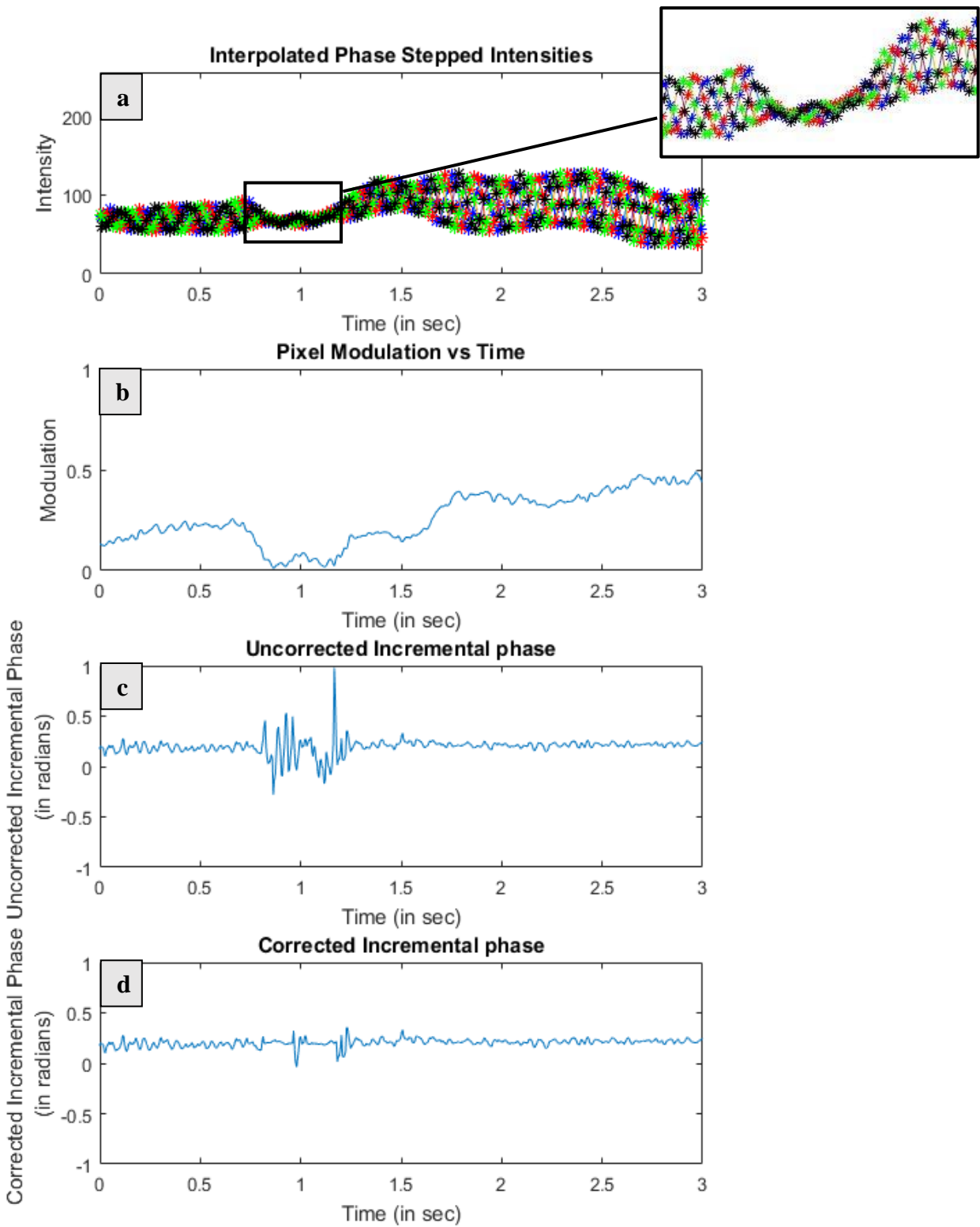


Figure 4-25: Example of post-processing showing correction of low modulation pixel.

- a). Shows the interpolated intensities. A zoomed view of one of the low modulation area is shown.**
- b). Modulation plot of the pixel. The low modulation points are detected and corrected for.**
- c). Shows the incremental phase map before correction.**
- d). Incremental phase plot after post processing.**

4.7.2. Correction for saturated pixels

The second post processing step is correcting for saturated pixels. The same method of correcting such pixels is used. Saturated pixels are the ones where the intensity of the pixels reach the maximum detectable value. For instance, for 8-bit pixel measurements, the maximum intensity value is 255. So, if a pixel receives a greater light intensity, the reported value remains at 255. Therefore, there is a loss of information in such saturated pixels. One way to avoid having many saturated pixels is to reduce the exposure time. However, this adjustment cannot be taken too far else the average light intensity will become low and discretization noise will become significant. Here, saturated pixels were identified as those with reported intensity values above 252. Their phase values were then corrected using the same 3x3 kernel averaging procedure as used for speckle transition correction.

Figure 4-26 and Figure 4-27 show two examples where the pixels pass through regions of saturation. The second case is more extreme compared with the first in the sense of calculation of the incremental phase values. The plots in these figures also show the correction technique and how it rectifies the faulty readings. The computed values in the second case, as seen in the Figure 4-27, would be completely false if not corrected for saturation.

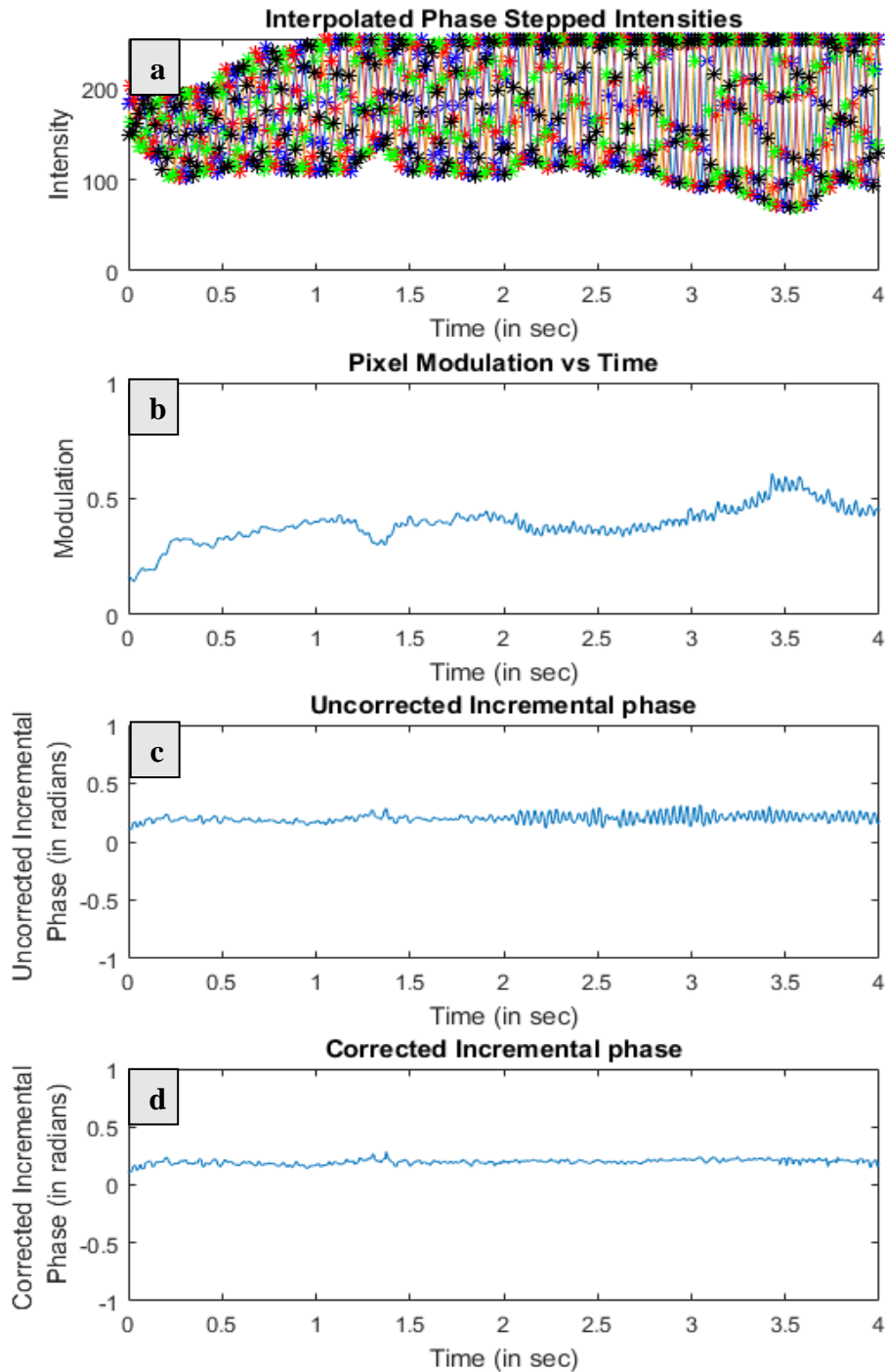


Figure 4-26: Example of post-processing where saturated pixel is corrected for.

- a). Shows the interpolated intensities. Saturated intensity region can be seen.**
- b). Shows the modulation map of the pixel.**
- c). Shows the incremental phase map before correction.**
- d). Shows the incremental phase plot after post processing.**

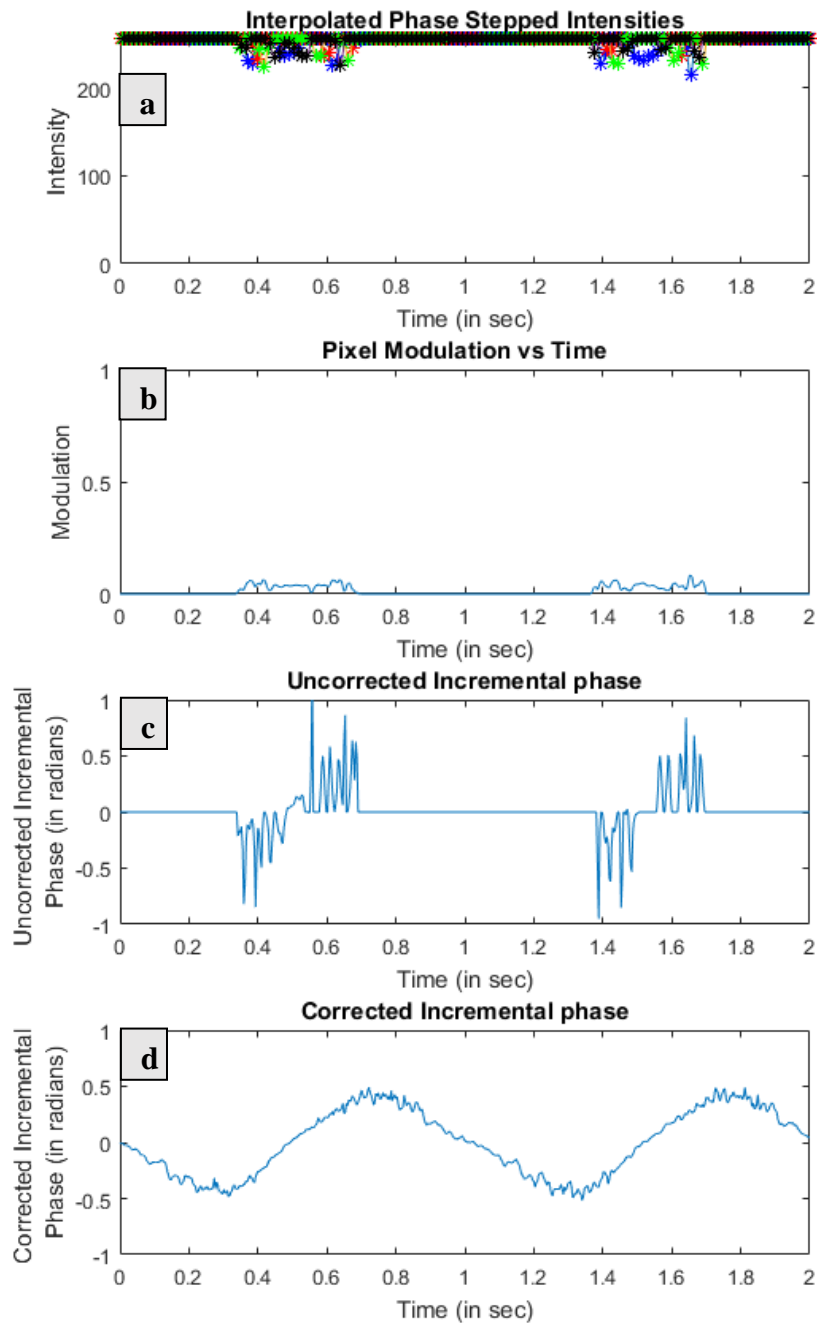


Figure 4-27: Case with extreme saturation of a pixel and its correction
a). Shows the interpolated intensities. Saturated intensity region can be seen.
b). Shows the modulation map of the pixel.
c). Shows the incremental phase map before correction.
d). Shows the incremental phase plot after post processing.

4.8. Large Displacement Measurements

The objective of this set of further experiments is to demonstrate that by combining Interpolated-ESPI with the post-processing correction techniques it is possible to measure large dynamic deformations reliably. Two cases are studied. Figure 4-28 shows the case where a 200-micron displacement is imposed. The first plot in the figure shows the four phase sequences recorded. It shows that the pixel passes through points of low modulation at least 4 to 5 times, causing serious decorrelation when not corrected. The third and the fourth plots respectively show the uncorrected and corrected incremental phase values.

Figure 4-29 shows how the added phase values appear before and after correction. The top figure shows zoomed-in view of the added phase values at regions of low modulation. The phase gets wrongly offset at those regions. The bottom figure shows the zoomed-in view of the same regions after correction. The offset is removed, and the added phase value is corrected.

Figure 4-30 shows the second case with a much higher displacement of 1000 microns or 1 mm. At this scale of displacement, there will be many points of low modulation or decorrelation. This is evident from the second plot in the figure which shows around 11 points approaching 0 visibility. This means that there will be 11 points when the error in the added phase values will be introduced and then propagated with time damaging the final phase result. The uncorrected and corrected incremental phase values are plotted in the third and the fourth plots, respectively. Finally, Figure 4-31 is plotted where the measured displacement value for such a big displacement is calculated and shown. 1000 microns displacement is measured with ~2.5% error.

CASE 1: 200 microns

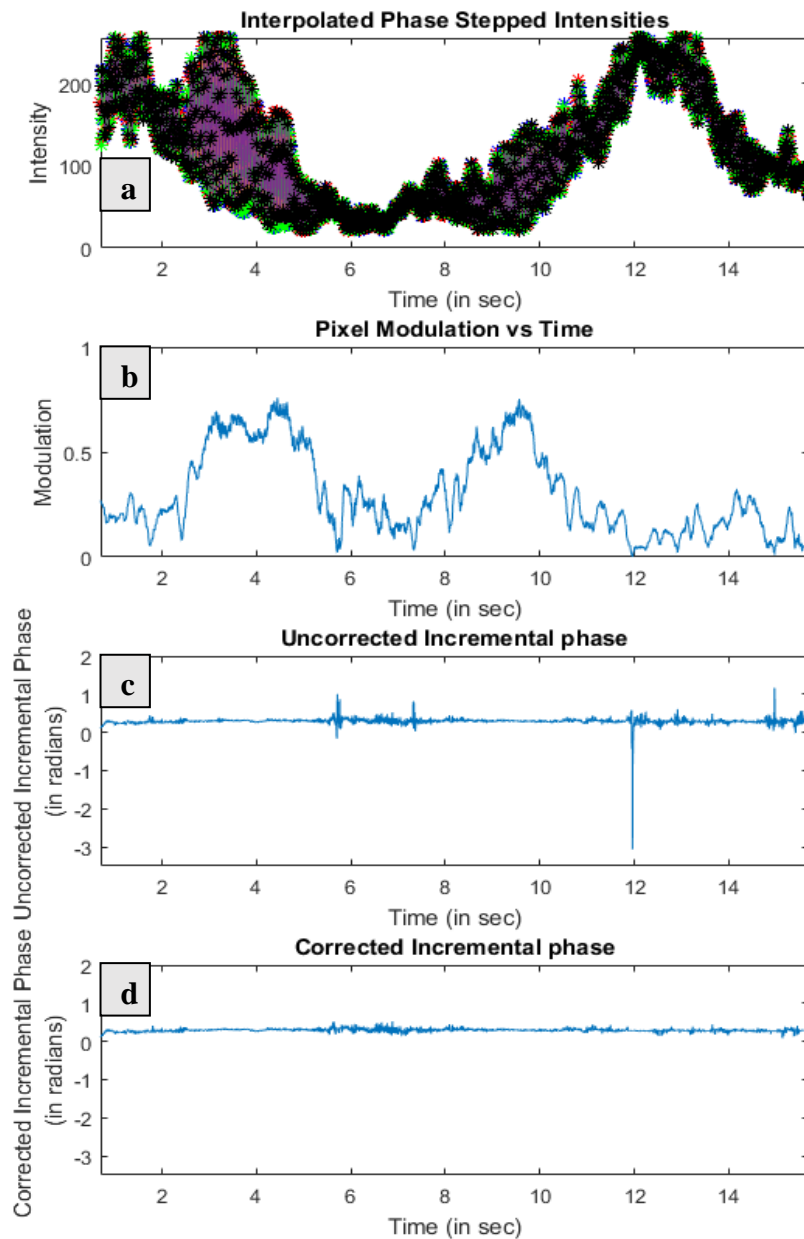


Figure 4-28: Application of the technique measuring large deformation. The deformation measure is around 1300 radians that corresponds to 200 microns.

- a). Shows the interpolated intensities. Low modulation regions can be seen.**
- b). This plot shows the modulation plot of the pixel.**
- c). This plot shows the incremental phase map before correction.**
- d). Incremental phase plot after post processing.**

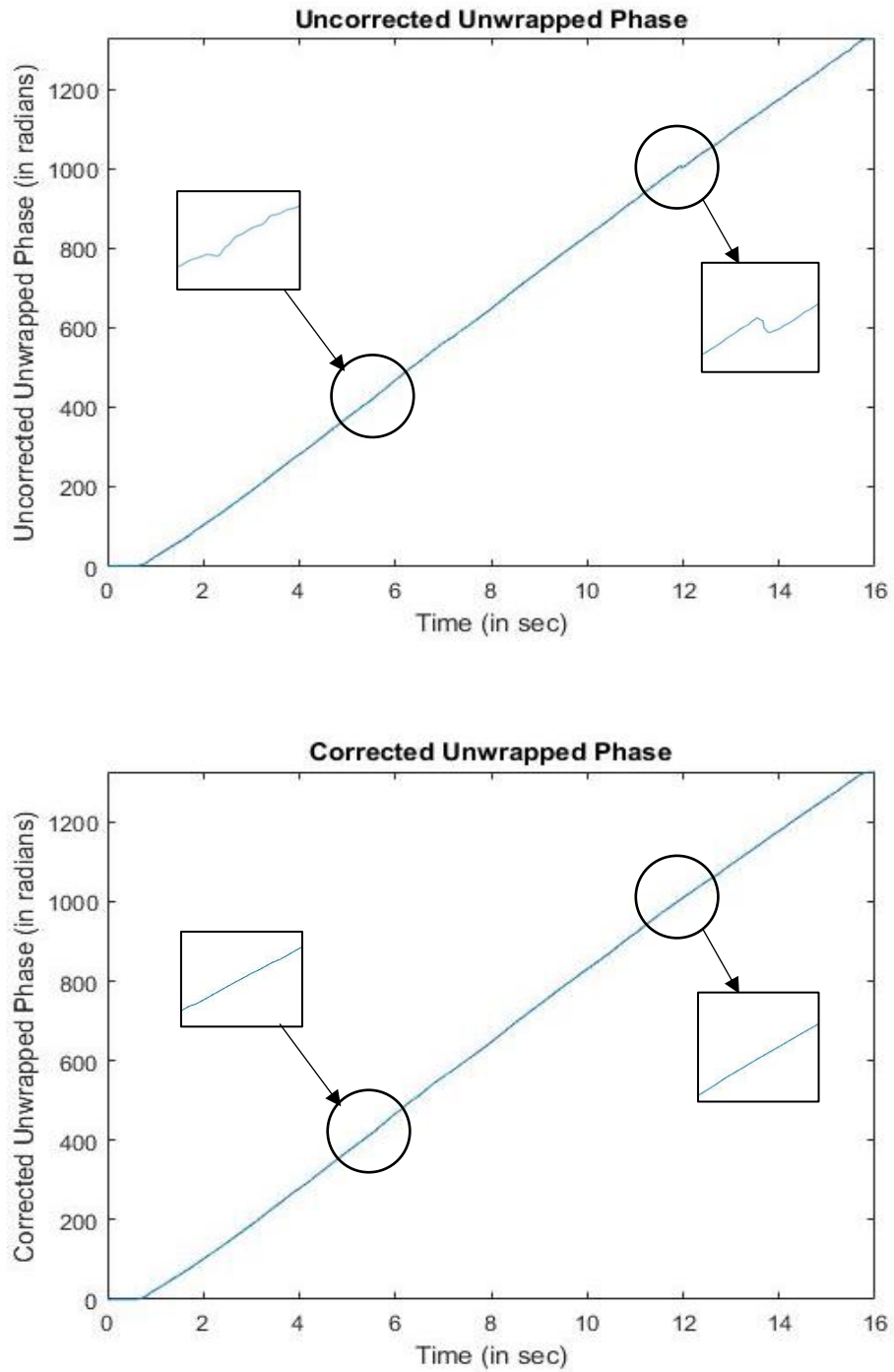


Figure 4-29: The unwrapped phase map for the same example of 200 microns displacement is shown.
(Top) The unwrapped phase before correction for correction of poor pixels.
(Bottom) The unwrapped phase after correction of pixels.

Case 2: 1000 microns

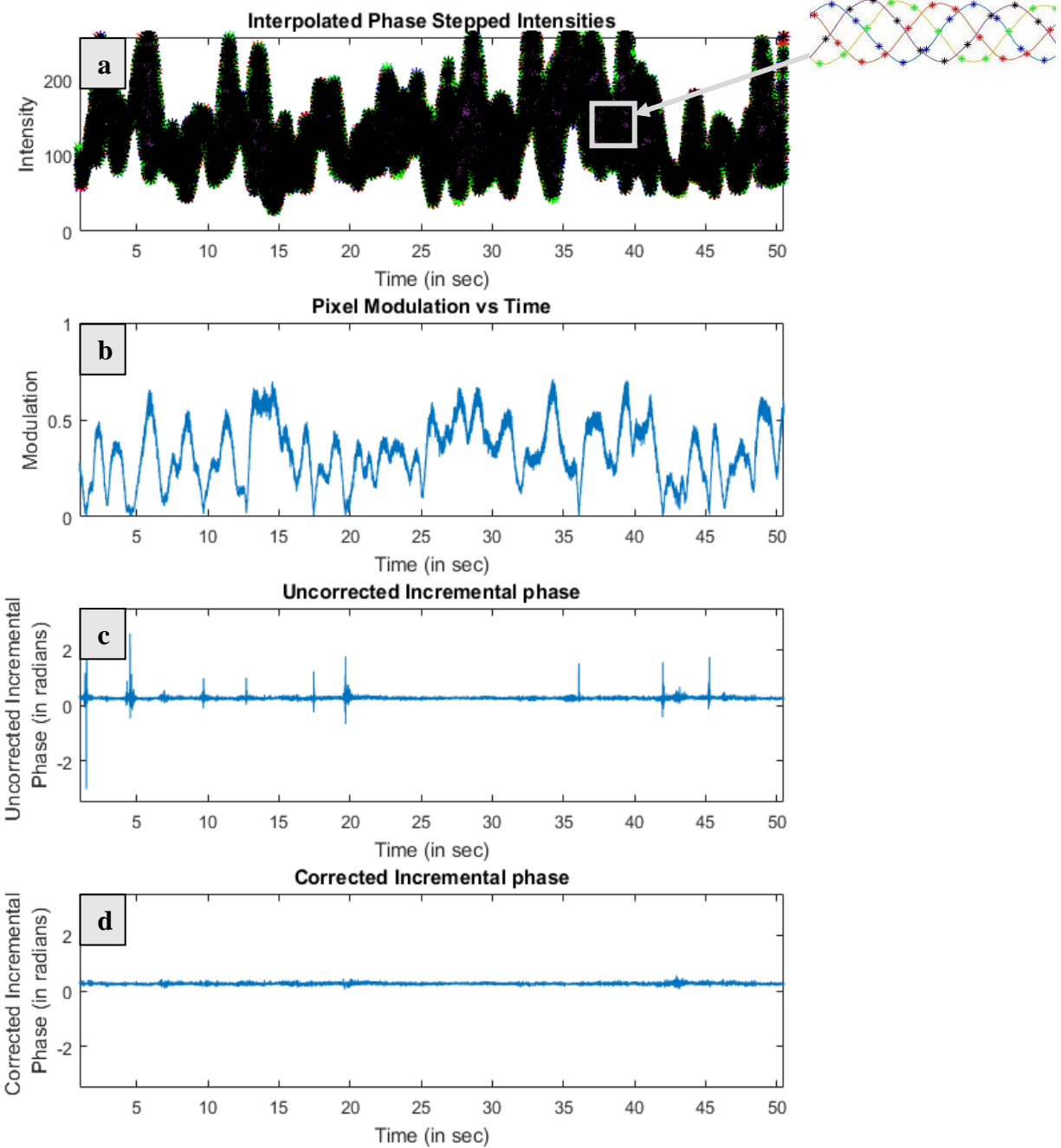


Figure 4-30: Second large displacement measurement example. The displacement here is 1000 microns.

- a). The interpolated intensities. Saturated intensity region can be seen.**
- b). The second plot shows the modulation plot of the pixel.**
- c). The third plot shows the incremental phase map before correction.**
- d). Incremental phase plot after post processing.**

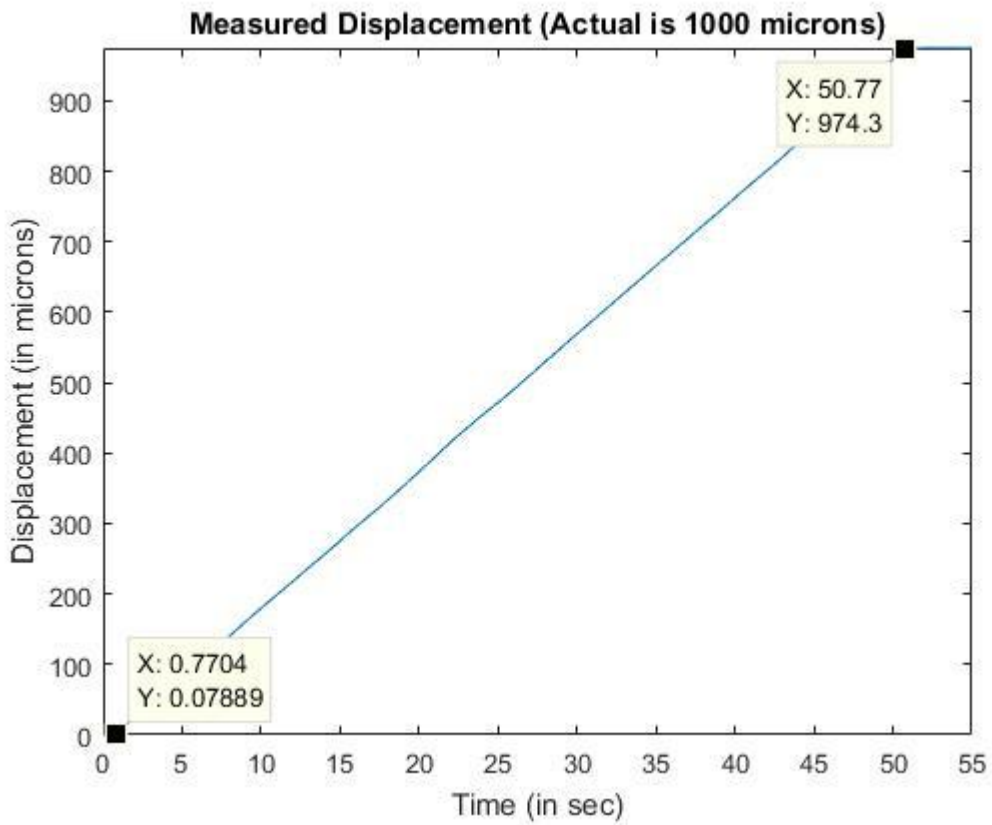


Figure 4-31: Displacement plot of the second example of 1000 microns. The measured value is 974 microns. This shows successful measurement of 1000 microns with around 2.5% error.

4.9. Errors

From all the example applications demonstrated, the average error ranges from 0.5%-3%.

The sources for the errors can be:

- Measurement error of the angles between the interfering beams. They were made small so as to moderate the sensitivity of the measurement. A 1° angle adjustment error between the beams would account for around 3% error in the measurement.
- The calibration angle is not exactly 90° which is the ideal case. The best achievable calibration for the fast moving piezo is between 85° - 95° . This would give small irregularities in the unwrapped data. The overall effect would be modest though.
- The actuator itself, although very precise, has some error of its own considering the micrometer scale of the measurement. The accuracy of the motorized actuator is $\pm 2 \mu\text{m}$.
- The mount and rail are not completely frictionless which would also account for some error especially due to jerking at the start and stop of the motion.

Considering all the above-mentioned reasons, the maximum error of 3% is understandable.

The steps that can be taken to control and reduce the error is to make sure that the angle measurement between the two interfering beams is more closely controlled. Also, the mounting for test sample can be made close to as ideal as possible, reducing friction.

4.10. Application: Wheat Seed Health Monitoring

A practical application area was explored to assess the potential of the Interpolated-ESPI technique. The investigation involved using biospeckles. A Biospeckle results from the interference of backscattered light from the biological samples [38]. It has several applications such as measuring flow in blood vessels [39], studying parasite activity in living tissues [40] and monitoring bull's eye rot [41]. All these measurements give a very good qualitative indication. Health monitoring of organic samples is done by observing the dynamic speckle activity in the sample, also known as Biospeckle Activity (BA). Here, a wheat seed was selected for study. In a germinating wheat seed sample, the diseased or infected regions show less BA compared to that in healthy seeds [42].

The Interpolated-ESPI system was used to make measurements on wheat seeds, some of them treated with a copper solution to inhibit the germination and growth. The results are shown in Figure 4-32. The two wrapped phase maps were compared, one of a healthy seed and the other of the one treated with copper. The phase maps are as shown in the Figure 4-33

The measured phase maps show substantial and consistent responses, indicating a good potential of the measurement method. As yet, the interpretation of the phase maps needs some further investigation because it is not yet apparent what physical phenomenon is driving the phase changes. It seems that surface lateral displacement is not the cause because the unwrapped phase change always occurred in the same direction independent of the seed orientation. Also, the magnitudes of deformation were quite high, reaching an apparent “displacement” of 30 microns in 2 seconds. This is much too fast to be physically realistic. Further experiments continue to determine the physical processes that drive the observed phase changes. Certainly, the Interpolated-ESPI technique is providing a good measurement tool for this investigation.

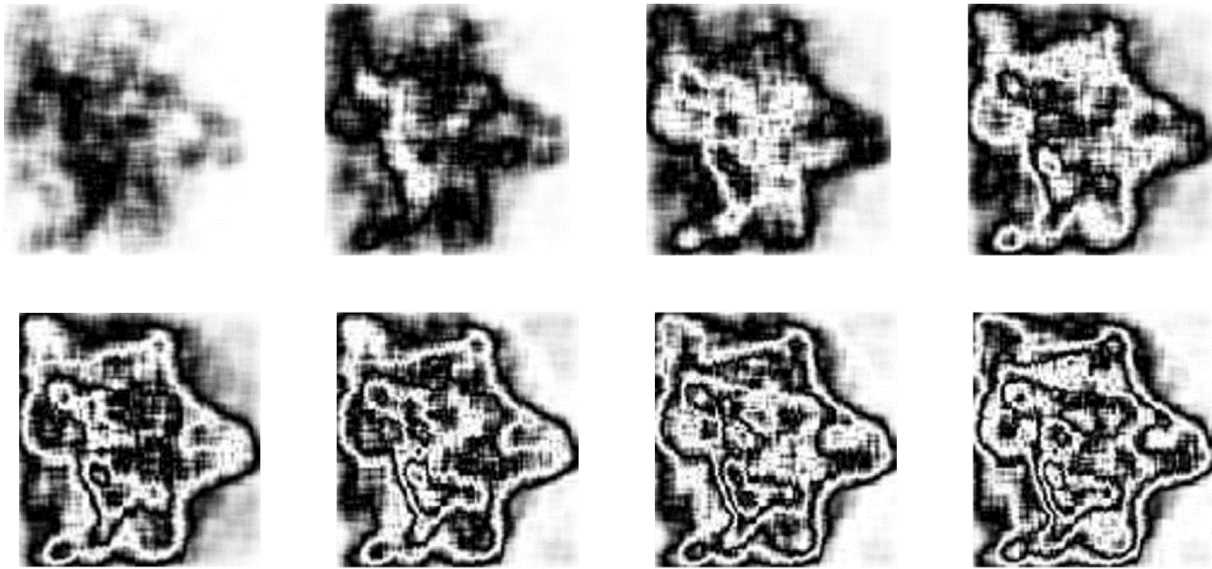
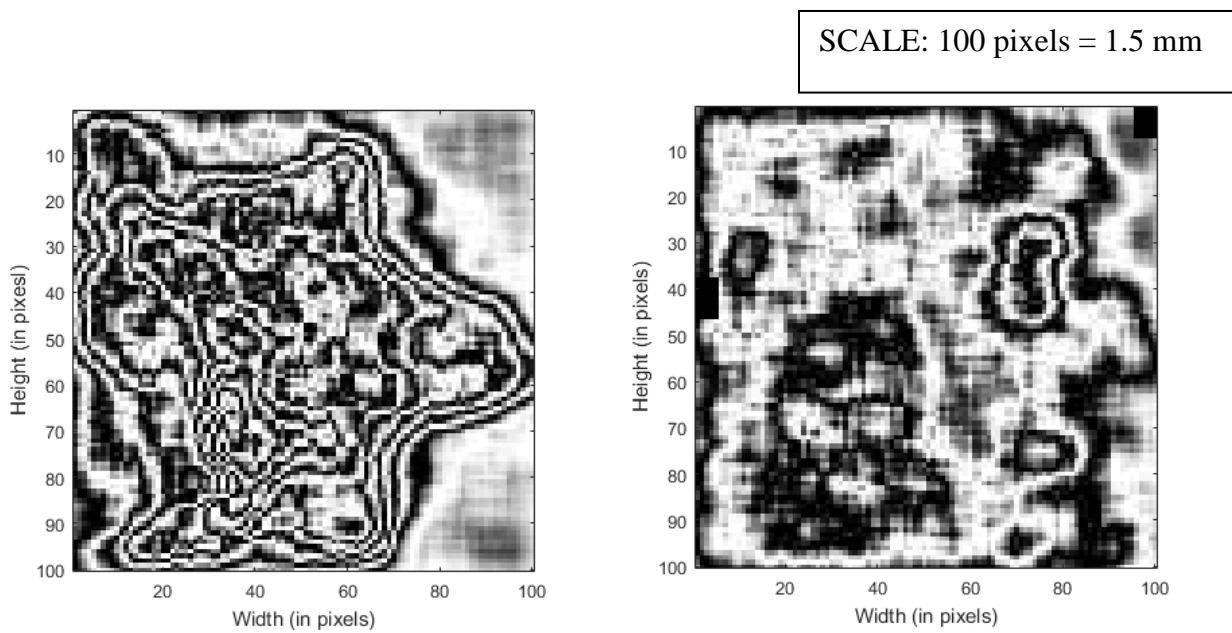


Figure 4-32: Phase evolution of the seed with time. The data is yet to be studied further for interpretation



**Figure 4-33: (Left) Wrapped phase map of a healthy seed
(Right) Wrapped phase map of copper treated inhibited seed sample**

5. Conclusions and Future Work

5.1. Dynamic Measurement Technique and Its Features

The primary focus of this research was to do non-contact full-field measurements of moving objects using ESPI. Conventional phase-stepping ESPI needs the test object to be quasi-static; it requires for every measurement that at least three phase stepped images are available. The proposed Interpolated-ESPI technique overcomes the quasi-static limitation. It uses a camera-synchronized PZT mirror. A striking difference is that in the conventional systems, the PZT triggers the camera while in this technique, the camera triggers the PZT mirror. After each frame is captured, the exposure signal steps the PZT mirror for the next frame. Even though only one frame is captured at a time, it allows for mathematically generating the required phase stepped images at every time instant. Therefore, it becomes possible to have available all the required phase sequences. Here, as in conventional practice, four stepped images are used instead of three to achieve more stable results. Once the four phase-stepped intensities at every time instant are known, it is possible to get continuous instantaneous phase values.

In conventional phase-stepping ESPI, the phase values obtained are wrapped, meaning there is a cyclic phase jump between $-\pi$ and π . Therefore, to get the overall displacement map, the wrapped phases need to be unwrapped using specialized algorithms. This is problematic when there are discontinuities in the sample or where large noise is present. Sophisticated but computationally expensive algorithms are often but not always effective in handling these challenges. In the proposed Interpolated-ESPI technique, accumulation of the incremental phases from one time instant to the next directly gives the phase values corresponding to the final displacements. No unwrapping is required because the phase change from one image to the next is small, well within the $-\pi$ to π range. In addition, every pixel acts as an independent displacement

sensor, unaffected by neighbouring pixels. This makes it possible to measure discontinuous samples with ease.

Given the simultaneous availability of four phase stepped images, the local average intensity, A and modulation, B are known for all the pixels at every moment. This allows for detection of low modulation points, saturated points and most importantly, points of speckle decorrelation when the modulation approaches zero. Low modulation and decorrelation are related in a way that the bulk speckle motion from one pixel to the next causes the modulation to drop precipitously. Pixels identified with saturation or low modulation, can then be corrected. This idea adds on to one of the main features of the proposed technique. By overcoming the decorrelation problem, it has the ability to measure large deformations in the scale of millimeters, limited only by the field of view and focal depth of the camera.

The important features of the Interpolated-ESPI technique can be summarized as follows.

It

- can detect both the amplitude and the direction of motion of a **moving** sample,
- is able to measure **large deformations** with accuracy and precision,
- can measure **discontinuous deformations** in a sample.

5.2. Applications

The Interpolated-ESPI technique expands the scope of conventional ESPI to applications where the test sample is not quasi-static. It can be used to measure vibrations, as successfully demonstrated. The amplitudes can be found out from the unwrapped data. Once the displacement map of the surface is obtained, basic Fourier Transforms can be applied to obtain the frequency of

vibration. This ESPI technique has applications in non-destructive testing (NDT) and strain analysis. Full-field surface deformation maps of samples under loading or stress can be obtained, regions of stress concentration can be detected in manufactured parts in automobile and aerospace industries, especially with the ability to overcome the problem of decorrelation. In composite materials, it can be used for crack detection and finding areas of poor bonding. Material characterization is another area of application. Other interesting industries where this can be used are biology and cereal industries [42].

5.3. Challenges

- A major challenge is the requirement for high camera frame rate. Due to the nature of the algorithm, i.e., the fact that four phase-stepped images must be acquired quasi-simultaneously, the frame rate requirement becomes four times that of other dynamic methods. This can be solved using high-speed cameras.
- Good modulation is essential so that there is a clear distinction between points/cycle/sequence and a good signal to noise ratio is maintained.
- For high-speed imaging, exposure times are much smaller than used with quasi-static ESPI systems. To combat the effects of the shorter light collection times, either greater light intensities and/or increased bit-depth, low-noise camera need be used.
- Calibration error: The calibration process makes use of the speckles to determine the voltages necessary for the PZT mirror; External vibrations, noise and speed of motion of the mirror result in variation in step angles such that they are in the range of $90^\circ \pm 10^\circ$.
- A system limitation is that the current set-up is only capable of measuring deformations in one direction and it is an in-plane interferometry set-up.

5.4. Future Work

It would be desirable to expand the measurement capabilities to enable multi-dimensional measurements. That would enable measurements of full 3-D deformation maps of moving surfaces. Such a system would be capable of measuring even complex vibrational modes where points move in different dimensions.

One idea of such a system involves a few modifications. The green laser can be replaced by an RGB laser and the monochrome camera can be replaced by a colour camera. Figure 5-1 illustrates the concept. The combined beam from RGB laser would pass through an assembly of dichroic filters, each chosen to transmit or reflect red, green and blue light. The set-up would be such that each coloured beam when combined with the common beam on the surface of the sample, would result in three sensitivity directions. The various directional measurements could then be decomposed into 3-D axial components.

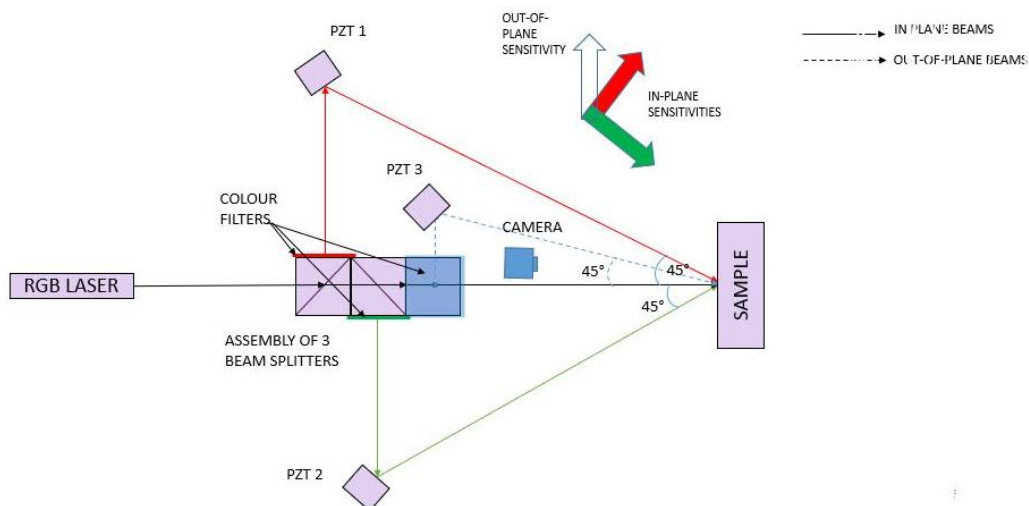


Figure 5-1: Proposed 3D dynamic ESPI setup for future work

The three PZT mirrors would be connected to the camera in a way similar to the current in-plane dynamic ESPI setup where all of them would be synchronized to the strobe signal of the camera. The three colour channels in the camera would pick up the phase change corresponding to the three sensitivity directions and they can be combined to give full 3-D displacement data. When only one piezo mirror is present, the phase steps for the three colours would be different. With the assumption that the phase stepping for all the three colours remain constant within themselves, it is then possible to use Carre's calibration technique [31]. This way the setup can be made compact.

Another objective is to achieve consistent biological interpretation of the phenomenon in case of biospeckles. There could be a diffraction related optical phenomenon yet to be explored and understood for the seed sample. To perform more controlled tests on seed samples remains a part of the future work. The results need to be studied further to interpret the meaning of the phase maps obtained in the test conducted. This can be an extremely valuable, innovative and state-of-the-art application of ESPI. Some of the tests that will be done include:

- Tests on dissected seed samples
- Tests on seed sample painted with a reflective coating
- Tests to compare healthy seeds and seeds infected with germ or bacteria
- Monitor fungal growth under a glass slab
- Effect of temperature on the germination process to be studied using ESPI
- Tests using an out-of-plane arrangement on the samples

References

- [1] T. Siebert, W. El-Ratal, R. Wegner, and A. Ettemeyer, "Combine simulation and experiment in automotive testing with ESPI measurement," *Exp. Tech.*, vol. 26, no. 3, pp. 42–47, 2002.
- [2] P. Aswendt, C. D. Schmidt, D. Zielke, and S. Schubert, "ESPI solution for non-contacting MEMS-on-wafer testing," *Opt. Lasers Eng.*, vol. 40, no. 5–6, pp. 501–515, 2003.
- [3] F. M. Vincitorio *et al.*, "Dynamic speckle study of microbial growth," *Proc. SPIE*, vol. 9660, no. August 2015, p. 96601Q–1–96601Q–6, 2015.
- [4] R. Shahar, P. Zaslansky, M. Barak, A. A. Friesem, J. D. Currey, and S. Weiner, "Anisotropic Poisson's ratio and compression modulus of cortical bone determined by speckle interferometry," *J. Biomech.*, vol. 40, no. 2, pp. 252–264, 2007.
- [5] P. J. Georgas and G. S. Schajer, "Simultaneous Measurement of Plate Natural Frequencies and Vibration Mode Shapes Using ESPI," *Exp. Mech.*, vol. 53, no. 8, pp. 1461–1466, 2013.
- [6] K. Creath, "Phase-shifting speckle interferometry," *Appl. Opt.*, vol. 24, no. 18, pp. 3053–3058, 1985.
- [7] B. P. Holownia, "Non-destructive testing of overlap shear joints using electronic speckle pattern interferometry," *Opt. Lasers Eng.*, vol. 6, no. 2, pp. 79–90, 1985.
- [8] J. N. Butters, "Application of ESPI to NDT," *Opt. Laser Technol.*, vol. 9, no. 3, pp. 117–123, 1977.
- [9] O. J. Løkberg and J. T. Malmo, "Detection of defects in composite materials by TV holography," *NDT Int.*, vol. 21, no. 4, pp. 223–228, 1988.
- [10] R. Jones and C. Wykes, *Holographic and Speckle Interferometry*, Second. Cambridge U. Press, Cambridge, 1989.
- [11] C. Ramault, A. Makris, D. Van Hemelrijck, E. Lamkanfi, and W. Van Paepegem,

- “Comparison of different techniques for strain monitoring of a biaxially loaded cruciform specimen,” *Strain*, vol. 47, no. SUPPL. 2, pp. 210–217, 2011.
- [12] M. Hagara, F. Šimčák, and M. Kalina, “The knowledge acquired by using of optical methods by strain fields investigation,” vol. 486, pp. 141–146, 2014.
- [13] C. Joenathan, P. Haible, and H. J. Tiziani, “Speckle interferometry with temporal phase evaluation: influence of decorrelation, speckle size, and nonlinearity of the camera,” *Appl. Opt.*, vol. 38, no. 7, pp. 1169–1178, 1999.
- [14] J. A. Leendertz, “Interferometric displacement measurement on scattering surfaces utilizing speckle effect,” *J. Phys. E.*, vol. 3, no. 3, pp. 214–218, 1970.
- [15] E. Archbold, J. M. Burch, and A. E. Ennos, “Recording of In-Plane Surface Displacement by Double Exposure Speckle Photography,” *J. Mod. Opt. - JMOD Opt.*, vol. 17, pp. 883–898, 1970.
- [16] J. W. Goodman, “Statistical Properties of Laser Speckle Patterns,” in *Laser Speckle and Related Phenomena*, 2nd ed., Dainty J.C., Ed. Springer-Verlag Berlin Heidelberg, 1975.
- [17] P. Hariharan, *Basics of Interferometry*, Second. Academic Press, 2006.
- [18] G. Gülker, O. Haack, K. Hinsch, H. C. K. J, and P. W., “Two-wavelength electronic speckle-pattern interferometry for the analysis of discontinuous deformation fields,” *Appl. Opt.*, vol. 31, no. 22, pp. 4519–4521, 1992.
- [19] J. Kato, I. Yamaguchi, and Q. Ping, “Automatic deformation analysis by a TV speckle interferometer using a laser diode.,” *Appl. Opt.*, vol. 32, no. 1, pp. 77–83, 1993.
- [20] a J. Haasteren and H. J. Frankena, “Real-time displacement measurement using a multicamera phase-stepping speckle interferometer.,” *Appl. Opt.*, vol. 33, no. 19, pp. 4137–42, 1994.
- [21] M. Takeda, H. Ina, and S. Kobayashi, “Fourier-transform method of fringe-pattern analysis for computer-based topography and interferometry,” *J. Opt. Soc. Am.*, vol. 72, no. 1, p. 156, 1982.

- [22] X. Li, "Deformation analysis with temporal speckle pattern interferometry," *Opt. Eng.*, vol. 40, no. 2, p. 310, 2001.
- [23] D. J. Anderson, J. D. Valera, and J. D. C. Jones, "Electronic speckle pattern interferometry using diode laser stroboscopic illumination," *Eng. Opt.*, vol. 4, no. 4, pp. 982–987, 1993.
- [24] T. J. Cookson, J. N. Butters, and H. C. Pollard, "Pulsed lasers in electronic speckle pattern interferometry," *Opt. Laser Technol.*, vol. 10, no. 3, pp. 119–124, 1978.
- [25] A. J. Moore, D. P. Hand, J. S. Barton, and J. D. Jones, "Transient deformation measurement with electronic speckle pattern interferometry and a high-speed camera.," *Appl. Opt.*, vol. 38, no. 7, pp. 1159–1162, 1999.
- [26] D. R. Schmitt and R. W. Hunt, "Optimization of fringe pattern calculation with direct correlations in speckle interferometry.," *Appl Opt.*, vol. 36, no. 34, pp. 8848–8857, 1997.
- [27] P. J. Georgas and G. S. Schajer, "Modulo-2pi phase determination from individual ESPI images," *Opt. Lasers Eng.*, vol. 50, no. 8, pp. 1030–1035, 2012.
- [28] W. An and T. E. Carlsson, "Speckle interferometry for measurement of continuous deformations," *Opt. Lasers Eng.*, vol. 40, no. 5–6, pp. 529–541, 2003.
- [29] C. Pérez López, F. Mendoza Santoyo, R. Gutiérrez Zamarripa, and C. Caloca Mendez, "Measurements of mechanical deformation using a full field optical interferometry and a fast camera," *Proc. SPIE - Int. Soc. Opt. Eng.*, vol. 6046, no. February 2006, p. 60461W–60461W–5, 2006.
- [30] Y. Fu, G. Pedrini, and X. Li, "Interferometric Dynamic Measurement: Techniques Based on High-Speed Imaging or a Single Photodetector," *Sci. World J.*, vol. 2014, pp. 1–14, 2014.
- [31] D. W. Robinson, G. T. Reid, and P. de Groot, "Interferogram Analysis–Digital Fringe Pattern Measurement Technique," *Phys. Today - PHYS TODAY*, vol. 47, 1994.
- [32] A. Baldi, F. Bertolino, and F. Ginesu, "Phase Unwrapping Algorithms: A Comparison," in *Interferometry in Speckle Light*, 2000, pp. 483–490.

- [33] S. Jia, "New method for correcting the error of phase unwrapping.," *Proc. SPIE*, vol. 3783, no. July, pp. 325–329, 1999.
- [34] H. Xia *et al.*, "Phase calibration unwrapping algorithm for phase data corrupted by strong decorrelation speckle noise," *Opt. Express*, vol. 24, no. 25, pp. 28713–28730, 2016.
- [35] Y. Deng and D. Chu, "Coherence properties of different light sources and their effect on the image sharpness and speckle of holographic displays," *Sci. Rep.*, vol. 7, no. 1, pp. 1–12, 2017.
- [36] L. W. Bingleman and G. S. Schajer, "DIC-Based Surface Motion Correction for ESPI Measurements," *Exp. Mech.*, vol. 51, no. 7, pp. 1207–1216, 2011.
- [37] G. Cloud and Cambridge University Press., *Optical Methods of Engineering Analysis*. Cambridge University Press, 1995.
- [38] A. Zdunek and J. Cybulska, "Relation of biospeckle activity with quality attributes of apples," *Sensors*, vol. 11, no. 6, pp. 6317–6337, 2011.
- [39] J. D. Briers and A. F. Fercher, "Retinal blood-flow visualization by means of laser speckle photography.," *Invest. Ophthalmol. Vis. Sci.*, vol. 22, no. 2, p. 255, 1982.
- [40] J. A. Pomarico *et al.*, "Speckle interferometry applied to pharmacodynamic studies: Evaluation of parasite motility," *Eur. Biophys. J.*, vol. 33, no. 8, pp. 694–699, 2004.
- [41] A. Adamiak, A. Zdunek, A. Kurenda, and K. Rutkowski, "Application of the biospeckle method for monitoring bull's eye rot development and quality changes of apples subjected to various storage methods-preliminary studies," *Sensors*, vol. 12, no. 3, pp. 3215–3227, 2012.
- [42] D. B. Sutton and Z. K. Punja, "Investigating biospeckle laser analysis as a diagnostic method to assess sprouting damage in wheat seeds," *Comput. Electron. Agric.*, vol. 141, pp. 238–247, 2017.